



**HAL**  
open science

# Magnetic field sensor arrays for current determination using spatial harmonics : application to measurements in electrical grids

Benjamin Wilsch

► **To cite this version:**

Benjamin Wilsch. Magnetic field sensor arrays for current determination using spatial harmonics : application to measurements in electrical grids. Electric power. Université Grenoble Alpes, 2016. English. NNT : 2016GREAT028 . tel-01599037

**HAL Id: tel-01599037**

**<https://theses.hal.science/tel-01599037>**

Submitted on 1 Oct 2017

**HAL** is a multi-disciplinary open access archive for the deposit and dissemination of scientific research documents, whether they are published or not. The documents may come from teaching and research institutions in France or abroad, or from public or private research centers.

L'archive ouverte pluridisciplinaire **HAL**, est destinée au dépôt et à la diffusion de documents scientifiques de niveau recherche, publiés ou non, émanant des établissements d'enseignement et de recherche français ou étrangers, des laboratoires publics ou privés.

## THÈSE

Pour obtenir le grade de

### **DOCTEUR DE LA COMMUNAUTÉ UNIVERSITÉ GRENOBLE ALPES**

Spécialité : **Génie Électrique**

Arrêté ministériel : 7 août 2006

Présentée par

**Benjamin WILSCH**

Thèse dirigée par **Orphée CUGAT**  
coencadrée par **Laure-Line ROUVE**  
et codirigée par **Nouredine HADJ-SAID**

préparée au sein du **Laboratoire de Génie Électrique de Grenoble (G2Elab)**  
dans l'**École Doctorale «Électronique, Électrotechnique, Automatique et Traitement du Signal»**

## **Dispositif de magnétomètres pour la mesure de courant exploitant les harmoniques d'espace**

**Application aux réseaux électriques**

Thèse soutenue publiquement le **31 Mars 2016**,  
devant le jury composé de :

**Pr Charles JOUBERT**

Professeur Université Lyon, Président

**Dr Christophe COILLOT**

Ingénieur de recherche, Université Montpellier, Rapporteur

**Dr Luca DI RIENZO**

Associate Professor, Politecnico di Milano, Examineur

**Dr Orphée CUGAT**

Directeur de recherche, CNRS, Directeur de thèse

**Dr Laure-Line ROUVE**

Ingénieur de recherche, Grenoble INP, Coencadrante de thèse

**Pr Nouredine HADJ-SAID**

Professeur, Grenoble INP, Co-Directeur de thèse

**Dr François COCHET**

Ingénieur de recherche, Nexans Suisse, Invité





---

**Magnetic Field Sensor Arrays for  
Current Determination Using Spatial Harmonics**  
Application to Measurements in Electrical Grids

---

PhD thesis

submitted to the University of Grenoble

Benjamin Wilsch

May 31, 2016



## Abstract

The evolution of electrical grids from conventional unidirectional power transmission to diverse networks with a large variety of electricity consumers and producers requires the development of advanced and/or novel measurement and communication technologies, in order to create smart grids. As a part of the SOGRID project, an innovative current measurement method was developed to supplement the existing range of current sensors and to facilitate the installation, since the sensor is not only non-intrusive but can also be located at a distance from the cable.

The primary obstacle for precise current measurement in power grids is the three-phase nature of power transmission. A current sensor that is to be employed in the electrical grid must therefore provide geometrical selectivity between the individual phases. Existing commercial current sensors are non-intrusive but require placement around the conductor of interest, e.g. to measure the field along a closed path. Solutions include Rogowski coils, magnetoresistors, Hall effect or fluxgate sensors as well as magneto-optical sensors. However, a placement around the conductor limits the miniaturization required by smart grid development: miniature sensors can be integrated with other measurement and data transmission units, thus enabling the densely meshed monitoring and control of modern smart grids. In order to avoid these restrictions and to improve geometrical selectivity, a current measurement method based on the decomposition of the field into spatial harmonics has been developed in this thesis.

The decomposition of the magnetic field into spatial harmonics is based on the development of the magnetic field within a defined area/volume in a series of products of periodic functions, a radial dependence and corresponding development coefficients, so that the sum of the (in theory infinite number of) development orders reconstructs the field accurately. The development is performed for a source-free region besides the source of the field (internal field decomposition), which uses functions that increase from the center of decomposition toward the field source. The current measurement process is based on the determination of the development coefficients for the various orders, wherein higher orders exhibit a reduced dependence on perturbing sources (as long as the field measurements are performed closer to the conductor of interest than to the perturbing conductor). The relation between these coefficients and the current of interest is linear and defined by transfer factors.

In order to exploit the increased geometrical selectivity of higher orders, it is necessary to perform a sufficient number of magnetic field measurements on the boundary of a suitable area/volume in order to derive the development coefficients from the solution of an inverse problem. The size and positioning of this sensor array also plays a vital role in the detectability of higher order contributions to the field. Suitable 2D (for straight conductors) and 3D (for arbitrary conductor paths) prototypes were designed, implemented and subsequently tested in the laboratory during this thesis.

Further developments focus on determining the characteristic transfer factors. While these can be easily determined if a known controlled current is induced in the conductor, a method that allows for their determination under real operating conditions must be developed for industrial applications. A suitable calibration method is presented in this thesis.



## Résumé

L'évolution des réseaux électriques d'une transmission de puissance unidirectionnelle classique vers un réseau diversifié avec une grande variété de consommateurs et producteurs d'électricité, requiert le développement des technologies de mesure et de communication avancées et/ou nouvelles. Dans le cadre du projet SOGRID, une méthode innovante de mesure de courant a été développée pour enrichir la gamme existante des capteurs de courant et pour faciliter l'installation dans le réseau électrique. En effet, le capteur développé ici est non seulement non-intrusif, mais peut également être déporté du câble.

Dans les réseaux électriques, l'obstacle principal pour une mesure précise du courant est la nature triphasée de transmission de puissance. Un capteur de courant qui doit être utilisé dans le réseau électrique doit donc fournir une sélectivité géométrique entre les différentes phases. Les solutions commerciales existantes sont non-intrusives, mais nécessitent le placement entourant le conducteur d'intérêt pour mesurer le champ le long d'un chemin fermé. Ces solutions comprennent des bobines de Rogowski et les mesures en boucle fermée avec des capteurs de champs comme les magnétorésistances, les capteurs à effet Hall ou les fluxgates, ainsi que des solutions magnéto-optiques. Toutefois, un placement autour du conducteur limite la miniaturisation requise par le développement des réseaux intelligents: des capteurs miniatures peuvent être intégrés avec d'autres unités de mesure et de transmission de données pour permettre le suivi et le contrôle des réseaux intelligents modernes avec une maille plus dense.

Afin de répondre à ces exigences, et pour améliorer la sélectivité géométrique des conducteurs, une méthode de mesure de courant basée sur la décomposition du champ en harmoniques spatiales a été développée dans cette thèse.

La décomposition du champ magnétique en harmoniques spatiales est basée sur le développement du champ magnétique à l'intérieur d'une zone / volume défini avec une série de fonctions périodiques, une dépendance radiale et des coefficients de développement correspondants, de sorte que la somme des ordres (théoriquement infini) de développement reconstruit le champ avec précision. Le procédé de mesure de courant est basé sur la détermination des coefficients de développement pour les différents ordres, dans lequel les ordres supérieurs présentent une dépendance réduite aux sources de perturbation (à condition que les mesures de champ sont réalisées plus proches du conducteur de l'intérêt que du conducteur perturbateur). La relation entre ces coefficients et le courant d'intérêt est linéaire et défini par des facteurs de transfert.

Afin d'exploiter la sélectivité géométrique accrue des ordres supérieurs, il est nécessaire d'effectuer un nombre suffisant de mesures du champ magnétique sur la limite d'une zone / volume approprié afin de déduire les coefficients de développement à partir de la solution d'un problème inverse. La taille et le positionnement de ce réseau de capteurs jouent des rôles essentiels dans la détectabilité des contributions d'ordre supérieur du champ. Des prototypes appropriés pour une décomposition en 2D (pour les conducteurs rectilignes) et en 3D (pour les conducteurs avec des chemins arbitraires) ont été conçus, mis en œuvre et ensuite testés en laboratoire au cours de cette thèse.

D'autres développements se concentrent sur la détermination des facteurs de transfert caractéristiques dans des conditions d'opération réelles pour des applications industrielles. Une méthode de calibration appropriée est aussi présentée dans cette thèse.

---

---

# Acknowledgements

This work would not have been possible without the contributions of many people, who I do not only want to thank for their effort but also for making the past three years such a valuable and enjoyable experience.

First of all, I would like to thank my supervisors for the opportunity to conduct this thesis work as a member of their research groups. From the beginning I was able to work in an optimal working environment with the necessary facilities and personnel to successfully complete the successive steps and, wherever necessary, they helped find competent contacts for further inquiries.

I thank Prof. Jérôme Delamare for his contribution during the initial phase of the work, the examination of different research paths for the given task and the indication of spatial harmonics as a potential solution. I thank Dr. Orphée Cugat for his support and input throughout the thesis work, especially in the design of the prototypes, and the coordination of the work within the SO-GRID project. I thank Dr. Laure-Line Rouve for readily taking over as thesis supervisor on short notice, for the valuable insights on spatial harmonics and magnetometer technologies and the interesting and helpful discussions during the development of the measurement methods, especially the calibration method, and during the writing of the thesis.

I thank Dr. Olivier Pinaud for his work and input both for the simulations and, especially, the implementation of the experimental setup (twice, on campus and at GreEN-ER). The fruitful discussions allowed for significant developments during the work. I thank Dr. Menad Bourkeb for his contribution during the last half year of my thesis work, especially, for this seamless integration into the group and work which allowed us to proceed without missing a stride during a very intense experimental phase. I am also thankful for the productive and enjoyable atmosphere created by all the PhD students/post-docs at Minatec (Thomas Lafont, Elena and Boris Gusarov) and the ERT (Vincent Fedida, Lyes Ifrek and Vinicius Oiring).

I thank Florian Dumas for his advice on the design phase of both the 2D and 3D prototypes as well as the fabrication of the 2D prototypes and the support structures for placement within the experimental setup.

For the support throughout my studies, I thank my parents.

Last but foremost I thank Elena and Leticia.



# Contents

<b>I</b>	<b>Introduction &amp; Scope</b>	<b>1</b>
I.1	Smart grids . . . . .	1
I.2	The SOGRID project . . . . .	4
I.3	Measurement conditions and requirements . . . . .	7
<b>II</b>	<b>Sensor technology: state-of-the-art</b>	<b>11</b>
II.1	Dedicated current sensor technology . . . . .	16
II.2	Magnetic field sensor technology . . . . .	19
II.2.1	Hall effect sensors . . . . .	19
II.2.2	Magnetoresistors . . . . .	20
II.2.3	Fluxgate technology . . . . .	22
II.2.4	Sensing configurations for geometrical selectivity . . . . .	25
II.3	Patented measurement principles . . . . .	30
II.4	Outlook . . . . .	34
II.4.1	MEMS technology . . . . .	34
II.4.2	Induction sensors . . . . .	36
II.5	Conclusion . . . . .	39
<b>III</b>	<b>Spatial harmonics decomposition</b>	<b>41</b>
III.1	Introduction to spatial harmonics . . . . .	41
III.2	2D magnetic field decomposition in spatial harmonics . . . . .	43
III.2.1	Coefficient identification/inverse problem . . . . .	54
III.2.2	Parametric analysis: dimensioning and error sources . . . . .	55
III.3	Calibration procedure (2D case) . . . . .	68
III.3.1	Calibration of transfer factor - general considerations . . . . .	68
III.4	3D spherical harmonics decomposition . . . . .	72

III.4.1	Linear and non-linear conductors . . . . .	76
III.4.2	Sensor distribution . . . . .	78
III.4.3	Parametric analysis - dimensioning and error sources . . . . .	82
III.5	AC measurement methods . . . . .	91
III.5.1	Pointwise evaluation . . . . .	91
III.5.2	Fast Fourier Transform of field measurements . . . . .	92
III.6	Conclusion . . . . .	92
<b>IV</b>	<b>Prototypes and laboratory setup</b>	<b>95</b>
IV.1	Sensor technology for laboratory tests: Stefan Mayer fluxgate sensors . . . . .	96
IV.2	2D prototypes . . . . .	98
IV.3	3D prototype . . . . .	99
IV.4	Laboratory setup . . . . .	101
IV.5	Magnetic sensor characterization and offsets . . . . .	102
<b>V</b>	<b>Experimental results</b>	<b>107</b>
V.1	2D measurement arrays . . . . .	108
V.1.1	Transfer factors . . . . .	108
V.1.2	Effect of perturbing conductor . . . . .	111
V.1.3	Reproducibility (second sensor array) . . . . .	115
V.1.4	Calibration method . . . . .	121
V.1.5	AC measurements . . . . .	124
V.2	3D measurement array . . . . .	131
V.3	Conclusion and Perspectives . . . . .	133
<b>VI</b>	<b>Conclusion and Outlook</b>	<b>137</b>
VI.1	Conclusion . . . . .	137
VI.2	Perspectives . . . . .	141
VI.3	Long-term technological advances . . . . .	143
	<b>Bibliography</b>	<b>149</b>
	<b>List of Figures</b>	<b>152</b>
	<b>List of Tables</b>	<b>153</b>

---

# Introduction & Scope

---

The objective of the work detailed below, is the development of an innovative current sensor that meets the demands of smart grids. Consequently, this introduction serves to explain the characteristics of modern, intelligent electrical grids and the requirements they pose for a current sensor, in order to fulfil their intrinsic demand for a close-meshed, “real-time” monitoring. The French smart grid development project, SOGRID, as part of which this work is conducted, will also be introduced and the project guidelines with respect to the current sensor will be discussed.

## I.1 Smart grids

The electrical grid was originally conceived and developed to provide consumers with the electricity that has become the pivotal resource of the modern society. Therefore, the focus of the first one hundred years of grid development, after the installation of the first power grid in 1886, was placed on establishing a gapless connection of all consumers to a reliable electricity supply (with the well-known differences in the development status for different countries). For this purpose, centralized production plants were used to generate electricity which was subsequently transported to the consumers (households and industry) via transmission and distribution networks as well as substations. The flow of power was thus essentially unidirectional, as illustrated by the left hand-side of Fig.I.1. While the types and variations of power plants were continuously adapted to meet the increasing demand for electricity (e.g. the development of nuclear power plants), the fundamental structure of the grid remained unchanged and it was rather the size of the grid that was subject to a rapid growth. The last thirty years have then seen a remarkable evolution of

## I.1. Smart grids

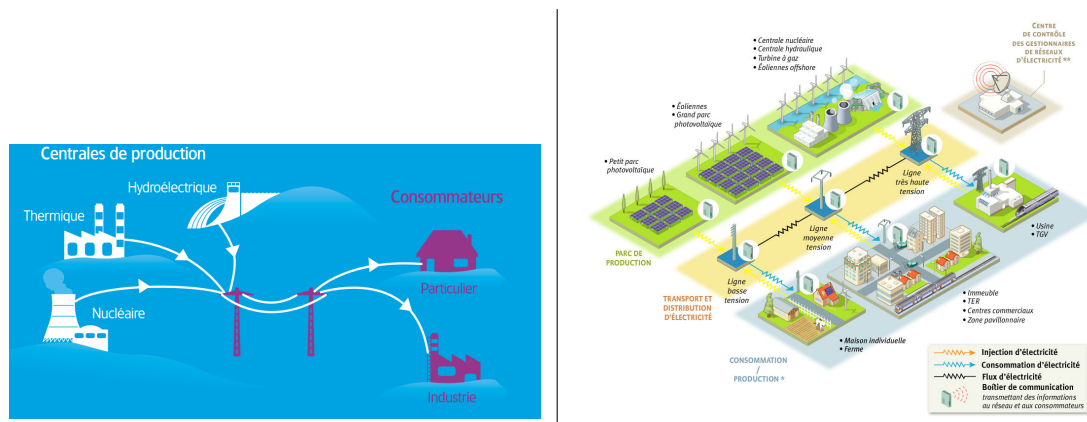


**Figure I.1:** Evolution of the electrical grid topology. From a unidirectional power flow between production plants and consumers (left) to a complex smart grid with a significantly improved communication layer and various additional network components (right).<sup>[1]</sup>

the topology of the electrical grid. A primary cause for this can be found in a combination of technological innovation and an interest in the use of the latter for energy efficient and sustainable solutions, which has been strengthened significantly by the concerns about greenhouse gas emissions. The most prominent example in this respect is the development of technologies to use renewable energy sources (sunlight, wind, water, etc.) for the production of electricity. The pressing need for this paradigm shift is underlined by the ambitious goals of the 10-year strategy of the European Commission for “smart, sustainable, inclusive growth” (Europe 2020), which, among others, includes the objectives of reducing greenhouse gas emissions by (at least) 20% compared to 1990, to increase energy efficiency by 20% and to increase the share of renewable energy in final energy consumption to 20%. The widespread use of renewable energy sources has led to the fact that the few, large and centralized (predominantly fossil fuel or nuclear) power plants of the past are nowadays supplemented or replaced by large numbers of small, decentralised power plants that feed electricity into the grid on both the transmission and distribution level of the electrical grid. Unlike the man-made fossil fuel power plants, the distribution of equipment to harvest renewable energy sources is adapted to suit the specific sources (e.g. off-shore wind parks) and an optimal usage of these resources is by nature strongly delocalized, while also incorporating power generation on both the household level (e.g. photovoltaic [PV] panels) as well as large-area wind or PV parks. In addition, renewable energy resources are subject to strong seasonal, geographical and meteorological variations which introduce peaks in the load level. The structure of the electri-

cal grid is thus significantly complexified by the integration of power generation using renewable energy sources at all levels of the electrical grid and this calls for advanced and closer monitoring and also requires greater load balancing efforts. Furthermore, the originally unidirectional character has been replaced by a fundamentally bidirectional nature, since former consumption endpoints can now also serve as power generation points that feed electricity into the grid. Energy storage facilities (e.g. batteries) and electric vehicles further contribute to the manifold demand-supply considerations that define the modern grid. An example for the pronounced change in the number and distribution of power generation plants is given in Fig.I.2, for Denmark which takes advantage of its geographical location by focusing on wind-powered electricity generation. Solutions to adapt the grid management to this new reality can be implemented as part of (overdue) grid modernization efforts that have become necessary in view of the peaking energy demand of modern societies, and which are, in some countries more than others, accentuated by outdated grid equipment, which results in an increasing number of blackouts.

The reconfiguration of the grid necessitates a more densely meshed, real-time monitoring and control of power generation, storage and consumption, as well as an information and communication layer to link the individual components and control centres of the grid. The development of new communication technologies, such as power line communication, fibre-optics and wireless networks are thus essential enabling components of the grid development. Along with digital processing capabilities, these new communication and control features allow for various “intelligent” and dynamic grid management solutions, which are the origin of the term ‘smart grids’. Besides the integration of renewable energy sources and energy efficiency measures, the concept of smart grids also encompasses customer-side demand-response management (smart meters) and the control of household appliances for the purpose of load management (smart appliances). Smart grids seek to provide grid reliability and sustainability, load balancing, flexibility in network topology, peak curtailment (e.g. via price incentives/smart meters) and the integration of smart cities and electrical vehicles, while also providing a platform for new and advanced services that were unthinkable for the classical grid structure.

Today, numerous projects and deployments to test individual or multiple features of smart grids have already been implemented or are currently being implemented to advance the development of smart grids in all industrialized countries. It is important to keep in mind that the transition from the classical, unidirectional grid architecture to modern smart grids is not immediate but rather a gradual process that started thirty years ago with the deployment of the first renewable energy power generation plants and initial automatic meter readings, and which is nowadays in full effect. As a reference, 459 smart grid projects have been launched in EU member states, Switzerland and

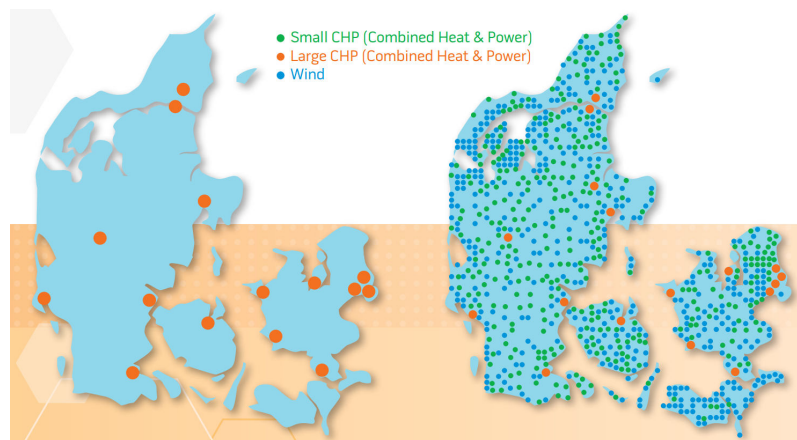


**Figure I.2:** Evolution of the number, distribution and type of power generation plants in Denmark, between the 1980s (left) and today (right)<sup>[3]</sup>

Norway between 2002 and 2014, for a total investment of 3.15 billion €. In France, this has already allowed for an enhanced observability of both the transmission grid, with 40,000 data points along 104,000 km (the largest electricity transmission system in Europe) of lines and 2,600 substations (63 to 400 kV), which are sampled every second, as well as the distribution grid, with 100,000 measurement and remote control devices and 30 regional dispatching centres for 1.3 million km of lines and 760,000 substations that serve 35 million customers.<sup>[2]</sup> In combination with advanced software and analysis algorithms, these devices and centres allow for fault-detection and the development of self-healing networks, and thus provide a considerable contribution to grid reliability. One of the projects that seeks to advance the monitoring capabilities of the distribution network, by further developing power-line communication and novel observation technology, the SOGRID project, provides the framework for the work conducted as part of this thesis and will thus be discussed in more detail in the following section.

## I.2 The SOGRID project

The SOGRID project was conceived and developed as of October 2011, after a tender from ADEME, (“Agence de l’Environnement et de la Maîtrise de l’Energie”, the French agency for the environment and energy management) and finally launched in April 2013. As its motto, “The electrical grid of the future”, indicates, it aims to further advance the development of smart grids. In particular, it is concerned with the implementation of a global and real-time communication

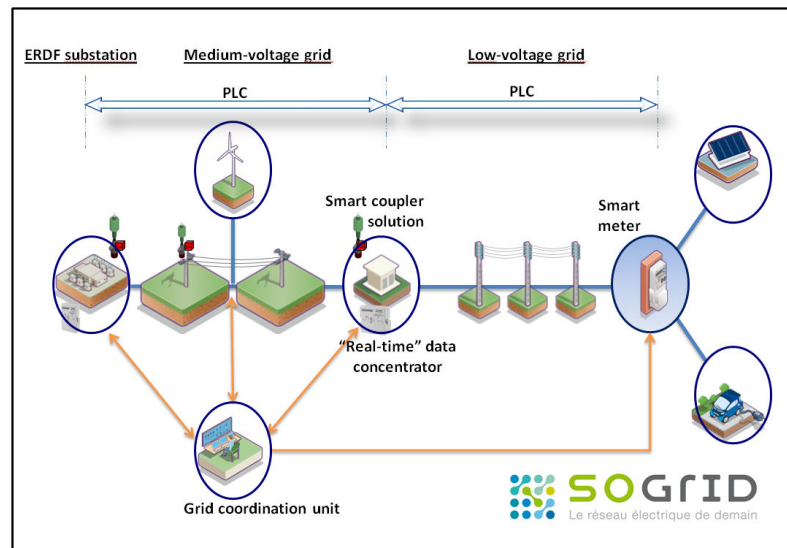


**Figure 1.3:** Overview of the components of the SOGRID project and their installation sites in the distribution grid.

and management system that connects all equipment of the distribution level of the electrical grid, i.e. the medium voltage grid. This allows the extension from smart devices to an entire smart grid. The project involves the use of a novel power-line communication (PLC) protocol to enable a transmission of digital information directly via the electrical grid. An electronic chip of a new generation, along with the integrated devices and software, provides the central piece of the project, which draws from overall funds of 27 million Euros, seeks to connect 1300 devices and involves 100 researchers divided between the 10 project partners. The consortium includes a utility (ERDF, owner of 95% of the French electrical distribution grid), technology companies (STMicroelectronics, Landis+Gyr, Sagemcom and Nexans), consulting firms (Trialog and Capgemini) and research institutes (Grenoble INP, Ecole Polytechnique ParisTech and LAN). Besides the third generation PLC communication system and protocols, the installation of innovative equipment for the grid observation and advanced grid management features of medium- and low-voltage (MV and LV) state estimation, fault localization and device control are the other two pillars of the project. The novel PLC communication system has been further developed within the SOGRID project (and several patents have been filed on this subject) and it is also being tested in a demonstrator project in the Toulouse metropolitan area, where a grid covering 1000 customers, 30 MV/LV substations, 5 MV and 2-3 source substations. This demonstrator project will be operational at the end of 2015. The central electronic chip of the SOGRID project which is provided by STMicroelec-

tronics, aims to combine the functions of voltage and current sensors (Nexans), a communication interface (Nexans), a data concentrator (Sagemcom) and a smart meter (Landis+Gyr). The responsible parties are indicated in brackets, however, the development of the individual components is performed by a qualified subset of the project consortium. Specifically, task 3.2. of the SOGRID project, “Innovative AC current sensors”, concentrates on the design of an AC current sensor to be used on the distribution level of the electrical grid. This current sensor is developed using the expertise of Grenoble INP, specifically G2Elab and as the focus of this thesis work, under the guidance of the industrial partner Nexans, a French manufacturer of cables for the infrastructure, industrial and construction market. As the second largest cable supplier worldwide and with a strong position in the electrical cable sector, Nexans is involved in various smart grid development projects and draws from a strong background in current and voltage measurements. During the early months of the collaboration with Nexans, it was quickly established that the primary interest for a current sensor is the development of an innovative current measurement method, which is unique with respect to existing measurement solutions detailed in Ch. 2 and which meets the precision requirements detailed below. The interest for a novel measurement principle stems from the desire to develop a current sensor that is well adapted to the specifics and requirements of modern (smart) grids. As explained above, the complexified structure of smart grids necessitates a closely-meshed monitoring of various relevant parameters, (primarily current, voltage and power) at defined intervals/frequencies in both space and time. While few sensors with a limited accuracy were sufficient to monitor and document the power flow in classical, unidirectional power grids, the high level of sophistication of smart grids require large numbers of sensors that are deployed at all critical points. To achieve this objective, it is thus desirable to develop current sensors that are (ideally) miniaturised, more precise and cheaper with respect to existing technologies. A miniaturisation of the sensor is of interest, in order to allow for an integration of the sensors with other measurement and data transmission units across the grid. These considerations triggered the development of a new measurement principle and sensor architecture which will be detailed in Ch. 3 and 4, while avoiding the limitations of existing current sensors (Ch. 2).

Before taking a closer look at existing sensor technologies that are suitable for application in (smart) electrical grids, it proves meaningful to further specify the measurement conditions of the applications envisioned within the SOGRID project.

### I.3 Measurement conditions and requirements

The fact that the SOGRID project is concerned with an advanced monitoring of the distribution level of the electrical grid, already dictates two fundamental principles of the current measurement conditions, namely:

- the distribution grid transmits power in the medium (AC) voltage range (in France: 'Haute Tension A, HTA', i.e.  $3 \text{ kV} \leq U \leq 50 \text{ kV}$ )<sup>1</sup>. Typical root-mean square (RMS) current values at this level of the electrical grid amount to 1000 A (but may increase by a factor of 10 in case of malfunctions). As will be detailed in the following chapter, a (contactless) current measurement necessitates magnetic field measurements for current determination. The field magnitude that results for the typical current ( $I = 1000 \text{ A}$ ) and a single conductor at a minimum distance of  $d = 25 \text{ mm}$  (the typical radius of cable insulations in this current range) is  $B = \frac{\mu_0 I}{2\pi d} = 8 \text{ mT}$ , with the vacuum permeability  $\mu_0$ . This can be used as a reference value for the discussion of magnetic field sensor technology in the following chapter.
- the three-phase nature of AC electrical power transmission implies that current measurements on one conductor/phase will occur in close proximity of the two other conductors/phases.

While the first point provides a parameter that must be observed in sensor design considerations, the second point provides the primary obstacle for a high precision determination of the current value. As will be detailed in the following chapter, current measurements on the grid imply (contactless) magnetic field measurements. The presence of adjacent conductors, will thus introduce an imprecision into the magnetic field (and thus current) measurement for the conductor under investigation. The central parameter for the assessment of the measurement precision of the current sensor will thus be the geometrical selectivity, i.e. the ability and extent to which it is possible, to differentiate the measurement of the conductor of interest from perturbing sources in the measurement environment. The study of the precision attainable with certain measurement principles and geometries thus constitutes the primary stage of the research for the thesis.

Besides accounting for the influence of adjacent conductors and other external magnetic field sources, the sensor is designed to be compatible with installation at various points of the electrical grid. In general, the different levels of the electrical power grid can be divided in terms of function (generation, transmission and distribution,) or voltage (low, medium and high voltage). The essential elements of power transmission between power sources and the industrial or domestic users are

---

<sup>1</sup>The exact limits and designation of the low-, middle- and high-voltage range are inconsistent for different countries

### I.3. Measurement conditions and requirements

---

substations, transformers and a combination of overhead and underground tri-phase cable systems. Coupling connectors are employed at the interfaces between the various components of the power grid. Two specific installation points that were prioritized based on discussions with Nexans are such coupling connectors and overhead power lines (on or near utility poles). The development of the measurement principle was, however, not limited to the consideration of a specific application case. It is merely possible to classify the measurement geometry within a range from simple, i.e. (theoretical) infinite straight conductor paths in-line on a horizontal axis, to complex, i.e. increasingly deformed conductor paths out of the horizontal axis, wherein the former case would be more closely related to overhead power lines, while the latter case applies to power couplers where the cables follow a (usually defined and for all three conductors identical) path. The measurement location and geometry can also entail limitations (of different strictness) for sensor characteristics, primarily the size (e.g. in order for the sensor to fit inside a power coupler). Within the given measurement conditions and geometries, the current sensors should achieve specific precision standards which were defined by Nexans based on their experience and requirements in the field of smart grind monitoring and control. Based on their time scales, the precision requirements can be divided into two complementary scopes with different requirements on the precision and, in consequence, different restrictions on the measurement procedure. These values are summarized in Table I.1. The desired frequency range starts at the fundamental transmission frequency of 50 Hz and reaches up to 25 kHz for transient effects.

	time scale	precision	method	objective
<b>periodical measurement</b>	s	0.2 – 0.5 %	measurement + data treatment	consumption metering
<b>continuous measurement</b>	$\mu$ s	lower	instantaneous measurement	detect transient faults

*Table I.1: Comparison of measurement requirements for the two application modes.*

To complete the set of criteria for the current sensor, it is important to recall the requirement of novelty with respect to the landscape of existing sensor products on the market as well as patent documents. The prerequisite of a geometrical selectivity between individual conductors, the defined precision requirements, the different measurement locations and geometries and the novelty criterion thus set the stage for the development of the current sensor which is the subject of this

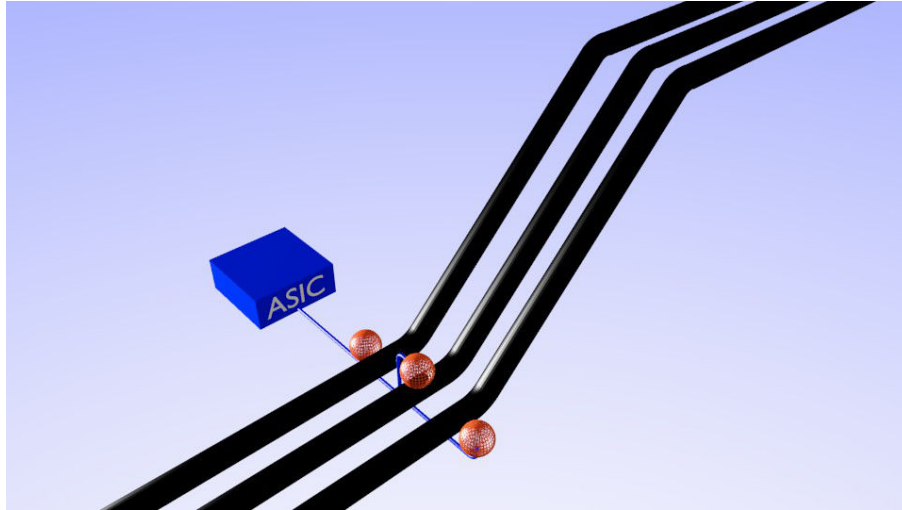


**Figure I.4:** Schematic of an exemplary measurement setup. The sensor arrays (red spheres) for each (non-linear) conductor are connected to an ASIC to allow data combination and processing for increased precision.

thesis work. An exemplary, but not representative, measurement scenario is displayed in Fig.I.4. As will become evident in the following chapters, each conductor (in black) will have a dedicated array of sensors (red spheres) which can be connected to a central data processing unit (e.g. an Application-Specific Integrated Circuit, ASIC) to combine the information received from each array.

The following chapters serve to delineate the development process from the prerequisites given above to the measurement solution indicated in Fig.I.4. Specifically, in a logically constitutive manner, Ch. 2 will provide an overview of the state-of-the-art of current and magnetic field sensor technology, while also justifying the selection of commercially available magnetic field sensors that meet the demands of the actual measurement process. The following Ch. 3 details the measurement principle that has been employed and developed to fulfil the task at hand. Ch. 4 subsequently discusses the implementation of different sensor prototypes which are used to obtain the measurement results provided in Ch.5.



---

## Sensor technology: state-of-the-art

---

---

II.1	Dedicated current sensor technology . . . . .	16
II.2	Magnetic field sensor technology . . . . .	19
II.2.1	Hall effect sensors . . . . .	19
II.2.2	Magnetoresistors . . . . .	20
II.2.3	Fluxgate technology . . . . .	22
II.2.4	Sensing configurations for geometrical selectivity . . . . .	25
II.3	Patented measurement principles . . . . .	30
II.4	Outlook . . . . .	34
II.4.1	MEMS technology . . . . .	34
II.4.2	Induction sensors . . . . .	36
II.5	Conclusion . . . . .	39

---

This chapter is intended to lay out the landscape for current sensor technology at the present date. For this purpose, the review of existing technologies will be comprehensive but the level of detail in individual points will be proportional to the relevance of the technology with respect to the task at hand. Consequently, some sensing technologies are listed with a brief description, while fluxgate sensors, which were used for the laboratory sensor prototype, are discussed in an

---

independent subsection. It is also important to keep in mind the requirements for the current sensor which were provided in Chapter I and which will be provided again, and supplemented by further considerations and parameters, at the pertinent points throughout this chapter. An additional refocusing mask is defined by the envisioned application area. Electrical current sensors are applied in a broad variety of fields, e.g. motor drives, power converters and modules, house automation, medical examination methods, etc., but this thesis is, in a broad sense, concerned with current determination in industrial applications (large DC or AC currents) and the explanations below will be oriented accordingly. Besides providing an overview of the diverse measurement principles that are employed for current determination, special attention is also attributed to the (commercial) availability and/or technological readiness of individual solutions, and a selection of commercially available products will be presented along with a number of relevant patent documents. The landscape of the state-of-the-art, which is outlined in the described manner, then allows for a positioning of the current measurement solution developed in this thesis work in terms of its innovative character, measurement functions as well as of the attainable precision.

The primary task of current sensors is the determination of the current magnitude at a required precision. Further decisive sensor parameters include the range, frequency response and the stability with respect to e.g. temperature variations. Electric current sensors can be classified in various categories. One meaningful distinction is possible between **contact** and **contactless** sensors. The former class provides high accuracy through a direct current measurements based on Ohm's law of resistance, using e.g. shunts or current-to-voltage converters. However, they require an interruption of the conductor and thus do not provide galvanic isolation and dissipate energy as heat, which makes them unsuitable for high-voltage/current environments and the task at hand. Given their self-evident nature with respect to current measurements, intrusive, contact measurement methods can also be considered the first generation of current measurement methods. As current measurement conditions and applications grew increasingly diverse over time, novel and equally diverse determination methods also became a necessity. The earliest and simplest form of achieving galvanic isolation between current-carrying conductors and the sensor is provided by current transformers which are based on Ampère's circuital law. They do however suffer significant errors due to saturation and hysteresis, high thermal losses and are very bulky (together with the equipment for periodic calibration). While popular in multiple applications current transformers are therefore not an option for an (ultimately miniature) current sensor solution intended for mass deployment throughout the electrical grid.

More advanced contactless current sensing methods rely on the determination of the magnetic flux

density<sup>1</sup> created by a current flow in conductors and the exploitation of a functional dependence between the measured field and the current value. The fundamental dependence that describes the relationship is the Biot-Savart law:

$$\vec{B}(\vec{r}) = \frac{\mu_0}{4\pi} \int \frac{\vec{j}(\vec{r}') \times (\vec{r} - \vec{r}')}{\|\vec{r} - \vec{r}'\|^3} d^3r' \quad (\text{II.1})$$

with the vacuum permeability  $\mu_0 = 4\pi \cdot 10^{-7} \text{ N/A}^2$ , the current density  $\vec{j} [\text{A/m}^2]$  and the position vectors  $\vec{r}$ ,  $\vec{r}'$  of the measurement point and the conductor element, respectively. For an infinitely thin wire, the current density reduces to:

$$\vec{j}(\vec{r}) d^3r = I(\vec{r}) d\vec{l} \quad (\text{II.2})$$

with the current vector  $\vec{I}$  and the length element of the wire  $d\vec{l}$ . This thus results in:

$$\vec{B}(\vec{r}) = \frac{\mu_0}{4\pi} \oint \frac{I(\vec{r}') \times (\vec{r} - \vec{r}')}{\|\vec{r} - \vec{r}'\|^3} d\vec{l} \quad (\text{II.3})$$

and for the specific case of an infinite wire the angular component of the magnetic field yields the magnitude of the field at a given distance to the current:

$$B_\theta(I_0, d) = \frac{\mu_0 I_0}{2\pi d} \quad (\text{II.4})$$

with the current magnitude  $I_0$  and the distance  $d$  between the conductor and the point of interest. This relation can be used to estimate the field magnitude around a (single) power line of the electrical distribution grid. The field magnitude that results for the typical root-mean square (RMS) current values ( $I_{\text{RMS}} = 1000 \text{ A}$ ) and a single conductor at a minimum distance of  $d = 25 \text{ mm}$  (the typical radius of cable insulations in this current range) is  $B = \frac{\mu_0 I}{2\pi d} = 8 \text{ mT}$ . This can be used as a reference value for the discussion of magnetic field sensor technology in section II.2. The current value may, however, increase by a factor of 10 in case of malfunctions, so that a resilience of a field sensing technology with respect to magnetic shocks also becomes a relevant criterion. Depending on the magnitude of field created by the source under examination, the geomagnetic

---

<sup>1</sup>The difference between the magnetic field  $\vec{H}$  and the magnetic flux density  $\vec{B}$  should be kept in mind. They are related via the vacuum permeability  $\mu_0$  and the magnetization  $\vec{M}$  by  $\vec{B} = \mu_0(\vec{H} + \vec{M})$ . Their respective units are Tesla, [T] and Ampere per meter, [A/m]. The magnetic flux density is the measurement quantity. The exact relation between the flux density and the field further depends on the material, which the field penetrates. In linear and isotropic media, it is possible to relate  $\vec{M} = \chi_m \vec{H}$  using the magnetic susceptibility  $\chi_m$  and to define the magnetic permeability  $\mu_r = 1 + \chi_m$ , in order to write  $\vec{B} = \mu_r \mu_0 \vec{H}$ .

---

field may also need to be taken into account. Although it is not critical for current measurements in the electrical distribution grid, it has a significant impact on lower level DC measurements, such as the laboratory measurements presented in Ch. 5. This field is of the order of  $B_{\text{GMF}} \approx 50 \mu\text{T}$  and exhibits a daily variation of approximately  $(\pm 0.1) \mu\text{T}$  (e.g. through solar winds) as well as spatial variations.

Eq.II.4 indicates that an individual magnetic field sensor can be employed as a current sensor. While providing the advantage of contactless current determination, magnetic field measurements are faced with the fundamental issue of differentiation between field sources. This basic requirement applies to most instances of magnetic field measurements, which are perturbed either by additional field sources in the immediate environment or simply by the presence of the geomagnetic field. The measurement case at hand provides an extreme example of these complications, since the three-phase nature of electrical power transmission already dictates that, for the examination of a conductor of interest, two perturbing conductors are located in (close) proximity. Further sources of magnetic fields (of diverse forms and magnitudes), e.g. transformers, are also standard components of power transmission grids. Their relative position and thus their impact will depend on the specific installation site. In the context of current determination, the ability to distinguish the magnetic field of the current/conductor of interest from other sources is discussed as the **geometrical selectivity** of the measurement method.<sup>[4]</sup> There are two distinct solutions to obtain geometrical selectivity for current measurements. On the one hand, there are **dedicated** (contactless) **current sensors** that measure the field along a closed path around the conductor in order to achieve geometrical selectivity. The second category is based on the use of individual field measurements. Since these do not provide geometrical selectivity in environments of multiple (perturbing) field sources, it is nonetheless necessary to conceive special measurement principles, usually associated with specific geometrical configurations using a given number of sensors, in order to achieve geometrical selectivity between the source(s)/conductor(s) of interest and the perturbing source. For these cases, the current measurement process is thus replaced by a combination of magnetic field measurements and the theoretical framework/measurement configuration used to deduce the current value from these. Current sensing solutions can thus be classified in two distinct categories, with fundamentally different implications. The inherent structure of the two categories is illustrated in Fig.II.1. For the dedicated current sensors, the sensing technology itself defines the measurement principle, the two aspects are interweaved and inseparable. Examples for this are the shunt resistors mentioned above or the Rogowski coil which will be presented below. The second category, illustrated on the left-hand-side of Fig.II.1, includes those measurement methods for which the measurement principle and sensing technology present two independent

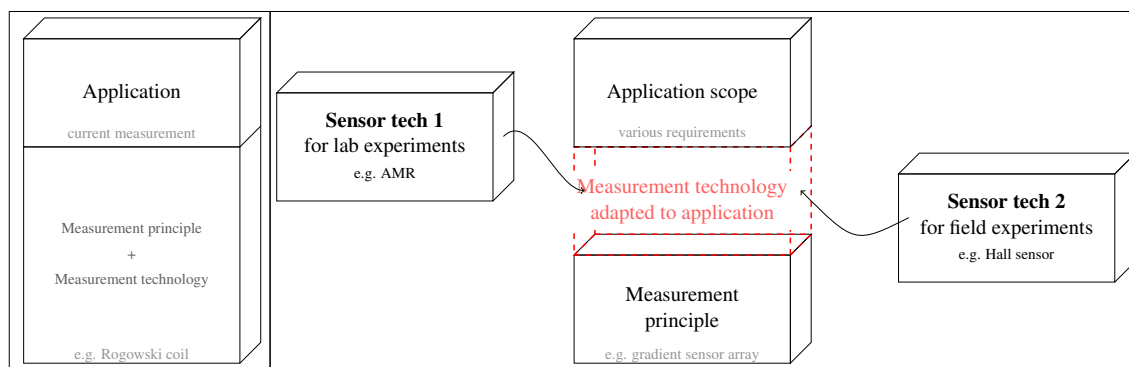


**Figure II.1:** The two categories of contactless current measurement methods. Depending on the method, the measurement principle and technology are either essentially inseparable and the solution is dedicated to current measurements (left) or they present individual building blocks (right) to meet the application requirements.

and fundamental building blocks, which are combined to stem the application task. Herein, the **measurement principle** defines the relation between the magnetic field measurements and the current magnitude, while the **measurement technology** serves an enabling function that allows the implementation of the principle. The two elements are essentially independent, i.e. a measurement principle can be implemented using various, interchangeable field sensing technologies. The specific technology is then selected based on the measurement conditions of an application case and the requirements that the principle implies. The measurement principle thus acts as the basis on which the measurement technology rests, in order to bridge the gap between theory and application. This latter category of contactless current determination has a characteristic advantage over the first group of methods and this is the flexibility. Once the measurement principle has been developed and proven, i.e. the transfer function between the magnetic field measurements and the current has been established, the measurement method is still free to evolve and to adapt to specific application cases using appropriate sensor technology. In effect, these methods can also benefit from future developments in sensor technology, i.e. miniaturisation or reduced power consumption. Furthermore, due to the independent nature of the measurement principle, it can also stand alone and be used in other application areas (just like the sensor technology is also used in contexts other than current determination), e.g. magnetic field characterization.

The two categories of contactless current measurement methods provide the outline for the following considerations, i.e. existing (contactless) current measurement principles, for which the measurement principle depends on a certain sensing technology will be reviewed first along with some concepts that are central to their evaluation. This will be followed by a discussion of individ-

ual magnetic field sensing technologies, which can be used to implement measurement principles that are functional with any kind of measurement technology (evidently with varying degrees of suitability for different applications). These sensing configurations are presented alongside the sensor technology. Ultimately, both approaches, whether it is the use of dedicated current sensors or the application of a measurement principle in combination with a suitable field sensing technology, will be judged according to their suitability for current measurement in the electrical grid. Before the solutions are presented in the following two sections, it is thus meaningful to consider the relevant parameters according to which they will be assessed:

- **Range:** defines the limits within which the sensor can be employed for field/current measurements. A given field range for a magnetic sensor in Tesla can easily be translated into a current range, if the measurement distance is known, using the formulas provided above.
- **Precision:** with which the field/current value can be determined. For individual magnetic field sensors, this is usually provided as a percentage of the full-scale value (% F.S.), while commercial current sensors for the electrical grid are categorized in terms of precision classes defined by international standards.
- **Bandwidth:** the frequency range in which the current sensor is functional.
- **Noise:** undesired, random variation of the measurement signal. Often ultimately defines the resolution (smallest detectable variation of the magnetic field) of a sensor (in terms of the signal-to-noise ratio) and is generally frequency-dependent.

With these parameters in mind, it is now possible to examine the individual current sensing solutions, beginning with dedicated current sensors.

### II.1 Dedicated current sensor technology

As indicated by the denomination, the sensors that can be classified in this category are inherently designed for current measurement tasks and are not suitable for other applications. Shunts are thus also part of this category, but the focus here will be on the contactless solutions that are utilized for current measurement in electrical grids. Their measurement principle will be described in this section and a representative commercial product is presented in the comparison of Tab. II.3.

**Current transformers** Current transformers use a multi-turn secondary winding to pick up the field created by the conductor, which acts as a single-turn primary winding. The secondary coil

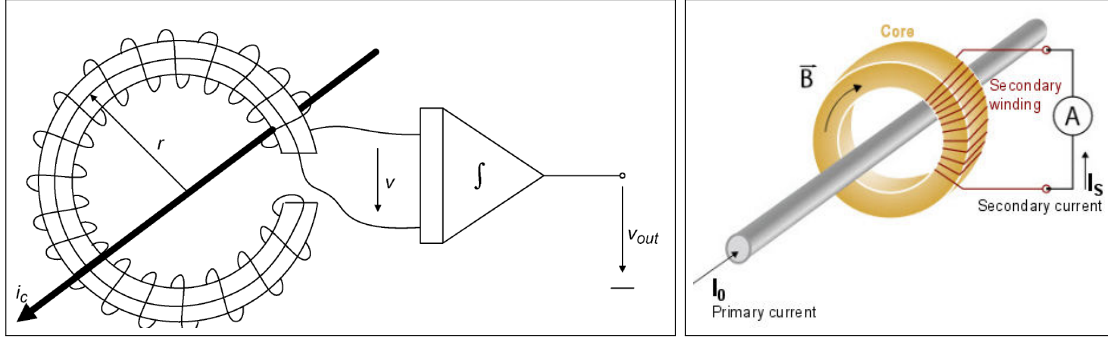


Figure II.2: left: Schematic of a Rogowski coil.<sup>[5]</sup>; right: Schematic of a current transformer.

is wound around a core material of high relative permeability and placed around the conductor of interest. For an ideal transformer, the flux in both windings,  $\Phi_P$  and  $\Phi_S$ , are equal and the secondary current is proportional to the current in the primary conductor. The number of turns defines the transformation ratio. A schematic of a current transformer (CT) is provided in Fig. II.2. In practice, the second winding is used to compensate the flux generated by the primary current and the current that drives it is proportional to the primary current. CTs cannot measure DC currents and also exhibit significant deviation from the linear behaviour at high duty cycles. Their advantages include the low cost, the robustness, the autonomous operation principle and an output signal that is directly compatible with analog-to-digital converters.<sup>[5]</sup>

**Rogowski coil** The operating principle of Rogowski coils rests on Ampère's circuital law, i.e. the inhomogeneous Maxwell equation of magnetostatics, which states that the integral of the magnetic field along a closed path around the conductor is proportional to the current:

$$\oint \vec{B} d\vec{l} = \mu_0 I_0 \quad (\text{II.5})$$

For the implementation, a (usually circular) air coil ( $\mu_r=1$ ) is placed around the conductor and an integrator is used to obtain the (AC) current waveform. Specifically, the time-derivative of the magnetic flux  $\Phi$  is related to the current  $I$  via the mutual inductance  $M$  between the conductor and the coil, thus producing a proportional voltage  $V$ :

$$V(t) = \frac{d\Phi(t)}{dt} = -M \left( \frac{dI(t)}{dt} \right) \quad (\text{II.6})$$

## II.1. Dedicated current sensor technology

---

The coil consists of primary and secondary windings with different number of turns (single and multiple respectively). Rogowski coils can – therefore – only be employed to measure AC currents and transients or changes in DC current. An integrator (single-chip digital versions are available) is used to obtain the AC flux waveform. The coil does not contain any ferromagnetic materials, so that excellent linearity and a large dynamic range are achieved.<sup>[6]</sup> However, the required single integrator increases the power consumption of the sensor and can suffer from offset drift in long-term measurements. The attainable precision of Rogowski coils is usually dominated by the positioning accuracy of the conductor within the circular coil. Under ideal conditions, i.e. if the mutual inductance is constant along the coil, the measurement is position-independent. The mutual inductance is given by

$$M = \mu_0 \cdot n \cdot S \quad (\text{II.7})$$

with the turn density  $n$  and the core cross-section  $S$ . Therefore, the measurement is precision independent if the core has a constant cross-section, the windings are perpendicular to a imaginative line along their centres and if the turn density is also constant. For manufactured Rogowski coils, the error introduced by positioning variations is usually  $\leq 1\%$ , but may reach up to 3% if the conductor is positioned near the gap in split-core coils. A Rogowski coil with an integrator is displayed in Fig. II.2. Rogowski coils are available from various manufacturers, for example, PEM offers the *RCTi-3ph*, a flexible AC current transducer that can be clipped around all three phases of a power transmission line, measures currents up to 50 kA at a bandwidth of 1 MHz and provides an accuracy of  $\pm 1\%$  (of the reading).<sup>[7]</sup> Another interesting commercial product, is offered by LEM. Their PRiME current transducer consists of two concentric Rogowski coils around a conductor on a PCB. The PCB provides a more precise geometry and the two coils are used to compensate the virtual perpendicular loop. The PRiME product is also an example of a split-core solution, since a gap is introduced into the circular coil, in order to allow for the the insertion of a conductor and to thereby enable installation on existing power cables (example products: LEM AP and APR range, precision : 1%, linearity: 0.5%).

After reviewing the most common dedicated current measurement methods, for which the measurement technology is also the measurement principle, it is now possible to make the transition to those that use a combination of a measurement principle and suitable measurement technology, as illustrated in Fig.II.1. For this purpose, the different technologies for magnetic field sensing, which provide the intermediate building block that 'enables' the measurement principle, will be introduced first, followed by a presentation of possible configurations that allow for current measurement using these sensor solutions by establishing a degree of geometrical selectivity.

At that point, the discussion will also return to the dedicated solutions discussed above, since a combination of CTs or Rogowski coils with magnetic field sensors provides a practical solution, primarily due to the extension of the bandwidth of the current sensor up to DC measurements.

## II.2 Magnetic field sensor technology

Magnetic field sensing can either involve the determination of the scalar magnitude of the magnetic field (which could be exploited for current determination using Eq.II.4), or the vector components of the field, which are related to the current in the conductor via Eq.II.1. However, a single sensor that performs a punctiform, vectorial measurement of the magnetic field is insufficient for current measurements, since it cannot discriminate between the fields created by different field sources in a multi-source environment. As described above, in order to achieve geometrical selectivity with one or a set of magnetic field sensors, it is necessary to conceive and implement a suitable measurement principle that achieves geometrical selectivity on the basis of the sensor performance parameters. These measurement principles are often closely related to specific geometrical arrangements, in order to obtain the desired selective current measurement. Such (existing) configurations are discussed toward the end of this section. A novel measurement principle for sensor arrays is presented with this thesis and will be detailed in the following chapter. Since the developed measurement principle rests on the spatial characterization of the field gradient, it consequently requires vector field measurements. The sensor technologies which enable a determination of the vector magnetic field at the required precision, frequency and stability are thus examined in the following. The relevant characteristics for the single sensors which compose the array are range, precision, noise and bandwidth as well as the respective stabilities of those parameters, especially regarding variations with temperature or over time.<sup>[6]</sup> In this section, the various magnetic field sensing technologies will be reviewed, followed by a description of sensing configurations that provide geometrical selectivity and allow for the application of the sensor technologies for current sensing.

### II.2.1 Hall effect sensors

In 1879, Edwin Hall discovered that the trajectories of electrons traversing a thin sheet of conductive material are diverted by a magnetic flux density that penetrates the sheet. This results in a voltage  $V_H$  in the direction perpendicular to both the current flow and the field. A schematic of the setup for the determination of the Hall voltage is provided in Fig. II.3. For a given current  $I$

## II.2. Magnetic field sensor technology

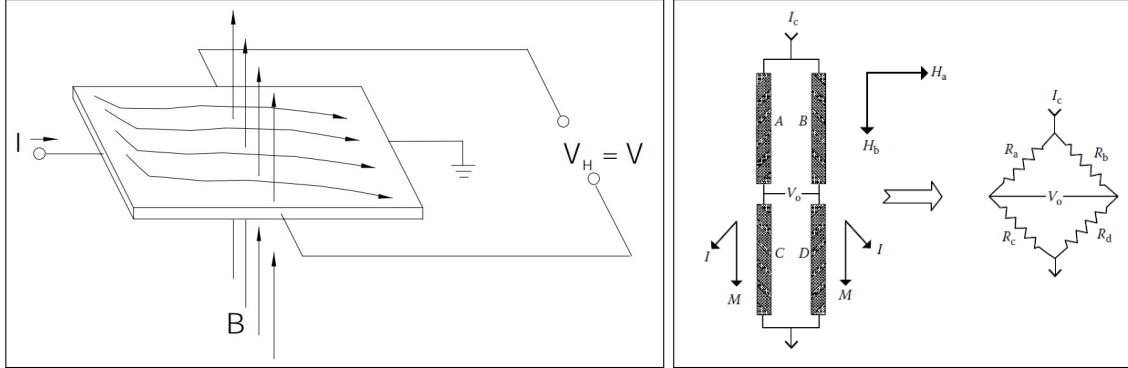


**Figure II.3:** Schematics to illustrate the operating principle of magnetic sensors based on the Hall effect (left) and an AMR sensor using a Wheatstone bridge.

through the sheet and a field  $B$ , this voltage is given by:

$$V_H = R_H \frac{BI}{d} \quad (\text{II.8})$$

with  $d$ , the thickness of the sheet and  $R_H$  the material-dependent Hall coefficient. Hall effect sensors require a constant and stable current of charge carriers. Materials that are used in Hall sensors are characterized by the charge of the current carrier and the carrier density. Common materials include indium antimonide (InSb), indium arsenide (InAs) and gallium arsenide (GaAs). Hall sensors find widespread application in a variety of commercial products, are low-cost, but do not reach the quality of other technologies in terms of noise characteristics ( $100 - 1000 \text{ nT}/\sqrt{\text{Hz}}$ ) and precision. Hall sensors can be used for punctiform measurement of the magnetic field, or as a part of a current sensor in a gap in a ferromagnetic ring core (field concentrator). Here, they are usually employed with feedback compensation, as will be discussed in more detail during the presentation of configurations for current sensing below.

### II.2.2 Magnetoresistors

The dependence of the resistance of a ferromagnetic material on the external magnetic field, the magnetoresistance effect, was first observed by William Thomson (Lord Kelvin) in the mid-19<sup>th</sup> century. Today, magnetoresistive sensors are commonly made of Nickel-iron alloys (permalloys), since these exhibit the greatest change in resistance with field (approximately 5%). This resistivity change is anisotropic and thus depends on the angle  $\alpha$  between the detected field and the current

flow in the resistor:

$$R(\alpha) = R_0 + \Delta R \cos^2(\alpha) \quad (\text{II.9})$$

where  $R_0$  is the resistivity for  $\alpha = \pi/2$ . The anisotropic properties depend, e.g., on the fabrication process and it is possible to exploit this dependency to produce thin permalloy strips with highly uni-axial anisotropic characteristics (using magnetizing field during film deposition). The characteristic is employed in anisotropic magnetoresistance (AMR) sensors. Typically four AMR sensors are combined in a Wheatstone bridge, in order to measure the voltage gradient and to thereby enhance the output signal and to reduce sensitivity to (homogeneous) external perturbations. This configuration also allows a determination of the orientation of the magnetic field (each element of the bridge has a characteristic change of resistance  $\propto \cos^2(\alpha)$ , with  $\alpha$  denoting the angle between the current flow through the conductor). The bridge also serves to compensate the temperature variation of the electric resistivity. A schematic of the measurement principle is provided in Fig. II.3.<sup>[8]</sup> Similar configurations are possible with sensors based e.g. on giant magnetoresistance (GMR) or tunnelling magnetoresistance. The entire family of magnetoresistors is commonly referred to as XMR current sensors. In comparison to AMR sensors, GMR sensors provide an increased detection limit, since their resistance can vary up to 12.8% under the influence of external magnetic fields.<sup>[5]</sup> In general, XMR sensors offer good resolution (nT range) and precision (10  $\mu$ T), however, they are sensitive to magnetic shock and impose a rather high power consumption (up to 70 mW for AMR sensors).

Before the focus is shifted to the fluxgate technology, which provides many advantages and which is of central interest for this thesis, the following field measurement technologies should also be mentioned along with their specific shortcomings with respect to applications in the electrical grid:

- **Giant magnetoimpedance sensors** GMI is based on large variations of the impedance of soft, amorphous metals when exposed to magnetic fields. The effect was discovered in 1994, but the sensor development based on this effect has only emerged over the past decade. For measurement, ribbons of e.g.  $\text{Co}_{67}\text{Fe}_4\text{Cr}_7\text{Si}_8\text{B}_{14}$  are annealed and wound around the conductor of interest. GMI sensors suffer from a stronger temperature drift than AMR or fluxgate sensors. Due to their lower level of maturity, there are currently no commercial products for current measurement that employ GMI sensors, but their future development should be monitored closely<sup>[6]</sup>, since they present a lively field of research, noticeably also pursued at G2Elab<sup>[9]</sup>, and their performances are gradually approaching those of fluxgate sensors.

- **Superconducting quantum interference detectors (SQUIDs)** have been developed specifically for the detection of very small fields (fT) and are otherwise expensive, complex and very sensitive to external sources. They are thus used predominantly for medical applications (e.g. to measure the magnetic field of the brain).
- **Magneto-optical sensors** are almost exclusively based on the Faraday effect, according to which the plane of polarization of light is rotated as it passes through a transparent medium in parallel to a magnetic field. For current measurements, an optical fibre is wound around a current-carrying wire. Measurement preparation and the detection of the polarization using a polarized light source and an polarization analyser make this method very complex and expensive. The results are, however, very impressive. For example, ABB Sweden has produced magneto-optical sensors which measure currents above 23 kA with a relative error of  $\pm 0.15\%$ .<sup>[10]</sup>

### II.2.3 Fluxgate technology

The term fluxgate denotes the concept of the technology, which serves to transduce the magnetic flux to a voltage, exploiting its proportionality to the rate of change of the flux (Faraday's law). For this purpose, a combination of an excitation and a detection coil are wrapped around a high-permeability core to measure the variation in flux density. In principle, the excitation coil creates a calibrated, variable field (via an AC current) that periodically saturates the core, so that its relative permeability is either very close to 1 (in air, exactly 1 for vacuum) or equal to the high value of the core material. As a result, the detection coil observes the rate of change of flux density of the total field. Without an external field (or no field component along the axis of the detection coil), this results in a symmetrical hysteresis curve for the detection coil and the induced flux and voltage contain only odd harmonics. The calibrated AC field is then shifted by the presence of an external field along the detection axis, thus breaking the symmetry of saturation of the core and introducing even harmonics. This shift can be exploited to determine the field. Phase-sensitive detectors and amplifiers can be used to extract the second (or fourth) harmonic component of the excitation frequency. The amplitude of the voltage measured using the detection coil is proportional to the field magnitude, while the phase indicates the orientation of the field. The effect of the magnetic field on the magnetic permeability and voltage signal is illustrated in Fig.II.4. The induced voltage  $V$  can be described analytically using the following expression:

$$V(t) = nS \frac{dB}{dt} = nS\mu_0 H \frac{d\mu_e(t)}{dt} \quad (\text{II.10})$$

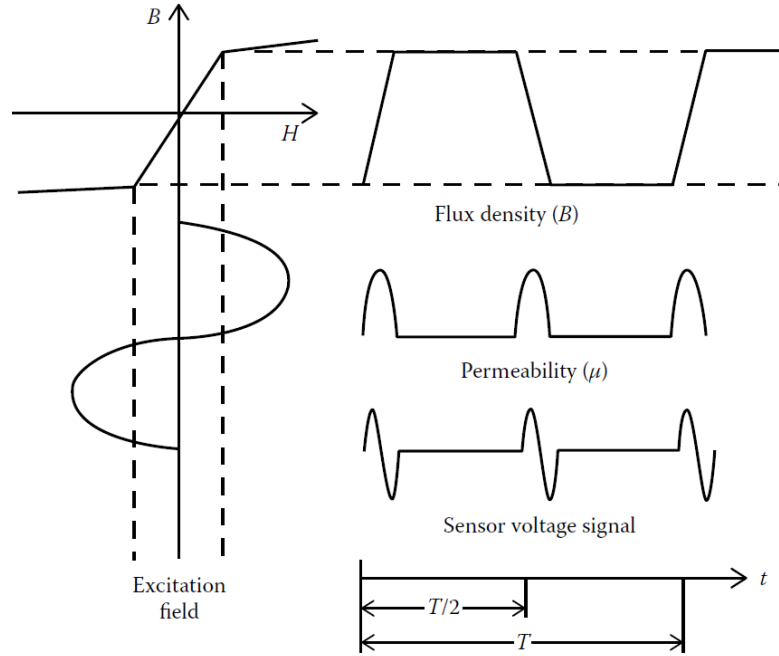


**Figure II.4:** Effect of the field created by the excitation field on the magnetic flux density and permeability of the core, as well as the resulting voltage pulses picked-up by the detection coil.<sup>[10]</sup>

with the geometrical properties of the detection coil (number of windings  $n$ , cross-sectional area  $S$ ), the relative permeability  $\mu_e$  of the toroid and the induced magnetic flux density  $B$ . In practice, two magnetic cores are normally used and excited in opposite directions, in order to compensate the coupling of the excitation energy into the system. A third coil, placed through the two cores, is also used in combination with a servo amplifier, to create a feedback field  $H_{fb}$  that compensates the external field  $H_e$ , i.e. to maintain the second harmonic contribution in the detection coil in the near-zero, and thus in the linear part of the magnetization curve of the toroid. As a result, fluxgate sensors provide excellent linearity/sensitivity across a broad detection range and the operating principle makes the technology very robust against magnetic shock. To this end, the field  $H_e$  is linked to the voltage via a transfer function  $k_{vh}$ . This voltage signal is amplified and converted to a feedback current  $I_{fb}$  which is driven through the feedback coil to induce the feedback field  $H_{fb}$ . The overall transfer function for the circuit then becomes:

$$V_0 = \frac{Ak_{vh}H_e}{1 + (k_{hi}Ak_{vh}/R_{fb})} \quad (\text{II.11})$$

## II.2. Magnetic field sensor technology

Sensor technology	Sensor parameters			
	Range	Noise [ $/\sqrt{\text{Hz}}$ ]	Bandwidth	Comment
Hall effect	10 $\mu\text{T}$ – T	100 nT	DC – 100 kHz	suitable for large fields ( $> 1$ T)
Magnetoresistance	1 nT – mT	10 nT	DC – 10 MHz	sensitive to magnetic shocks
Magnetoimpedance	0.1 $\mu\text{T}$ – mT	1 nT	DC – 10 kHz	less mature, competitive at higher frequencies ( $> 100$ Hz)
Fluxgates	0.1 nT – mT	10 pT	DC – 1 kHz	considerable power consumption
Magneto-optical	10 $\mu\text{T}$ – 100 T	1 pT	DC – 100 MHz	high power consumption
SQUID	1 pT – mT	2 fT	DC – 1 GHz	high power consumption, maximum performance at low $T$

**Table II.1:** Comparison of magnetic field sensor technology.<sup>[10,12,13]</sup> Parameters are provided as indications for comparison of sensor technologies, actual values vary for specific products.

with the amplification factor  $A$ , the feedback resistance  $R_{fb}$  and the transfer function  $k_{hi}$  between feedback current and field. Since the amplification factor should naturally be as high as possible, i.e.  $A \gg 1$ , this can be simplified to

$$V_0 = \frac{R_{fb}}{k_{hi}} H_e \quad (\text{II.12})$$

Since the two remaining factors can be controlled easily, the circuit can be used to obtain highly stable measurements, e.g. an accuracy of 1% in the temperature range of  $-80^\circ < T < +80^\circ$ . The sensitivity of the sensor can be improved by increasing the number of windings or the excitation frequency. A miniaturisation of fluxgate sensors, therefore, leads to large excitation frequencies, e.g., a classical sensor with a diameter of 2 cm has an optimal excitation frequency of 10 to 20 kHz, while an integrated fluxgate with a 1 mm long core has an optimum frequency of up to 1 MHz. Large frequencies increase parasitic capacitive coupling.<sup>[11]</sup> Due to their high precision and large dynamic range, fluxgate sensors have been used in a large variety of applications, for example, in the study of the earth-magnetic field or space.

The precision of fluxgate sensors is superior to other sensors in most application areas and the remaining inaccuracy can often be explained by the offset and its stability with temperature and time. The precision of fluxgate sensors can suffer both an intrinsic offset, which is due to imperfections in the magnetic core and which can be characterized after fabrication, and a change of offset due to parasitic effects. The latter can be due to false signal contributions, originating, e.g., from distortions in the excitation signal or a magnetostrictive signal. A detailed study of these offset effects is provided by Ripka *et al.*<sup>[11]</sup> The offset depends on the fabrication material

and process and usually lies in the nanotesla range, which is still very good in comparison to other sensing solutions.

A summary of sensing parameters for the various technologies is provided in Table II.1. The values are indicative and provide a first level of differentiation, which can be helpful in selecting potential candidates for a specific application case. The actual parameters of individual commercial sensors vary strongly even amongst a given technology. Precision values are not provided in the table, since this parameter in particular depends on the implementation of the sensing technology, and will thus be discussed in more detail for commercial current sensors below.

Given the magnetic field sensing solutions presented above, it is now possible to examine the sensing configurations usable in current sensing or other multi-source environments. This will also permit a comparison of these compound solutions (sensor technology + measurement principle) with dedicated current sensors that do not employ magnetic field sensors and which were presented in the previous section.

#### **II.2.4 Sensing configurations for geometrical selectivity**

The methods/sensing configurations that employ punctiform magnetic field sensors for current measurement and attain geometrical selectivity in a multi-source environment can be categorized as measurement of the magnetic field along a closed path around the conductor or the use of sensor arrays. These combinations of a field sensing technology and a measurement principle (that defines the sensing configuration) are represented on Fig.II.1, left. The former method exploits Ampère's circuital law to determine the current and employs a field concentrator, i.e. a magnetic core, which is placed around the conductor. The (usually) ring-shaped core concentrates all field lines from the conductor, and the flux measurement is thus largely independent from the exact position of the conductor, while the sensitivity is also increased. Depending on the flux measurement method, the core can either be gapless or a gap can be introduced in the core, so that, e.g. a Hall sensor can be placed in this gap to determine the field. The parameters of the measurement method will then depend both on the characteristics of the magnetic field sensing technology and those of the core. Gapless concentrators provide better geometrical selectivity, but also suffer from saturation, since the field  $H$  in the central line of the core is proportional to the product of the current  $I$  and the number of windings  $N$ : The following configurations are common choices that utilize the previously presented magnetic field sensing technology to determine the current flow in a conductor. As explained above, accurate current measurements are only obtained using a combination of the sensing technology and the measurement principle (configuration). All currently available

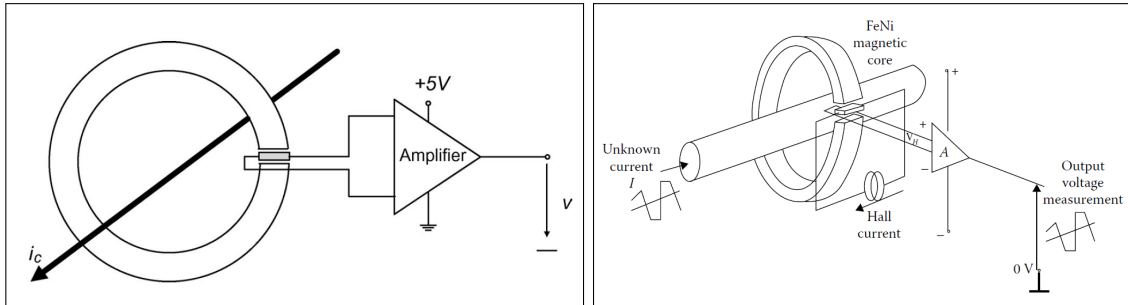


**Figure II.5:** Schematics of open-loop (left) and closed-loop (right) sensing configurations using magnetic field sensors in the gap of the magnetic core.

commercial products revert to the concept of measuring the field along a closed path around the conductor, using a magnetic core as a field concentrator, and measuring the concentrated field with one of the magnetic sensor technologies presented above to determine the current magnitude. This can be implemented in an open- or closed-loop configuration or in combination with a current transformer or Rogowski coil. These configurations used in commercial products will be detailed below, followed by other sensing configurations that have been developed to obtain geometrical selectivity, but that have not reached sufficient maturity for commercialization to date.

**Open-loop configuration** Open-loop configurations, such as surface-mounted magnetoresistors above a conductor of interest provide simple and cheap alternatives but often lack accuracy or require in-situ calibration. Their geometrical selectivity is generally limited and their positional dependence rather pronounced. The geometrical selectivity can, however, be increased using the sensing configuration provided on Fig. II.5, left. Here a magnetic core is placed around the conductor and the magnetic field sensor measures the field magnitude in a gap that is introduced in the core. The measurement principle then also depends on the properties of the magnetic core, and losses within the core can limit the bandwidth of the measurement method.

**Closed-loop configuration:** Closed-loop configurations present an improvement with respect to open-loop technology, since, similarly to the principle of the current transformer, a secondary winding is introduced to compensate the flux inside the transformer. This reduces the impact of thermal drift, improves the linearity and geometrical selectivity, but also introduces an offset that results from the increased number of components in the circuit (e.g. amplifier). An exemplary setup is provided in Fig. II.5, right.

		Sensor technology	Sensor parameters			
			Range	Precision	Bandwidth	Power consumption
dedicated current sensor	contact	Shunt	mA – kA	0.1 – 2%	DC – MHz	mW – kW
	contactless	Current transformer	A – kA	0.1 – 1%	kHz – MHz	mW
		Rogowski coil	A – MA	0.2 - 1%	kHz – MHz	mW
magnetic sensor + core	contactless	Closed-loop AMR	A	0.5 – 2%	DC – kHz	mW
		Closed-loop fluxgates	A	0.001 – 0.5%	DC – kHz	mW – W
		Closed-loop Hall effect	A – kA	0.5 – 5%	DC – kHz	mW
		Fiber-optic	kA – MA	0.1 – 1%	kHz – MHz	W

**Table II.2:** Performance comparison for current sensor solutions.<sup>[5]</sup>

**Magnetic field sensors with current transformers/Rogowski coils:** Since they are based on the same physical law as current transformers and Rogowski coils, it is also possible to replace the simple magnetic yoke with a CT or Rogowski coil, in order to combine the advantages from both techniques. The CT or Rogowski coil then ensures a high precision and bandwidth, while the use of a magnetic field sensor allows for a determination of DC or low-frequency currents. An exemplary implementation of this combination is provided by the “Eta” sensor from LEM, which uses a Hall sensor in the gap of a CT and is available at a comparable price with respect to closed-loop Hall sensors.<sup>[5]</sup> It should be noted that although the use of feedback circuits or field compensation windings is indispensable for precise and geometrically selective measurements, it also increases the complexity of the measurement circuit, its power consumption (up to several mW) and the price.

**Configurations for fluxgate current sensors:** While the size of the magnetic core and coils must be minimized if the fluxgate principle is to be used for punctiform magnetic field measurements, magnetic cores placed around the conductor prove to be the optimal configuration for current measurements. The core again serves to concentrate the field from the primary current which is then compensated by the secondary winding. It is also possible to conceive a configuration without a pick-up winding and to deduce the current from the signature of the excitation current<sup>[5]</sup>. The larger core does however require more time and energy to be driven between posi-

## II.2. Magnetic field sensor technology

Sensor technology	Commercial product	Sensor parameters				Dimensions [mm]
		Rated current	Precision (class)	Bandwidth	Power consumption	
Current transformer	<i>EATON HF7A</i>	2 kA	0.5%	50 Hz (rated)	6 W	146x106x52 for aperture $\varnothing 65$
Rogowski coil (flexible coil)	<i>PEM RCTi/2000</i>	2 kA	1%	0.6 Hz – 600 kHz	0.4 W (max)	coil $\varnothing 219$ electronic box: [138x60x28]
Closed-loop AMR	insufficient range, no commercial product for low-voltage grid					
Closed-loop fluxgates	<i>LEM ITC 2000-S/SP1</i>	2 kA	0.5%	DC – 27 kHz	5 W (current-dependent)	[191x184x100] for aperture $\varnothing 63$
Closed-loop Hall effect	<i>ABB ES 2000</i>	3 kA	$\pm 0.5\%$	DC – 1 kHz	0.6 W	[110x95x35] for aperture $\varnothing 40.2$
Fiber-optic	<i>ALSTOM F3 NXCT</i>	100 A – 4 kA (20 fiber turns)	0.1%	DC – 20 kHz	60 W	wrap-around fiber + sensor box: [400x350x130]



**Table II.3:** Performance comparison of exemplary commercial products for the low-voltage grid and the different contactless measurement technologies. Images for current sensors are provided in the order of appearance in the table.

tive and negative saturation, which limits the bandwidth of the configuration. Commercial sensor configurations therefore often use a combination of a fluxgate and a current transformer to extend the bandwidth.

The three configurations using magnetic field sensors described above are used for commercial products that are applicable for grid applications. An overview, comparison and preliminary conclusion of existing commercial current sensing solutions will thus be provided at this point, before the description of other sensor configurations that provide a geometrical selectivity which offer potential for commercialization. A general overview of the measurement methods that are (theoretically) applicable for grid applications is provided in Tab. II.2. The methods are classified according to the distinction introduced at the beginning of this chapter, which is illustrated in Fig. II.1. The sensor parameters confirm that the listed technologies meet the necessary requirements, i.e. measurement of currents with a nominal current of 1 kA at 50 Hz, and are thus potential

candidates for grid applications. As explained above, only contactless measurements present a feasible solution for current measurements in the power grid. Representative commercial products for contactless current measurement methods are thus provided in Tab. II.3. Here the precision is provided as accuracy classes defined by international standards. In comparison to the overview in Tab. II.2, commercial products have a much larger power consumption. This is due to the additional power consumption of signal processing electronics, and for some sensors (e.g. fluxgate), the power consumption is also proportional to the measured current (field) magnitude since the current used to drive the flux compensation must be increased accordingly. Magnetoresistance sensors (even in closed-loop configurations) are not used for power grid applications due to their limited range, inferior precision compared to other field sensing technologies and their susceptibility to magnetic shock. Current transformers must be designed for a specific (rated) frequency, while the other solutions provide extended bandwidth. As detailed above, all commercial sensing technologies rely on measurements around a conductor to achieve geometrical selectivity. For cables in the centimetre range, these sensors thus have considerable dimensions. The closed-loop solutions are also available in split-core designs for easier installation: in this case the introduction of the opening for the introduction of the conductor usually results in a degradation of the measurement accuracy. The commercial products that use individual, punctiform magnetic field sensors all rely on a closed-loop principle and a magnetic core to achieve geometrical selectivity and, consequently, a sufficient precision. Another popular approach to obtain geometrical selectivity using magnetic field sensor, is the arrangement of a given number of sensors  $N$  as a magnetic sensor array. Suitable configurations are introduced in the following paragraph.

**Combination of  $N$  magnetic field sensors** An intuitive approach to current measurement with field sensors in a multi-source environment is the equidistant distribution of multiple sensors along a circular path around the conductor of interest. This thus reverts directly to an approximation of the magnetic field along a closed path and thus Ampère's circuital law, as it is exploited for sensor and core combinations described above. The precision then depends on the number of sensors  $N$  that are used to approximate the field along the path. This approach can be extended by placing two sensors within close proximity of each other at each position on the circular path that surrounds the conductor. This allows to measure the field gradient and thus to exploit the fact that the field gradient  $\Delta\vec{B}$  is proportional to  $1/d^2$  and thus decreases faster with distance  $d$  to the conductor. Hence, as long as the current/conductor of interest is closer to the measurement sensor than the perturbing sources, a geometrical selectivity is obtained. The increase in precision does not show the same improvement with the sensor number  $N$ , so that the attainable geometrical selectivity is

limited even using a gradient sensor setup. This fact is underlined by the fact that no commercial sensors based on this configuration are currently available.

Another approach to achieving increased geometrical selectivity for current measurements was developed by Di Rienzo *et al.* and uses a spatial harmonics description of the field. Spatial harmonics also represent the theoretical framework of this thesis, even though the implementation and thus the implications is/are different. In the existing work, a number of sensors is again placed equidistantly on a circular path around a conductor of interest. The decomposition of the field in spatial harmonics does however allow for an increased geometrical selectivity with respect to perturbing conductors. The configuration is provided in Fig. II.6, left. This setup allows successful suppression of the perturbation of an adjacent conductor at up to  $d_1 = 6$  cm for DC measurements and  $\pm 8$  A in the conductors using an array of 4 magnetoresistive sensors on a circular path of radius  $r = 3$  cm.<sup>[14,15]</sup> This approach will be discussed in more detail during the introduction of spatial harmonics in the following section.

In a more recent publication, the measurement method has been adapted for the effective suppression of field sources that are external to the measurement region defined around three rectangular busbars. The setup is provided on Fig. II.6, right, wherein the sensors can be placed in the region  $A_0$ ,  $A_2$  is a source-free region, and the influence of sources in  $A_1$  is effectively suppressed. The sensor positions and orientations are optimized using a D-optimality criterion and a PSO (particle swarm optimization technique).<sup>[16]</sup> The use of circular sensor arrays or other array configurations for current measurements have not yet reached the stage of commercialization.

The protection of the intellectual property at the basis of these innovative measurement methods is usually an essential step toward the industrialization. It is therefore of interest to examine a selection of patent documents that carry implications for the measurement task at hand. This will be provided in the following section.

## II.3 Patented measurement principles

Here, the emphasis is placed on patents that are relevant for the measurement method which will be developed in the following chapter. Some interesting aspects are discussed with reference to the relevant patent document in the following paragraphs.

### Sensors on circular path around conductor

Existing solutions using dedicated current sensors or arrays of magnetic field sensors (e.g. using assemblies of Hall or AMR sensors)<sup>[6]</sup> placed on a circular path around a conductor under in-

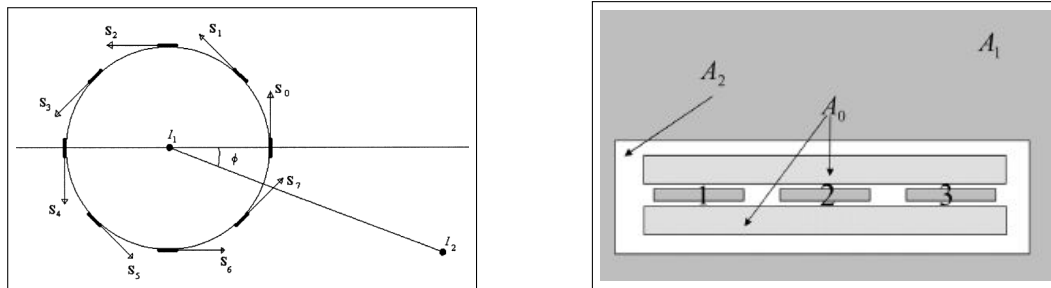


**Figure II.6:** Sensing configurations for the application of spatial harmonics decomposition for current measurement. Left: discrimination of perturbing conductor effect using sensors on circular path around conductor.<sup>[14]</sup> Right: suppression of external field sources (region  $A_1$ ) using sensors in region  $A_0$  for busbar system.<sup>[16]</sup>

investigation have been discussed above. There are accordingly numerous patents protecting these technologies.

An exemplary patent that uses a split-core solution placed around a conductor is:

*Patent US 7164263 (B2) (2007)*

**“Current sensor”**

Yakymyshyn et al./ FieldMetrics

A current sensor for applications including but not limited to DC, 50 Hz and 60 Hz power lines (or substation bus conductors) is described that consists of a plurality of magnetic field sensors oriented and located around a current carrying conductor.<sup>[17]</sup> This patent serves as an example for a large number of patents using similar measurement configurations. The drawing from the patent document is provided in Fig. II.7.

**Current determination in polyphase cable using calibration method**

*Application WO2013068360 (A1)*

*Patent FR2982672 (B1)*

**“Device for measuring currents in the conductors of a sheathed cable of a polyphase network”**

Bourkeb et al.

Although this patent responds to a different measurement task, i.e. polyphase cables in contrast to the system of three independent cables studied in this thesis, the calibration method introduced in this patent carries some interesting implications. For the measurement, at least four magnetic sensors around a central hole (for cable). The measurement geometry is provided in Fig. II.7, left.

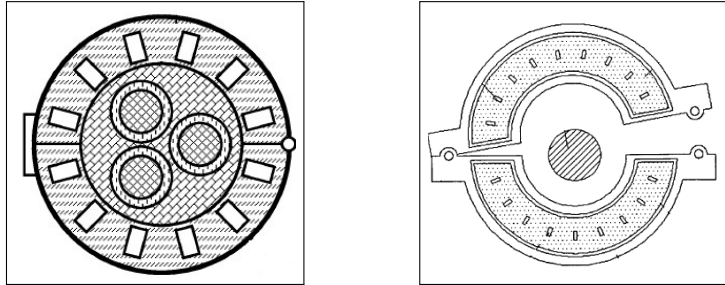


Figure II.7: left: Bourkeb et al. patent diagram; right: FieldMetrics patent diagram;

The field measurements are compared to an *a priori* library of reference matrices, calculated for various conductor positions and angular orientations of the sensors. The calculation of a residual vector allows a determination of the correct cable geometry. An example geometry is based on conductors 3 mm from the center and sensors 10 mm from the center of a multi-conductor cable. Currents of  $-0.5$  A,  $-0.5$  A, 1 A are passed through the conductors and can be determined with accuracies of 8%, 2% and  $\leq 1\%$ , respectively, for the use of  $N = 12$  sensors).<sup>[18]</sup>

This patent is primarily of interest for the task at hand, because it covers the use of a library of matrices to determine the current values from pre-determined information on the sensor measurement combinations. A similar idea was used to develop the calibration method described in the following chapter.

### Current measurement using spatial harmonics

A third patent, which shows a greater overlap with the work conducted for this thesis is the following:

*Patent EP1166132 (B1) (2006)*

#### “An improved current sensing device for low-voltage power circuit breakers”

Di Rienzo et al./ ABB

This patent is a direct result of the work by Di Rienzo *et al.* which was presented in the previous section. The measurement principle is adapted to circuit breakers and a three-phase network. To achieve the geometrical selectivity, individual sensors are distributed around the three busbars. A 2D decomposition of the magnetic field is then performed for the three-phase rectangular conductors system, in order to deduce the individual currents.

### **Current sensors besides the conductor**

Although there are no commercial products based on field sensing besides (and not around) a conductor, there are patents offering such solutions which are provided here for the sake of completeness. Their major limitation appears to be an insufficient geometrical selectivity. Furthermore, the following solutions require measurement geometries that are precisely defined and/or they do not work with non-linear conductive paths.

*Patent US8378662 (B2) (2013)*

*Patent EP 1977257 (B1) (2008)*

### **Current Sensor**

Storkey, M. / SENTEC<sup>[19]</sup>

Current sensor architecture using planar coils in close proximity to a current conductor. Detects the current gradient and uses an integrator to determine the AC current. Rejects uniform external fields, gradient magnetic fields, and fields from conductors in defined (and known) locations in close proximity.

*Patent US6642705 (B2) (2003)*

*Application EP1199573 (A3) (2002)*

### **Electric Current Sensor**

Kawase, M. /Canon Denshi<sup>[20]</sup>

A pair of magnetic detectors and a differential amplifier is used to differentially amplify two signals. The paired magnetic detectors are arranged adjacent to each other but spaced from the conductor to one side. The paired magnetic detectors have the same magnetic field detecting direction, which may be parallel or inclined relative to the magnetic field component to be measured.

*Patent EP1114325 (B1) (2002)*

*Application WO0054063 (A8) (2001)*

### **Device and Method for measuring an electric current**

Hohe, H.-P., Weber; N. / Fraunhofer<sup>[21]</sup>

Current measuring device for  $n$  conductors using  $n + 1$  magnetic sensors. Different configurations are described, the sensors are situated between the individual conductors or with at a vertical displacement from the imaginary line connecting the conductors. The sensor signals are acquired in a central processing unit that determines the current values. Requires calibration with known currents.

After discussion of the various current and magnetic field sensing technologies, relevant commercial products and patents, the landscape of state-of-the-art of sensor technologies can be completed with a short outlook on a research field that is likely to impact future sensor developments.

Recent years have seen the rise and development of micro-electromechanical systems (MEMS) which include both scaled-down solutions of existing technologies along with some interesting new developments. A brief overview is provided in the following and the reader is pointed to some relevant literature for further information. The complete picture then permits a conclusion concerning the state of the technology presented in this chapter.

## II.4 Outlook

### II.4.1 MEMS technology

In terms of current measurement and magnetic field sensing, MEMS offer the potential for significant improvement in two areas. On the one hand, they present a new class of sensors which focus on the requirement of providing miniature solutions that allow for the integration of low-cost, multi-functional devices on a single substrate/chip. On the other hand, they aim at providing autonomous solutions in combination with energy harvesting technology. These two characteristics make them interesting candidates for application in the fine-meshed monitoring of smart grids. MEMS solutions already exist in various areas, such as for gyroscopes, accelerometers, micro-mirrors or pressure sensors.<sup>[23]</sup> The primary areas of research in the domain of MEMS magnetic field sensors focus on three types of operating principles<sup>[23]</sup>, which will be discussed independently in the following. The first two categories of MEMS sensors present miniaturised versions that are based on operating principles described above but fabricated using techniques already explored in the electronics industry. The third group presents a more recent development of a measurement principle for magnetic field sensors that offers the potential for a similar miniaturisation.

- **Miniaturised fluxgate sensors:** aim to provide low-cost solutions based on the fluxgate principle. The miniaturisation of fluxgate sensors is not evident, since a reduction in size typically leads to low sensitivity and strong noise characteristics, e.g. due to the concentration of a high number of turns of the coils within a limited volume. MEMS solutions include planar sensors with flat coils, PCB-based solutions with the solenoid integrated in the tracks/vias and 3D micro-solenoids. MEMS fluxgate sensors have a range up to millitesla and offer a maximum resolution of 100 pT.<sup>[23]</sup>
- **Miniaturised Hall effect sensors:** offering a range that extends between 1  $\mu$ T and 1 T. Hall sensors on silicon substrates already find widespread application, but can impose limits on

the attainable sensitivity and resolution, so that alternatives such as polymer-based solutions are being explored. Amongst the reported devices, a tri-axial sensor based on micro-machining of silicon-on-insulator (SOI) wafers demonstrates the potential of this technology (sensitivities up to 1000 V/AT for each axis).

- Resonant sensors:** based on the Lorentz force principle. Micro-machined structures are excited at resonating modes, thus effectively amplifying the signal.<sup>[24]</sup> Many devices employ a beam structure through which a current passes and which is deflected due to the Lorentz force that acts when an external magnetic field is applied. Piezoresistive, optical or capacitive methods can be used to detect the degree of deflection of the beam. Reported ranges for these devices reach up to 1 T at resolutions up to 1 nT.

The overall dimensions of reported MEMS magnetic field sensors are typically in the range of a few mm<sup>2</sup>. The Hall sensors offer the lowest sensitivity amongst the three categories above. Sensors with low sensitivities can still be sufficient for applications that rely on the mere detection of the presence of a magnetic field and/or its orientation (e.g. position sensing, vehicle detection). Micro-fluxgate sensors are the most promising for high sensitivity, low noise applications and devices have already been developed for medical applications. The use of piezoelectric materials, often in combination with magnetostrictive materials, to generate a voltage proportional to the magnetic field is also a popular research topic in the field of MEMS sensor technology, however,

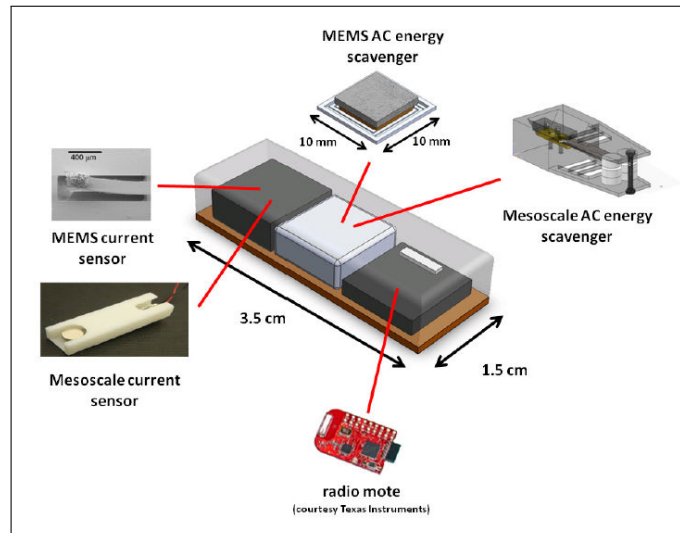


**Figure II.8:** Self-powered MEMS current sensor; including cantilever-based current sensor and AC energy harvester.<sup>[22]</sup>

this technology is not sufficiently mature for use with the measurement conditions at hand.<sup>[25]</sup> Miniaturisation also offers the possibility for a significant reduction of the power consumption. In this respect, the strong overlap between research on MEMS for sensors/actuators and MEMS for energy harvesting offers the potential for a combination of the two applications. This would allow the development of autonomous current sensing nodes, which could be distributed throughout the grid at low cost and installation efforts and would require very little maintenance. The potential of the combination of the same MEMS technology for both current measurement and energy harvesting is illustrated by the work of Paprotny *et al.*<sup>[26,27]</sup>, who have used a piezoelectric layer and a magnetic cantilever beam with a permanent magnet layer, tuned to the current frequency. The cantilever beam is optimized for energy harvesting in one unit and for AC measurement in another. In the end the entire device, including a radio transmission unit, measures  $10 \times 10 \times 4$  mm. The complete, self-powered system is provided in II.8. A laboratory prototype of the current sensor module showed excellent linearity when placed in the immediate vicinity of a power cord and the reported sensitivities were of the order of 1 mV/A.<sup>[22]</sup> A similar solution for 3D MEMS magnetometers was developed at CEA-Leti in Grenoble and uses magnetic material which is integrated into the MEMS device and which experiences a torque when surrounded by a magnetic field. Signal detection is based on piezoresistive detection using gauges of mono-crystalline silicon with nanometric section.<sup>[28]</sup>

While providing a very interesting and promising research domain, it must be concluded that MEMS solutions for magnetic field sensing (let alone current sensing with a given geometrical selectivity) do not yet present an applicable solution when it comes to the task at hand. In particular, since the work presented in the following chapters aims to demonstrate the effectiveness of the proposed measurement principle for current determination, only commercially available field sensing solutions that meet the requirements of the approach can be considered here. Nevertheless, the independence of the measurement principle and technology, and the resulting adaptability of the measurement method, calls for a consideration of all current and future developments in the field of magnetic field sensing, amongst which MEMS technology assumes a prominent role.

### II.4.2 Induction sensors

Induction coils, as used for the Rogowski coil current sensor, can also be employed for other applications involving magnetic field measurements (e.g. study of the earth's magnetic field, audio frequency applications or magnetic recording<sup>[30]</sup>) but have previously required rather large coil dimensions to achieve sufficient sensitivity. Air coils in particular are of interest because of their

stable and linear response to the field, however, their miniaturisation was for a long time hindered by the insufficient sensitivity which required for the inclusion of a ferromagnetic cores. Recent advancements in coil design allow for a reduction of the coil size and consequently the determination of the magnetic field over a reduced volume, thus enabling the application of these coils for the spatial mapping task at hand. Since no commercial product is readily available for air coils of the desired dimensions (< few cm), they could not be considered for the prototype development detailed below. However, the state of research calls for their consideration as a sensor technology for advanced prototypes. Their application is, furthermore, especially promising for power grid applications, since they allow direct determination of the field component at a defined frequency, i.e. 50 Hz, and thus the elimination of undesired perturbations.

The general operation principle of induction sensors is given by Faraday's law<sup>[29,30,31]</sup>:

$$V_i = \frac{d\Phi}{dt} = \frac{d[NA(t)\mu_0\mu_r(t)H(t)]}{dt} \quad (\text{II.13})$$

with the magnetic flux  $\Phi = BA$ , the magnetic field  $H$  and the sensor core relative permeability  $\mu_r$  ( $\approx 1$  for air) and for a coil of  $N$  turns and a cross-sectional area  $A$ .

The equation can be rewritten to account for the temporal variation of the different parameters, each associated with respective applications:

$$V_i = N\mu_0 \left[ \underbrace{A\mu_r \frac{dH(t)}{dt}}_{\text{search coil term}} + \underbrace{H\mu_r \frac{dA(t)}{dt}}_{\text{rotating coil term}} + \underbrace{HA \frac{d\mu_r(t)}{dt}}_{\text{fluxgate term}} \right] \quad (\text{II.14})$$

Air coils offer the advantage that they do not contain a nonlinear magnetic material and thus provide linear and stable output. These will be studied in more detail in the following section.

### Air coils

Several parameters must be considered in the design of an air coil. The primary requirement is a sufficient sensitivity of the coil. As evident from the above equations, this can be obtained by increasing the number of turns in the coil or the cross-sectional area. Multi-turn coils, however, suffer from parasitic capacitances that can lead to resonances at low frequencies, an effect that can also be temperature-sensitive. The use of a voltage-to-current converter is thus meaningful for the suppression of the parasitic capacitance.

The resolution of air coil sensors is limited by thermal noise, which is inversely proportional to the square of the coil diameter and the frequency. An example of the noise spectrum is provided in Fig. II.9, right. The left hand-side of the figure also provides a typical frequency response of the air coil sensors. To obtain high sensitivities, it is thus necessary to increase the coil diameter  $d$ , and previous solutions, employed e.g. for the measurement of micropulsations of the EMF, often involved dimensions on the meter scale (with the associated heavy weight). For smaller sensors, the reduced sensitivity limited the application scope to tasks such as position or movement detection or eddy-current detection.

Recent advancements open the possibility for an application of air coil sensors for magnetic field measurements that can be considered punctiform for the measurement method at hand, amongst these:

- A miniature search coil magnetometer optimized for operation between 20 mHz and 2 kHz. Dimensions:  $l = 5.4$  cm x  $d = 3$  cm, using  $N = 160000$  turns of a  $50$   $\mu$ m copper wire. The noise is characterized as  $14$  pT/ $\sqrt{\text{Hz}}$  at 1 Hz and  $0.35$  pT/ $\sqrt{\text{Hz}}$  between 100 Hz to 2 kHz (see Fig. II.9).<sup>[32]</sup>
- Design of a miniature search coil magnetometer with integrated electronics and batteries. A coil of  $d = 5$  mm times  $l = 50$  mm allows for the integration of a battery that provides continuous operation of half a year, with a noise of  $14.3$  pT/ $\sqrt{\text{Hz}}$  at 1 Hz.<sup>[33]</sup>
- A miniature three-axial search coil magnetometer providing  $12$  pT/ $\sqrt{\text{Hz}}$  at 1 Hz with dimensions of  $7.2 \times 6.9 \times 6.9$  cm, including the necessary electronics.<sup>[34]</sup>
- Optimization of a search coil magnetometer for space experiments, achieving down to  $15$  fT/ $\sqrt{\text{Hz}}$  at a few kHz. Dimensions  $d = 10.8$  mm,  $N = 13110$ .<sup>[35]</sup>

Given these recent advancements, it can be expected that miniature air coil sensors will be (commercially) available in the near future (or should be considered for further development/adaptation within the framework with respect to this application) and should consequently be taken into consideration for advanced prototypes. Together with MEMS technologies, they therefore complete the outlook for the magnetometer technologies that are of interest for further development of the measurement method and application beyond the framework of this thesis. As explained above, both solutions would simply require a substitution of the sensor technology, while the measurement principle would be left untouched. Their integration would thus be straightforward and would be relevant if it can serve to reduce sensor noise (and consequently the precision of the

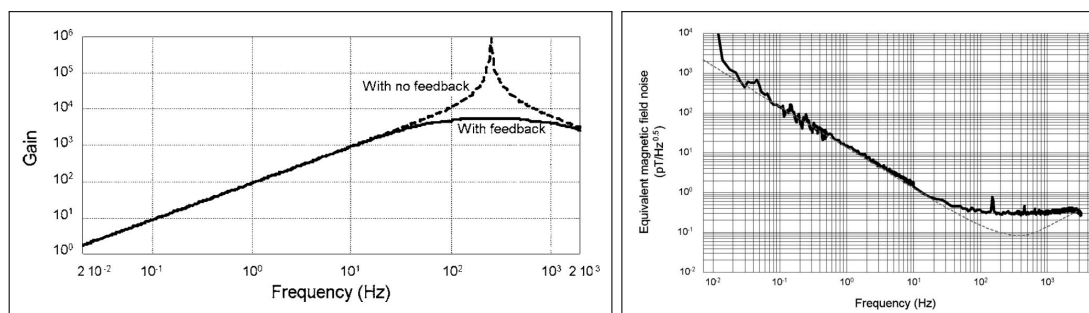


**Figure II.9:** Frequency response (left) and equivalent magnetic noise spectrum (right) for search coils.<sup>[32]</sup>

measurement method) or price, or if it significantly facilitates the design and fabrication of the sensor array.

## II.5 Conclusion

The outlook on MEMS and air coil sensor technology completes the overview of the state-of-the-art technologies. It should, however, not remove the focus from the central point of this chapter. As explained above, the sensor technology has been presented with the application in mind and the same mindset applies to the conclusions that can be drawn from the provided information. Given the measurement conditions in an electrical grid it is only meaningful to consider contactless (AC) measurement methods. Consequently, the measurement method must provide a geometrical selectivity between magnetic field sources (primarily the other two conductors). The solutions that meet these requirements have been classified either as dedicated current sensors (Rogowski coils or current transformers) or a combination of magnetic field sensors and an adequate measurement principle/sensing configuration. All of the commercially available solutions, summarized in Tables II.2 and II.3 have one thing in common: they require magnetic field measurement along a path that surrounds the conductor of interest and the sensors must thus be positioned accordingly. This complicates the installation of these current sensors. There is thus a strong interest in the development of an innovative current sensor which can be located besides a conductor, either in immediate proximity or at a small distance, while providing a comparable level of geometrical selectivity. Such a current sensor would significantly increase the application and installation possibilities for current measurements in electrical grids. The work presented in the following chapters seeks to fill this void by developing a sensing solution that relies on the theoretical framework of spatial harmonics and which uses an array of sensors (selected among existing magnetic

## *II.5. Conclusion*

---

sensor technologies) for current determination. It thus belongs to the group illustrated on Fig. II.1, right, i.e. those current measurement methods that are based on a combination of measurement principle and sensor technology. The inherent independence of the measurement principle and the sensor technology for the current determination method described in this thesis, ensures the flexibility of the method when it comes to an adaptation to future developments. The overview of magnetic sensor technologies provided above can thus serve as a selection guide for a specific application task. It was in fact already used as such during the work on this thesis, since the test of the measurement principle under laboratory conditions had very specific requirements that will be discussed in Ch. 4. In the future it can be used in the same way to determine a suitable sensor technology for industrial applications. In a more distant future, the proposed measurement method may also benefit from new developments, e.g. in the field of MEMS, to further enhance the attainable precision. The following chapter will serve to introduce the theoretical framework of the measurement principle, before the dimensioning considerations that result from it is used to select a suitable sensor technology for laboratory measurements amongst those provided above. The sensing characteristics will, therefore, also play a pivotal role in the assessment of the measurement results provided in Ch. 5.

---

## Spatial harmonics decomposition

---

---

III.1	Introduction to spatial harmonics . . . . .	41
III.2	2D magnetic field decomposition in spatial harmonics . . . . .	43
III.2.1	Coefficient identification/inverse problem . . . . .	54
III.2.2	Parametric analysis: dimensioning and error sources . . . . .	55
III.3	Calibration procedure (2D case) . . . . .	68
III.3.1	Calibration of transfer factor - general considerations . . . . .	68
III.4	3D spherical harmonics decomposition . . . . .	72
III.4.1	Linear and non-linear conductors . . . . .	76
III.4.2	Sensor distribution . . . . .	78
III.4.3	Parametric analysis - dimensioning and error sources . . . . .	82
III.5	AC measurement methods . . . . .	91
III.5.1	Pointwise evaluation . . . . .	91
III.5.2	Fast Fourier Transform of field measurements . . . . .	92
III.6	Conclusion . . . . .	92

---

### III.1 Introduction to spatial harmonics

As explained in the previous chapter, the main requirement for current measurements in multi-source environments is a geometrical selectivity between the source of interest and perturbing

sources. Existing measurement principles do not achieve this or suffer from the complications/limitations discussed above. In order to fill this void and meet the requirements, a new measurement principle based on the decomposition of the magnetic field into spatial harmonics has been developed. As will become evident below, this can, in a very broad sense, be considered an extension of gradient field measurements, since both principles rely on the investigation of the spatial distribution and orientation of the magnetic field. Spatial harmonics provide more detailed information about the field and are consequently more potent when it comes to the differentiation of field sources. In the past, spatial harmonic decompositions of the magnetic field have been studied extensively at G2ELab. They have been applied primarily for the identification and characterisation of electromagnetic sources and a detailed discussion is provided in the thesis of L. Schmerber<sup>[36]</sup>. The general idea is to describe the magnetic field using a set of suitable periodic (spatially-dependent) functions of different orders. This decomposition is analogous to a Fourier series, which is commonly used, e.g. in signal processing, to decompose a function of time into periodic functions of different frequencies. The main difference for the spatial harmonic decomposition (SHD) of the magnetic field is that the periodic functions exhibit a spatial dependency, but they are similarly summed up to reconstruct the original function (field). Before discussing the relevant formulations and their implications, it is meaningful to examine the two distinct application scenarios of the SHD for the magnetic field of current-carrying conductors, to establish a framework for the considerations and the course of this chapter:

- Two-dimensional magnetic field: a particular case, which is only applicable under the proviso that the field is created by an infinite straight conductor (II.4). In this case, the magnetic field component parallel to the current flow is equal to zero. To which extent actual conditions can differ from those required for this assumption (e.g. deviation from straight conductor path), before it becomes insufficiently accurate, depends on the specific application case. For example, aerial cables for power transmission will meet this requirement between two utility poles but deviate from it at intermediate/end support or connection points.
- Three-dimensional magnetic field: the universally valid spatial description of the field.

In Ch.II, several measurement methods which only require the detection of a 2D field (in a near-linear portion of a conductor path) have been discussed and a large variety of commercial products and patents rely on these. The possibility for this differentiation is thus intrinsic to applications of current measurement for conductors and can generally not be exploited in other fields of magnetic field characterisation. The measurement principle described below should suit both conductor geometry categories, i.e. those with a (predominately) two-dimensional field (straight

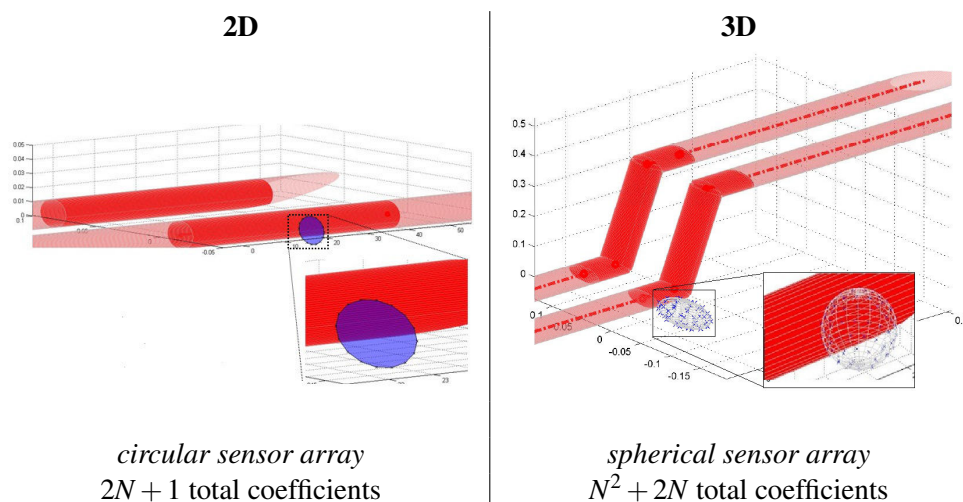


**Figure III.1:** Left: Conductor geometry of an (infinite) straight wire that creates a 2D magnetic field. Right: Exemplary conductor geometry creating an essentially 3D magnetic field. Both figures also indicate the adapted sensing geometry/area for the respective cases (in blue). Their design and implementation will be discussed later on in this chapter.

conductors, e.g. aerial cables) and those with an inherent three-dimensional field distribution (non-linear conductor paths, e.g. power couplers). An illustration of the two scenarios is provided in Fig. III.1, which also already indicates that each case will dictate an adapted measurement geometry for the magnetic field sensing technology. The two cases and the respective formulations will be discussed below in order of increasing complexity. Therein, the presentation of the decomposition of a 2D magnetic field in 2D spatial harmonics will contain greater detail and background on the measurement principle of a SHD itself, which will subsequently only need to be transferred and extended to 3D fields, in order to obtain the resulting implications for the measurement process. This procedure will highlight the difference in complexity between the two application cases.

### III.2 2D magnetic field decomposition in spatial harmonics

As briefly introduced above, the aim of this section is to present the decomposition of a two-dimensional magnetic field in spatial harmonics as well as the advantages that it provides for current determination. Suitable periodic functions for the decomposition of the magnetic field

### III.2. 2D magnetic field decomposition in spatial harmonics

---

should satisfy Laplace's equation in polar coordinates<sup>[37]</sup>:

$$\Delta\Psi(r, \vartheta) = \frac{1}{r} \frac{\partial}{\partial r} \left( r \frac{\partial\Psi(r, \vartheta)}{\partial r} \right) + \frac{1}{r^2} \frac{\partial^2\Psi(r, \vartheta)}{\partial\vartheta^2} = 0 \quad (\text{III.1})$$

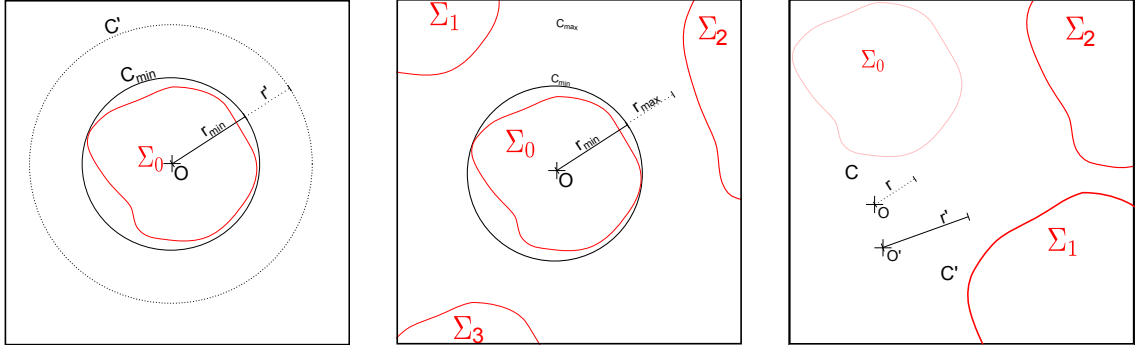
A consistent (periodic) solution requires that  $g(\vartheta + 2\pi) = g(\vartheta)$ , so that  $n$  can only assume integer values ( $n \in \mathbb{N}^+$ ). The full, separated solution then gives<sup>[36]</sup>:

$$\Psi(r, \vartheta) = (A_0 \ln r + B_0) + \sum_{n=1}^{\infty} (A_n r^n + B_n r^{-n}) (C_n \cos(n\vartheta) + D_n \sin(n\vartheta)) \quad (\text{III.2})$$

with development coefficients  $A_0, B_0, A_n, B_n, C_n$  and  $D_n$  that only depend on the field source(s). With this result it is already possible to make the differentiation between two different applications of a SHD for the magnetic field:

- **external decomposition:** the field is studied for an (infinite) zone that encompasses all of the field source, so that only functions proportional to  $1/r^n$  (decreasing magnitude) can be employed to describe the field
- **internal decomposition:** the field is studied for a finite zone which is source-free, i.e. surrounded by the sources being investigated, thus, only functions proportional to  $r^n$  (increasing magnitude towards the source(s)) can be employed to describe the field

The external decomposition presents an approach similar to the gradient field measurements discussed in the previous chapter and is also the approach selected for the characterization of magnetic field sources<sup>[38]</sup>. Schematic of the relevant regions for different applications of the spatial harmonics decomposition are provided in Fig. III.2. For the external decomposition (left-hand side of the figure), the source(s) are included in the region  $\Sigma_0$  and can be characterized using magnetic field measurements from sensors placed on any circle that at least encompasses the source region ( $r_i \geq r_{\min}$ ). The region  $C_0$  which extends to infinity is also the zone of validity for the reconstruction of the field based on the decomposition coefficients. The origin of the decomposition corresponds to that of the circle and possibly that of the source. The configuration for an internal decomposition is provided on the right-hand side of Fig. III.2, in which all source regions  $\Sigma_i$  are disjoint from the sensor region  $C_0$ . The latter is defined by the placement of the sensors on a circle of radius  $r_c$ , which must be source-free. This is the only constraint for the position and radius of the circle. The center of decomposition is again the center of the circle and will thus change depending on the position of the circle. In this case, the reconstruction is valid within this region  $C_0$ . It is also possible to use a combination of the internal and external decomposition



**(a) External decomposition:** all sources are included in the region  $\Sigma_0$  and sensors can be placed on circles  $C_i$ , with  $r_i \geq r_{\min}$ . The circle of radius  $r_{\min}$  presents the smallest possible placement around the source. The decomposition is valid outside of  $C$  to infinity.

**(b) Combined decomposition:** combination of external decomposition for source(s) of interest in  $\Sigma_0$  and internal decomposition for perturbing sources in  $\Sigma_{1,2,\dots}$ . Sensors can be placed on circles  $C_i$ , with  $r_{\min} \leq r_i \leq r_{\max}$  and the reconstruction is valid between  $r_i$  and  $r_{\max}$ .

**(c) Internal decomposition:** with disjoint regions ( $C \cap \Sigma_i = \emptyset$ ). Sensors can be placed on circles  $C_i$  as long as the enclosed area is source-free. This corresponds to the region of validity for the field reconstruction.

**Figure III.2:** Different application methods of spherical harmonic decompositions using either an internal or an external composition or a combination of both.

to describe the field created by multiple sources. This approach has previously been applied to current measurements<sup>[14,15,16]</sup> and the definition of regions is provided in Fig. III.2(b). In this case the sensors can be placed in a region  $C_0$  that is intermediate to the region  $\Sigma_0$  containing the source (conductor) of interest and the regions  $\Sigma_i$  containing perturbing sources (conductors). It is then possible, to utilize an external (2D) decomposition for the sources in  $\Sigma_0$ , while the perturbing sources can be modelled using an internal decomposition using functions increasing in  $r$  ( $\propto r^n$ , Eq. III.2). For a conductor as field source in  $\Sigma_0$  and a circular sensor array in  $C_0$ , it is furthermore, possible to write the magnetic scalar potential in a form with only an angular dependency  $\left[ \Psi(\vartheta) = \frac{I_0 \vartheta}{2\pi} \right]$ .<sup>[14]</sup> This combination of internal and external decompositions for the conductor of interest and the perturbing conductor(s), respectively, results in a formulation for specific coefficients that return the desired current value from (few) magnetic field measurements, e.g. it was possible to effectively reject the influence of the perturbing conductor using four magnetoresistive field sensors, placed on a circular path of radius  $r = 3$  cm, centred around the source, and a summing of sensor inputs to approximate Ampère's circuital law (for DC currents  $I_0 = -I_1 = 8$  A, perturbing conductor as close as 6 cm to the primary conductor)<sup>[14]</sup>. In this case, the formulations and the reconstruction of the field are valid within the region  $C_{\min} \leq C' \leq C_{\max}$ . The formulations are based on the assumption that the conductor is positioned at the center of decomposition (i.e.

the center of the circular sensor array). Other studies of the use of an external decomposition for current determination, have indicated that, if the conductor is decentred, additional terms are added to the magnetic scalar potential. In consequence, the magnetic field is a combination of the contribution of a centred conductor and a component that depends on the eccentricity of the conductor, thus adding harmonic terms and potentially increasing the number of required sensors.<sup>[39,36]</sup> Amongst the three cases presented above, the use of an external decomposition or a combination of the external and internal decomposition (Fig. III.2(a) and (b)) both require placement of the sensors in a region that encompasses the source (although the sensors must not necessarily encompass the source completely<sup>[40]</sup>). In contrast, the use of an internal decomposition (Fig. III.2(c)) allows for the placement of the sensors in a restricted volume besides the source (conductor) of interest. Since the reconstruction of the magnetic field is valid within the same volume, it can describe the field of an arbitrary number of sources in regions  $\Sigma_i$ , as long as the region  $C_0$  is source-free. This creates a potential for a (further) miniaturization of magnetic field sensor arrays used for current measurements and for their facilitated installation. Both aspects can serve to increase the applicability of the measurement method. An approach based on the internal decomposition of the magnetic field in spatial harmonics will therefore be studied in detail below.

As stated above, the magnetic vector potential or, more generally, a function  $\mathcal{X}(r, \vartheta)$  for which  $\Delta\mathcal{X}(r, \vartheta) = 0$  can thus be developed according to Eq. III.2. For the 2D case, the magnetic vector potential  $\vec{A}(r, \vartheta)$  presents an appropriate choice, since it only has one non-zero component and allows for a direct derivation of the magnetic flux density. For the internal decomposition, it can be written as (Eq. III.2)<sup>[36]</sup>:

$$\vec{A}(r, \vartheta) = A_z(r, \vartheta)\vec{e}_z = \left[ (A_0 \ln r_0 + B_0) + \sum_{n=1}^{\infty} r^n (a_n \cos(n\vartheta) + b_n \sin(n\vartheta)) \right] \vec{e}_z \quad (\text{III.3})$$

with  $a_n = A_n \cdot C_n$  and  $b_n = A_n \cdot D_n$

with  $r, \vartheta$ , the polar coordinates of a point inside the finite zone that contains the decomposition center,  $n$  the decomposition order and  $a_n$  and  $b_n$  the decomposition coefficients which depend on the conductor positions and current magnitudes. In practical applications, the decomposition can be limited to a maximum decomposition order  $N$  (depending on the radius of the finite zone and its distance to the sources) and therefore uses only  $2N$  coefficients. In Eq. III.4, the terms  $A_0 \ln r_0$  and  $B_0$  correspond to constant contributions to the magnetic field, e.g. a static and spatially homogeneous magnetic field such as the geomagnetic field. In practical applications, this contribution, and the corresponding coefficients, can often be disregarded by means of differential measure-

ments (as was the case for this work, see Ch. V) and the equation can be simplified accordingly. The resulting magnetic flux density for the internal decomposition is thus:

$$\vec{B} = \nabla \times \vec{A} \quad (\text{III.4})$$

$$B_r(r, \vartheta) = \frac{\mu_0}{2\pi} \sum_{n=1}^N n \cdot r^{n-1} [-a_n \cdot \sin(n\vartheta) + b_n \cdot \cos(n\vartheta)] \quad (\text{III.5})$$

$$B_\vartheta(r, \vartheta) = \frac{\mu_0}{2\pi} \sum_{n=1}^N n \cdot r^{n-1} [a_n \cdot \cos(n\vartheta) + b_n \cdot \sin(n\vartheta)] \quad (\text{III.6})$$

The above formulations now allow for the reconstruction of the magnetic field within an area that is source-free and which is accordingly positioned besides a conductor of interest. A combination of sensor measurements can be employed to determine the respective terms of the decomposition orders, in order to reconstruct the source parameters (source current flow for known source position or vice versa). The form of the decomposition depends on the location of the magnetic

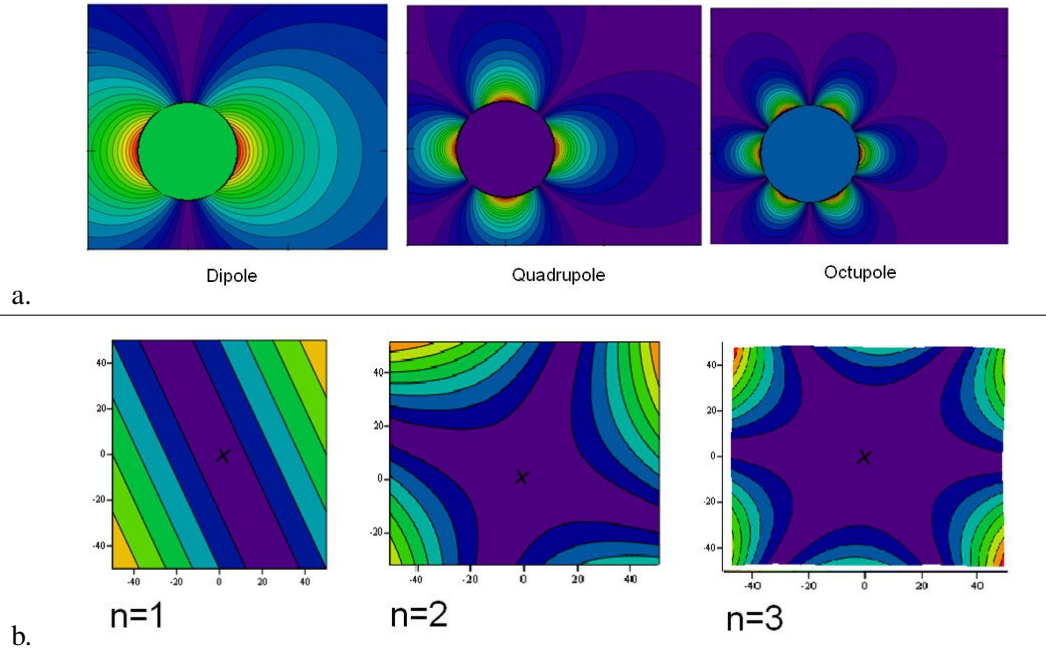


**Figure III.3:** Contour plots of magnetic vector potential for dipole, quadrupole and octupole sources as used for, a. external spatial harmonics decomposition (terms decreasing in magnitude with  $r^n$ ); b. corresponding terms for the internal decomposition, with a decomposition center marked by the cross and field sources outside the decomposition volume (terms increasing in magnitude with  $r^n$ ).

### III.2. 2D magnetic field decomposition in spatial harmonics

---

field sources with respect to the region of decomposition. If the sensors, and thus the region of decomposition, encompass the source(s) the decomposition is referred to as an external decomposition. A two-dimensional decomposition is adequate for the decomposition of a field from infinite straight conductors, as these do not create a field component parallel to the conductor path. The 2D decomposition uses sums of sine and cosine functions ( $\cos(n\vartheta)$ ,  $\sin(n\vartheta)$ ). Before the theoretical formulations are developed below, the following considerations will provide a first overview of the decomposition concept. A decomposition of the magnetic field in spatial harmonic functions, allows a reconstruction of the magnetic field within a defined area or volume. For this, the field is decomposed into a first order term  $B_1$  that corresponds to the equivalent dipole component of the source and a second order term  $B_2$ , the quadrupole component, which, together with subsequent higher order components, presents a full description of the field. To visualize this concept, the first three orders for the reconstruction of the (2D) field of a current-carrying conductor are shown in Fig. III.3a. To describe the actual field of the conductor, it is sufficient to limit the sum of decomposition terms to include orders up to a specific order. The maximum order depends on the exact

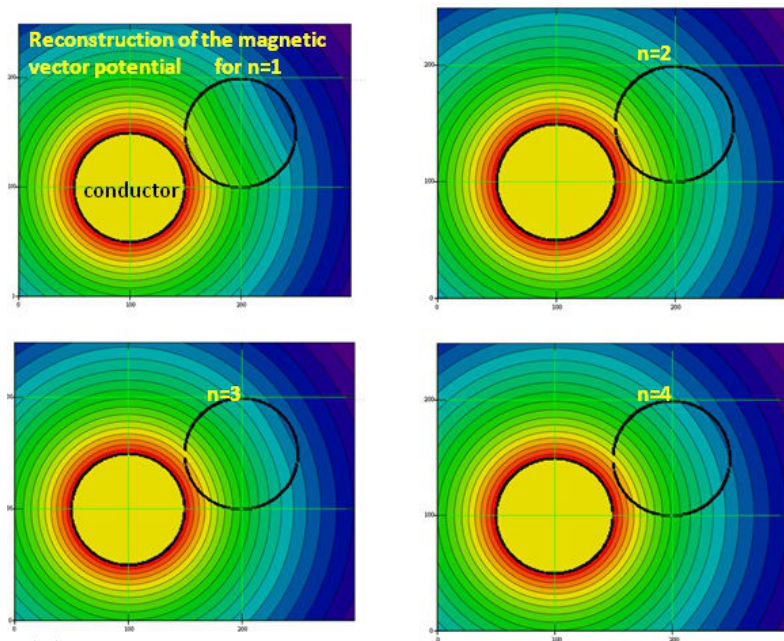


**Figure III.4:** Illustration of the reconstruction for the magnetic vector potential using an increasing number of orders (from  $N = 1$  to 4). For the field of an infinite straight conductor. The circle besides the conductor marks the decomposition area where the field is reconstructed using the calculated coefficients.

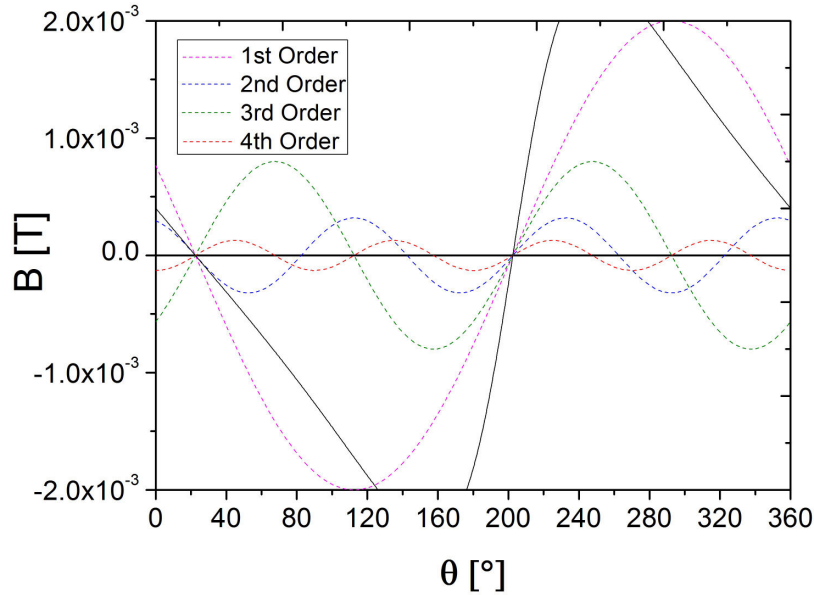


**Figure III.5:** Contribution of each order (dotted lines) to total magnetic flux density (solid line) along circular sensor array path in 2D for  $d_0 = 6$  cm,  $r = 4$  cm and  $I_0 = 10$  A.

parameters of the decomposition which will be investigated below. A graphical representation of how an increasing number of orders results in an improved approximation of the true field is provided in Fig. III.4, where the magnetic vector potential is reconstructed.

Given the general formulations for the reconstruction of the magnetic field, it is now possible to with the analysis of a representative geometry for current measurements. An exemplary geometry for the measurement problem for a 2D magnetic field (straight conductor piercing the plane) is provided in Fig. III.6. For such a geometry, the contributions of the specific orders to the total field along the circle are provided, for a given array radius and position, in Fig. III.5. Due to the factor  $r^{n-1}$  in equations III.4-III.6 the magnitude decreases for higher orders. Before this behaviour is discussed in more detail below, including the resulting considerations for the dimensioning of the array, the theoretical framework of the 2D decomposition problem will be completed by a study of the development coefficients and their identification.

The following geometrical considerations allow the derivation of an analytical formula for the decomposition coefficients  $a_n, b_n$ <sup>[41]</sup>. For this it is initially sufficient to consider a single conductor (since the superposition principle applies for magnetic fields, multi-conductor solutions can be

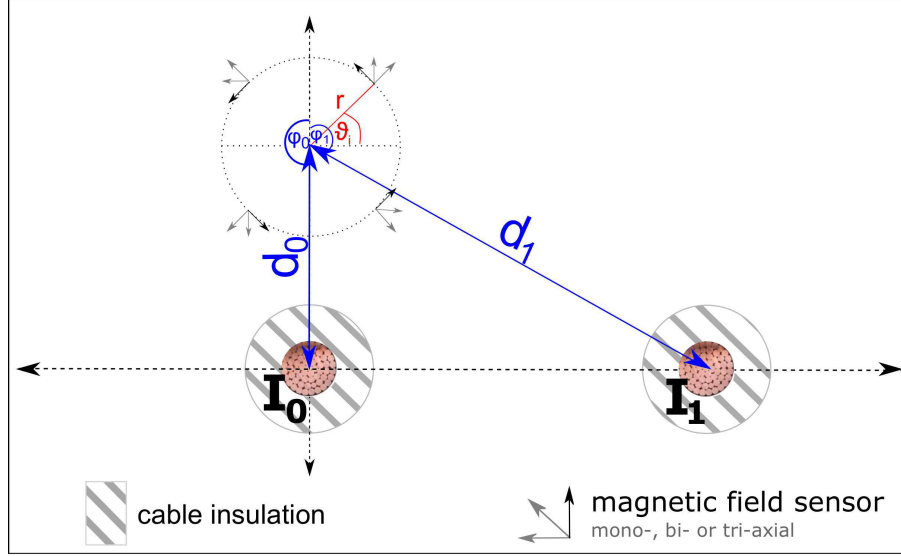


**Figure III.6:** Geometrical description of exemplary measurement conditions for an internal spatial harmonic decomposition and field reconstruction within a circle delineated by individual sensors. The figure shows two conductors/field sources at  $d_0, \varphi_0$  and  $d_1, \varphi_1$ .

obtained by addition). Eq.II.4 is then applicable for the description of the magnetic flux density for this geometry and can also be formulated in terms of the magnetic vector potential, which only has a component in the direction of  $\vec{e}_z$  for a magnetic field in the  $x$ - $y$ / $r$ - $\vartheta$ -plane:

$$\vec{A}(d') = A_z \vec{e}_z = -\frac{\mu_0 I_0}{2\pi} \ln(d') \vec{e}_z \quad (\text{III.7})$$

for a conductor  $I_0$  at a given distance  $d'$ . The center of the decomposition is the center of the circle in Fig. III.6 and the measurement points are ideally placed along the circumference (single- or multi-axis measurements are possible, see description of practical implementation in Ch. V). Using the relative position of the (center of the) conductor/source with respect to the center of decomposition,  $d_0, \varphi_0$ , and the relative position of a measurement point/sensor position  $r, \vartheta$  (with the origin of the coordinate system at the center of decomposition) in combination with the law of cosines yields:

$$d'^2 = r^2 + d_0^2 - 2rd_0 \cos(\vartheta - \varphi_0) \quad (\text{III.8})$$

For the internal decomposition  $r < d_0$ , this equation can be rewritten as:

$$d'^2 = d_0^2 \left( 1 + \left( \frac{r}{d_0} \right)^2 - 2 \frac{r}{d_0} \cos(\vartheta - \varphi_0) \right) \quad (\text{III.9})$$

and inserted into Eq.III.7 to yield:

$$A_z(r, \vartheta) = -\frac{\mu_0 I_0}{2\pi} \left[ \ln(d_0) + \frac{1}{2} \ln \left( 1 + \left( \frac{r}{d_0} \right)^2 - 2 \frac{r}{d_0} \cos(\vartheta - \varphi_0) \right) \right] \quad (\text{III.10})$$

At this point, it is possible to take advantage of the fact that the vector potential is periodic with respect to  $\vartheta$  and can thus be written as a sum of sine and cosine functions. Specifically, the second term of Eq. III.10 can be decomposed into Chebyshev polynomials that converge for  $\frac{r}{d_0} < 1$ <sup>[41]</sup>. This results in the following form for the vector potential:

$$A_z(r, \vartheta) = \frac{\mu_0 I_i}{2\pi} \left[ \ln(d_0) + \sum_{n=1}^{\infty} \frac{\cos(n(\vartheta - \varphi_0))}{nd_0^n} r^n \right] \quad (\text{III.11})$$

A decomposition of the cosine and a comparison with Eqs. III.5 and III.6 allows an identification of the coefficients:

$$a_n = \frac{\cos(n\varphi_0)}{nd_0^n} I_0 = k_{a_n} \cdot I_0 \quad (\text{III.12})$$

$$b_n = \frac{\sin(n\varphi_0)}{nd_0^n} I_0 = k_{b_n} \cdot I_0 \quad (\text{III.13})$$

for a distance  $d_0$  and angle  $\varphi_0$  between the conductor and the center of decomposition and a relative field sensing position  $r, \vartheta$ . For a given (e.g. manufactured) array geometry and sensor position, the parameters  $(r, \vartheta_i)$  are constant, since the center of decomposition is also the center of a manufactured sensor support. For the 2D SHD there is thus a linear relationship between the decomposition coefficients  $a_n, b_n$  and the current of interest  $I_i$ , and the transfer functions  $k_{a_n, b_n}$  depend on the position of the decomposition area relative to the source. If the transfer function, i.e. the measurement position, is known, the current  $I_i$  can be deduced directly from the decomposition coefficients. For a system of multiple conductors, the superposition principle for magnetic fields would likewise result in contributions from each individual conductor to the coefficient values:

$$a_n = \sum_{i=0}^{N_C} \frac{I_i}{nd_i^n} \cos(n\varphi_i) = \frac{I_0}{nd_0^n} \cos(n\varphi_0) + \frac{I_1}{nd_1^n} \cos(n\varphi_1) + \dots \quad (\text{III.14})$$

### III.2. 2D magnetic field decomposition in spatial harmonics

---

and the resulting ratio of contributions from two currents  $I_0$  and  $I_1$  becomes

$$\begin{aligned} \frac{a_n(I_0)}{a_n(I_1)} &= \frac{I_0 \cos(n\varphi_0) d_1^n}{I_1 \cos(n\varphi_1) d_0^n} & \text{for } I_0 &\approx I_1 \longrightarrow & \frac{a_n(I_0)}{a_n(I_1)} &\propto \frac{d_1^n}{d_0^n} \\ & & \text{for } d_1 &= f \cdot d_0 \longrightarrow & a_n(I_0) &\propto f^n \cdot a_n(I_1) \end{aligned} \quad (\text{III.15})$$

The following conclusions can thus be drawn for the geometrical selectivity of the method:

- for differentiation between conductors the requirement for the placement of the center of decomposition is  $d_1 \gg d_0$
- geometrical selectivity can be enhanced by increasing
  - the scale factor  $f$  or
  - the evaluated order  $n$ , since  $a_n(I_0) \propto f^n \cdot a_n(I_1)$

It must, however, be noted, that the scale factor and evaluation order cannot be increased at will since the location of the radius (along with the radius  $r$  of the decomposition area/volume) also influences the magnitude/contribution of each order. The measurement conditions must therefore allow for, and be adapted to, a decomposition of the magnetic field to a sufficiently high order for the required geometrical selectivity, while ensuring that these orders of interest remain measurable, i.e. that the contribution is not lost e.g. in magnetic sensor noise. To assess this latter requirement, it is purposeful to consider the relative magnitudes of decomposition orders and their dependence on the array-to-source distance  $d_i$  and the array radius  $r$ , which can be obtained from Eq.III.11:

$$\frac{B_{n+1}}{B_n} \propto \frac{r}{d_i} \quad (\text{III.16})$$

As the contribution of the respective orders decreases with the distance to each conductor/magnetic field source, the influence of each source is diminished by a factor of  $1/d_i$  with each order. As long as the geometry at the installation site allows for a placement of the sensor array (for the determination of the decomposition coefficients) closer to the conductor under investigation than to the perturbing conductors ( $d_0 < d_i$ ), the influence of those conductors will be negligible as of a defined order. With the formulations derived above, it is possible to perform simulations as a proof of concept for the application of the measurement principle. As a reminder, the objective is to determine the current in a nearby conductor of interest ( $d_0 = 6$  cm) with a precision of  $\Delta I_0 < 0.5\%$ . The geometrical selectivity that a 2D spatial harmonic decomposition can attain can be determined by studying the effect of a perturbing conductor at a given lateral distance (e.g.,

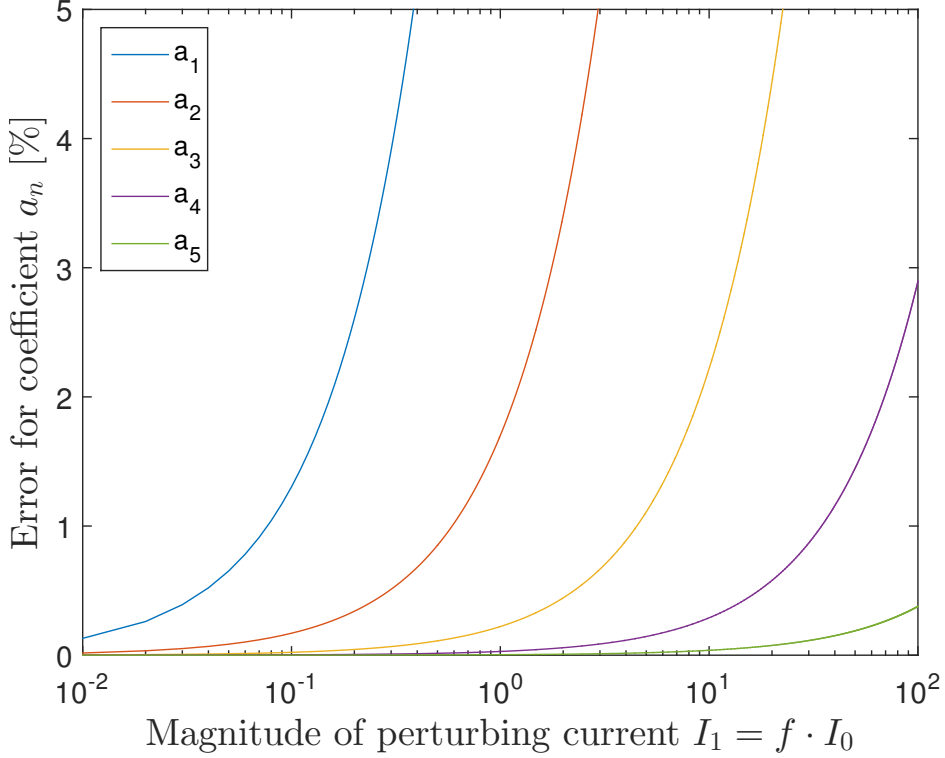


**Figure III.7:** Influence of increasingly large perturbing current on the decomposition coefficients of the first five orders. The dependence demonstrates the enhanced geometrical selectivity for higher orders. Simulation parameters: 100 sensors along circular sensor array path in 2D for  $d_0 = 6$  cm,  $\varphi_0 = 180^\circ$ ,  $r = 3.2$  cm,  $I_0 = 10$  A and  $I_1 = f \cdot I_0$  at  $d_1 = 6 + 40 = 46$  cm; maximum decomposition order  $N = 10$ .

$d_1 = 6 + 40 = 46$  cm). A first simulation result, with a typical measurement configuration (for details on the simulation software and geometrical parameters, section III.2.2) is thus presented in Fig. III.7, which also provides a first indication of the order which is required to achieve a sufficiently distinct geometrical selectivity between field/sources conductors. The simulation indicates that, for a typical conductor geometry, a precision of  $\Delta I_0 \leq 0.5\%$  can be obtained as of the fourth or fifth order of decomposition even if the perturbing current is 10 to 100 times stronger than the current of interest. The required decomposition order dictates the number of sensors that must be installed (number of measurements  $N_M > 2N$ ). However, to ensure that all orders contribute a distinguishable signature to the measured results the sensor array must have a minimum size. These dimensioning effects are studied in the following section. To study the notion of higher order magnitudes and contributions, as well as the measurement principle in general, in more detail, it is initially necessary to complete the toolbox for the 2D SHD by defining the procedure for the

determination of the decomposition coefficients  $a_n, b_n$ .

### III.2.1 Coefficient identification/inverse problem

Eqs.III.5-III.6 states that the magnetic flux density for a 2D field can be expressed as a product of a radial function ( $r^{n-1}$ ), angular functions ( $\cos(n\vartheta)$  or  $\sin(n\vartheta)$ ), and decomposition coefficients ( $a_n, b_n$ ). The first two functions describe the geometrical configuration of the measurement system and depend only on the definition of a decomposition area (specifically by the placement of sensors along its boundary).

$$\mathbb{A}\vec{x} = \vec{B} \quad (\text{III.17})$$

$$\mathbb{A}(r, \vartheta_i)\vec{x} = \vec{B}(r, \vartheta_i) \quad (\text{III.18})$$

with the matrix  $\mathbb{A}(r, \vartheta_i)$  (a uniform radius can be assumed for now) of dimensions  $(j,k)$  that defines the measurement geometry (positions  $[r_i, \vartheta_i]$  of the individual sensors) for  $j$  measurements and  $k = 2N$  coefficients and for a development up to the order  $N$ . Accordingly,  $\vec{x} = [a_1, b_1, \dots, a_N, b_N]$  is the vector of  $2N$  coefficients and  $\vec{B} = [|\vec{B}_r^1|, |\vec{B}_\vartheta^1|, \dots, |\vec{B}_r^{N_S}|, |\vec{B}_\vartheta^{N_S}|]$  is the vector that contains the  $j$  magnetic flux measurements. Therefore, if  $k > j$ , i.e. if there are more coefficients used for the decomposition than measurements made, the inverse problem is under-determined. If  $k = j$ , it is well-defined, and it is over-determined if there are more measured values than development coefficients, i.e. if  $k < j$ . The choice/requirement of the desired maximum decomposition order  $N$  thus dictates the number of required measurements ( $j$ ) and hence the number of mono- or bi-axial sensors ( $N_S$ ). Based on the formulation of the inverse problem (Eqs. III.5-III.6) and for a set of  $N_S$  bi-axial sensors, the matrix  $\mathbb{A}$  assumes the following form:

$$\mathbb{A}(r_i, \vartheta_i) = \frac{\mu_0}{2\pi} \overbrace{\begin{pmatrix} -\sin(\vartheta_1) & \cos(\vartheta_1) & \dots & \dots & -N \cdot r^{N-1} \sin(N\vartheta_1) & N \cdot r^{N-1} \cos(N\vartheta_1) \\ -\cos(\vartheta_1) & -\sin(\vartheta_1) & \dots & \dots & -N \cdot r^{N-1} \cos(N\vartheta_1) & -N \cdot r^{N-1} \sin(N\vartheta_1) \\ \vdots & \vdots & \ddots & \ddots & \vdots & \vdots \\ \vdots & \vdots & \ddots & \ddots & \vdots & \vdots \\ -\sin(\vartheta_{N_S}) & \cos(\vartheta_{N_S}) & \dots & \dots & -N \cdot r^{N-1} \sin(N\vartheta_{N_S}) & N \cdot r^{N-1} \cos(N\vartheta_{N_S}) \\ -\cos(\vartheta_{N_S}) & -\sin(\vartheta_{N_S}) & \dots & \dots & -N \cdot r^{N-1} \cos(N\vartheta_{N_S}) & -N \cdot r^{N-1} \sin(N\vartheta_{N_S}) \end{pmatrix}}^{2N} \Bigg\} 2N_S \quad (\text{III.19})$$

For a given measurement geometry and the according center of decomposition (given  $r, \vartheta_i$ ), the decomposition coefficients  $\vec{x}$  can thus be obtained by the solution of the inverse problem.

$$\vec{x} = \mathbb{A}^{-1}\vec{B} \quad (\text{III.20})$$

This formulation allows for the determination of the decomposition coefficients, if the inverse problem is at least well-defined in terms of the criteria given above.

This completes the theoretical framework of the measurement principle in two dimensions, which provides the toolbox for the decomposition of the magnetic field in spatial harmonics for current measurements of (near-) linear conductors. It can be used to obtain the desired geometrical selectivity as will be demonstrated below. A successful application of the toolbox requires adept knowledge of the various parameters that influence the measurement conditions. These are predominantly geometrical parameters, which can be analysed in two sequential stages:

- **Determination of measurement configuration (“dimensioning”):** this stage serves to find the best possible compromise between an **optimal** and a **practical** measurement configuration. Herein, the optimal configuration describes a solution of the measurement problem without constraints, i.e. those that one would choose for a simulation-only solution (‘infinite’ number of sensors and decomposition orders). In contrast, the practical solution is concerned with finding a configuration that can be fabricated, installed and operated at favourable effort and cost. The question is thus, which maximum decomposition order ( $N$ ), relative array position ( $d_0, \varphi_0$ ) and array radius ( $r$ ) will allow a sufficiently precise determination of a specific higher order coefficient that provides acceptable geometrical selectivity. The array position and radius affect the relative magnitude of higher order contributions and must thus be chosen to allow for the detection of these orders. Along with the number and distribution of sensors, they also affect the reconstruction quality which is another essential indicator of a successful application.
- **Analysis of potential error sources:** once a workable solution has been defined, the effect of errors in individual measurement parameters must be examined carefully, in order to prove the applicability of the measurement principle under on-site conditions.

These two aspects will be studied in the following section which is concerned with an in-depth analysis of all parameters that are used to describe and solve the measurement problem as it was presented above.

### III.2.2 Parametric analysis: dimensioning and error sources

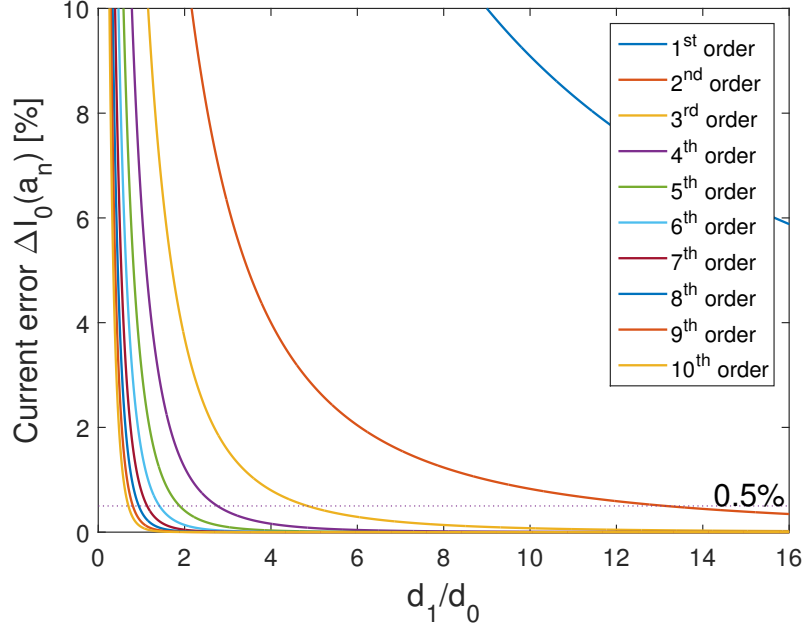
To evaluate, test and demonstrate the applicability of the current measurement measurement in complex environments, simulations have been conducted using MATLAB<sup>®</sup>. The aim is to assess the potential for geometrical selectivity between the three conductors of a tri-phase current distribution system with the additional perturbing influences of other (potential) magnetic field sources

(e.g. the earth magnetic field (EMF)). The range of suitable values for  $d_0$  is already defined by a typical conductor insulation radius in the low centimetre range (e.g. 2.5 cm) and the desire to keep the source-to-measurement distance  $d_0$  small, in order to maximize the suppression of perturbing effects. Along with the radius of the decomposition area  $r$ , which should principally be minimized in the interest of sensor miniaturisation, the distance  $d_0$  must be adapted to obtain measurable contributions from higher orders of the magnetic field. This proves an obstacle to the miniaturisation of the sensor. For the following simulations, the angular position is fixed at  $\varphi_0 = 180^\circ$  in order to simplify the parametric analysis by focusing on coefficients  $a_n$  only, since the coefficients  $b_n$  will be near-zero in this configuration (Eq. III.13) and the respective functions will therefore not contribute to the reconstruction of the magnetic field..

#### **Dimensioning - array radius $r$ and position $d_0$**

For each application of the measurement principle, the precision required by that application must be attainable using the given measurement conditions/geometry and the designed sensor array. For a given measurement environment, the first task is thus to determine the order necessary to achieve the required discrimination between field sources. This is predominately dependent on the relative distance of the array to the various sources. In a second step, the array radius and position must be adapted to allow for the determination of the order of interest. The considerations necessary to find suitable parameters that respond to these two tasks are presented in the following. For a system of two conductors and a sensor array placed on a line, so that the sensor is at distance  $d_0$  to the primary current  $I_0$  and a distance  $d_1 = d_0 + x$  to the secondary current  $I_1$  (where  $x$  denotes the distance between the two conductors), the order required to achieve a defined precision in current measurement with respect to the relative distance  $d_1/d_0$  can be deduced from Fig. III.8. For this graph, the distance  $d_0$  is kept constant at  $d_0 = 6$  cm and the secondary conductor, with  $I_0 = I_1$ , is shifted along the line connecting array and conductor centres. From this evaluation, it is possible to deduce, that for a typical ratio of  $d_1/d_0 = 3$  to 4, the fourth order of the decomposition can be used to determine the current with a precision of  $\Delta I_0 \leq 0.5\%$ . This however only provides one half of the answer to the dimensioning problem, since it is also necessary to be able to detect this order of interest.

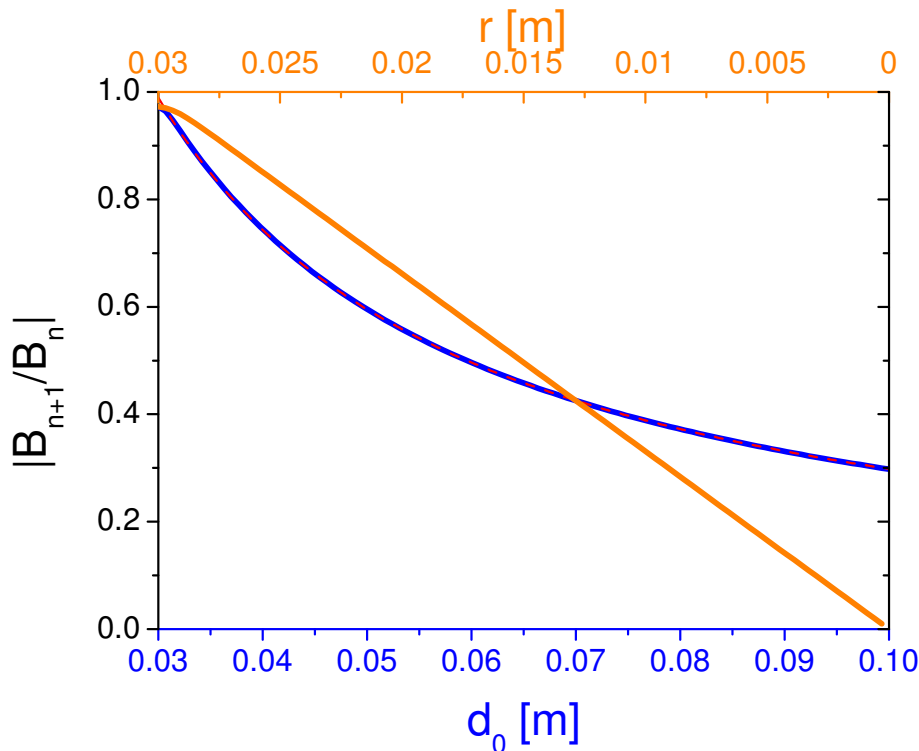
As derived above (Eq. III.16), the relative magnitude of an order  $B_{n+1}$  with respect to the next lower order  $B_n$  depends on the sensor array radius  $r$  and the distance  $d_0$  of the measurement area to the primary conductor. Since both enter into the equation to the power of  $(n - 1)$  or  $n$ , respectively, these two parameters determine the maximum number of orders required for a “complete” decomposition. In effect, this means that the closer the decomposition center is to



**Figure III.8:** Precision of current determination using different orders of the spatial harmonics decomposition and for different relative perturber-to-primary conductor distances  $d_1/d_0$ . Both conductors carry a current of  $I_0 = I_1 = 100$  A and the array is situated at  $d_0 = 6$  cm, with the centres of both conductors and the array situated on a line. The decomposition is performed with a large number of bi-axial sensors ( $N_S = 50$ ) and up to a high order  $N = 20$ , in order to obtain a complete description of the magnetic field.

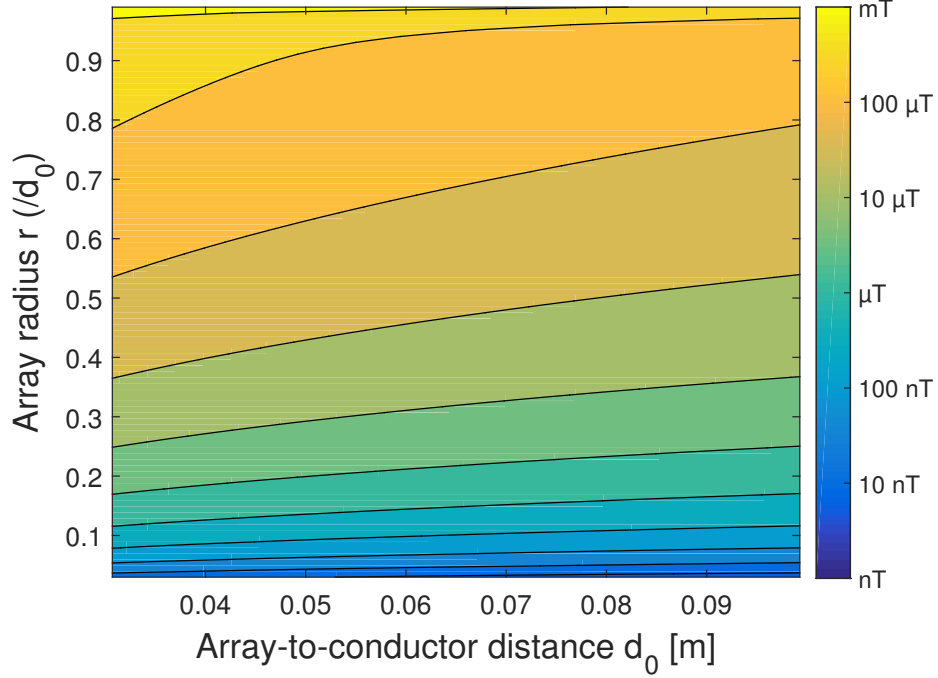
the field source, the more orders are required to reconstruct the field to a certain precision. For an increasing distance to the source  $d_0 \rightarrow \infty$ , the maximum decomposition for complete field reconstruction approaches  $N \rightarrow 1$ . It is therefore essential to find parameters for the array size and position that allow for the detection of the order that provides the required geometrical selectivity.

Fig. III.9 illustrates the influence of changing the array radius  $r$  and relative position  $d_0$  on the relative magnitude of the contribution of each order (with respect to the first order) to the field reconstruction, with the other parameter fixed at  $d_0 = 11$  cm and  $r = 3.2$  cm, respectively. The simulations confirm that, for a current conductor, the first order contribution is always of comparable magnitude to the actual field, while higher orders exhibit a decreasing contribution that is also evident in a simulation of the magnetic field along the circumference of the decomposition circle for the 2D field (Fig. III.5). For the selection of a suitable array radius for a given range of values  $d_0$ , it proves meaningful to perform the spatial harmonics decomposition for various combinations of the two parameters, in order to determine the resulting magnitude of a specific desired coefficient. For the case at hand, this analysis is presented for the fourth order in Fig. III.10, for a primary



**Figure III.9:** Relative magnitude of an order  $B_{n+1}$  with respect to the next lower order  $B_n$ , in dependence of the sensor array radius  $r$  and the array center-to-conductor distance  $d_0$ . The dependence on  $r$  is linear for successive orders and the dependence on  $d_0$  is reciprocal (indicated by red  $1/d_0$  fit).

current of  $I_0 = 100$  A (to allow for easy scaling using lower currents). This type of figure should be consulted when the parameters of a specific sensor technology are known, in order to conclude whether the desired order will be detectable with a specific sensor and array radius or to define the minimum array radius required for this determination. The influence of the array radius and array-to-conductor distance carries direct consequences for the dimensioning of a laboratory or industrial prototype. For example, while a miniaturisation of the sensor is desirable, the contribution and relative magnitude of higher orders is reduced as the decomposition/reconstruction volume is reduced for a fixed separation between the source and the center of decomposition. Thus, the sensor array radius cannot be reduced at will if higher orders are to remain detectable. The analysis of the influence of the two parameters on the attainable precision for current determination and the detectability of the higher order contributions, allows for a determination of suitable sensor array parameters for a laboratory prototype. Fig. III.8 indicates that the fourth order is sufficient



**Figure III.10:** Magnitude of fourth order contribution  $B_4$  to the reconstruction of the magnetic field for various combinations of the array-to-conductor distance  $d_0$  between 3 and 10 cm and the array radius  $r$  with respect to that distance. The current magnitude is  $I_0 = 100$  A a large number of orders ( $N = 20$ ) and sensors ( $N_s = 50$ ) are used to ensure an accurate determination of the coefficient values.

to determine the current with a precision of  $\Delta I_0 \leq 0.5\%$ , and Fig. III.10 shows that this order can be detected if the sensor solution can be used to determine variations on the sub- $\mu\text{T}$  scale and the ratio  $r_0/d_0 \sim 0.5$ . These conclusions will be used for the definition of a test case below and later on for the design of a laboratory prototype. Once the array dimensions and configuration have been defined an analysis of potential errors sources is also possible and is presented towards the end of the section.

### Test case for laboratory conditions

The above considerations allow a definition of suitable array parameters for specific measurement conditions. Depending on the desired measurement precision and the employed sensor technology, it is then possible to determine a suitable combination of array radius  $r$  and distance  $d_0$ , in order to determine and exploit the decomposition order/coefficient of interest. For the laboratory

tests that will be detailed below, it was clear that the values for  $d_0$  would be in the centimetre range (since  $d_0$  is the distance between the center of decomposition and the center of the conductor, it must necessarily be larger than  $r$ ) and the perturbing conductor would be in the range of several tens of centimetres. According to the evaluation of the required order to reach a current determination precision of 0.5% presented in Fig. III.8, the decomposition should thus be performed up to the fourth order. The radius must be sufficiently large to allow for the discrimination of the fourth order from the sensor noise, so that a choice of  $r = 3.2$  cm for the array radius was deemed adequate (see also the presentation of the sensor technology in the following chapter). For applications of the sensor in the field, the radius will always be a parameter that is fixed once at fabrication while the parameter  $d_0$  depends on the installation conditions but will also be adapted as best possible with respect to the above principles. Furthermore, an equidistant distribution of the sensors along the circle of given radius could be confirmed as the best solution for the 2D case, since it provides optimal spatial sampling. Since the definition of optimal or at least advantageous configurations is more complicated for the 3D case, the intricacies of different options for sensor distribution are discussed in the relevant section below and some of the implications can then also be transferred to the 2D case.

The test parameters that correspond to the array values used for the 2D prototypes and the dimensions of the laboratory setup are:

**2D sensor array parameters:**  $r = 3.2$  cm;  $N_S = 10$  at  $\vartheta_i = j \cdot \frac{2\pi}{10}$  for  $j = 0, 1 \dots 9$

**Setup parameters:**  $d_0$  in the cm range,  $\varphi_0 = \pi$ ;  
 $x > d_0$ ,  $d_1 = \sqrt{x^2 + d_0^2}$ ,  $\varphi_1 = \frac{\pi}{2} + \tan^{-1}\left(\frac{d_0}{x}\right)$

As will be detailed below for the fabrication of the laboratory prototype, the 2D sensor array and, accordingly, the test case will be based on mono-axial measurements of the component  $B_\vartheta$ , i.e. with the sensor axis oriented tangentially at each equidistant point on the circle.

After fabrication of a sensor array designed to suit these principles and its positioning in the field, the application of the measurement principle will be subject to variations of the obtainable precision with variations of input parameters. The influence of these parameters will be studied in the following section.

#### Error sources

Mispositioning of the sensor array relative to the field source (parameters  $d_0$  and  $\varphi_0$ ) or of the sensor positions within the sensor array (parameters  $r$  and  $\vartheta_i$  for  $i = 1 \dots N_S$ ) as well as misalignment

of the sensor measurement axis ( $\vec{B}_r$  and or  $\vec{B}_\vartheta$ ) are potential sources of errors and their effects on the measurement precision must be evaluated carefully. The array positioning accuracy is determined by the on-site conditions. The possibility to determine and correct the two parameters during operation are discussed in the following section. The intrinsic errors of the sensor array may be due to the precision of fabrication technology and they can potentially be corrected using in-factory control methods. However, the correction can only be helpful to the extent that the sensor parameter offset does not inhibit the quality of the measurement, e.g. a strong out-of-plane rotation of a measurement for a straight conductor will result in a significant decrease of the measured magnetic field magnitude. The individual parameters and sources of error are summarized in Table III.1 and will be discussed in the following subsections. Although the fourth order was identified as the order of interest above, the test case and laboratory prototype use 10 mono-axial measurements at each position. According to the formulation of the spatial harmonics problem (Eqs. III.5-III.6), the determination of the fourth order requires (at least) eight measurements. Ten sensors were chosen for the tests here, since this allows for more detailed analysis (e.g. evaluation using eight, nine or ten sensors). This setup would theoretically allow for the determination of the fifth order coefficients as well, however, since the sensor array radius is designed to be as small as possible while allowing for the detection of the fourth order, the fifth order contribution is at the brink of the sensor noise of available sensor and is thus not expected to be measurable. Given the test case defined above, it is now possible to proceed with an analysis of potential errors sources for the current determination process.

### Intrinsic array parameters

The matrix  $\mathbb{A}(r_i, \vartheta_i)$  (Eq. III.19) depends on the geometry of the sensor array and any imprecision in these parameters is included in the solution of the inverse problem. Since the matrix only depends on the array-intrinsic geometrical parameters, the source of error is limited to fabrication

	<i>Parameters</i>		<i>Potential error (types)</i>		<i>Correction</i>
Array-intrinsic /fabrication	$r, \vartheta_i$	sensor position in array	$\Delta r, \Delta \vartheta_i$	systematic or random	factory characterization
	$\vec{B}_r, \vec{B}_\vartheta$	axis alignment	$\alpha, \beta$	in-/out-of-plane rot. systematic or random	
On-site	$d_0, \varphi_0$	source position with respect to array	$\Delta d_0, \Delta \varphi_0$	systematic error/ variation over time	calibration

**Table III.1:** Summary of sensor array positioning and alignment parameters with respective sources of error

### III.2. 2D magnetic field decomposition in spatial harmonics

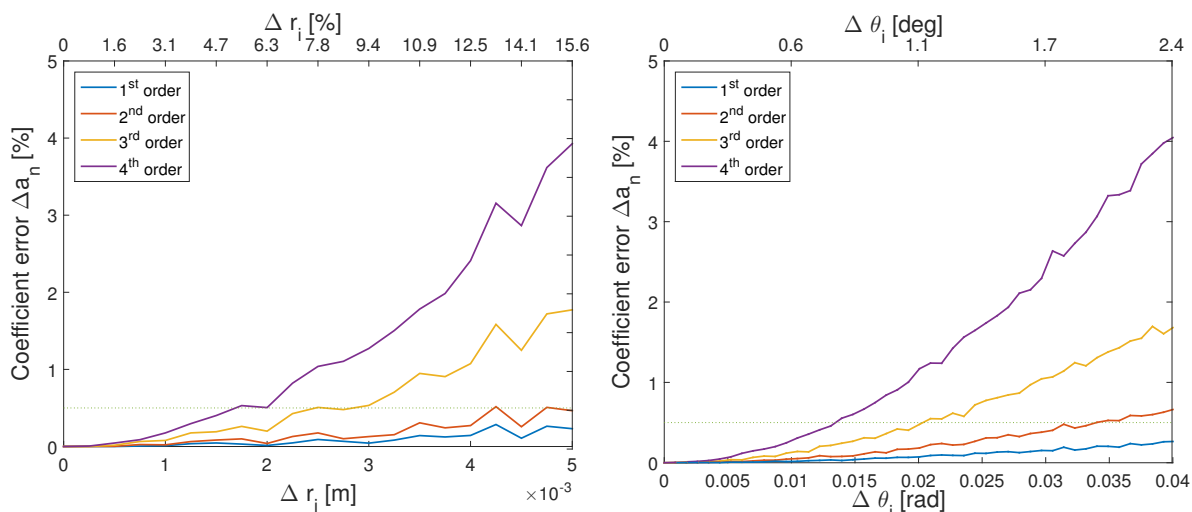


**Figure III.11:** Coefficient error for random errors of the given magnitude for the radial (left) and angular (right) position of the individual (10) sensors. Results are averaged for 1000 values for each offset. Array parameters as described in the test case,  $d_0 = 6$  cm,  $\varphi_0 = 180^\circ$  and  $I_0 = 100$  A.

errors (assuming that the sensors are fixed on a support in a way that prevents shifting/rotation over time, i.e. due to temperature or vibration effects). On a second level, the effect of these fabrication errors can be distinguished between the case where the errors are recognized and determined (but still different from the *a priori* parameters, or non-uniform e.g. distribution of array radii values for the set of sensors  $A(r) \rightarrow A(r_i)$ ) and the case where wrong parameter values are assumed and entered into the inverse problem. The unidentified, and thus uncorrected, variations in the later case will result in coefficient errors. While the collective rotation of the sensor array (and thus positions  $\vartheta_i$ ) results in very limited errors in the coefficient values ( $< 0.1\%$  for all orders 1 through 4), a systematic error of  $\pm 1$  mm in the array radius  $r$ , can lead to errors up to 0.15, 0.6, 1.7 and 4.3 % for the first to fourth order coefficients respectively. If the exact coefficient value is desired, the fabrication accuracy (and the parameter stability over time), should thus be well below  $\pm 1$  mm for the array radius. However, as described above, a linear and stable transfer factor  $k_{a_n}$  is the pivotal point for precise current measurements. As long as the array parameters do not vary (significantly) over time, the transfer factor will not be affected. If a significant change in array parameters (primarily position) does occur, a new determination (e.g. calibration) of the transfer factor would be required. Fig. III.11 displays the coefficient error for  $a_n(\Delta r_i, \Delta \vartheta_i)$  that results from random misalignments in the radial and angular position of individual sensors for the test case with  $N_S = 10$  sensors (see test case defined above). The results present the mean value of 1000

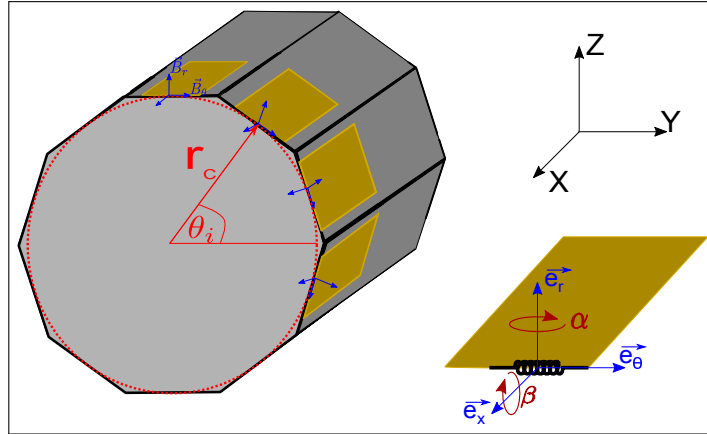


**Figure III.12:** Definition of misalignment/Euler angles ( $\alpha, \beta$ ) with respect to the measurement axes

simulations with a normal distribution of the given span applied to the respective parameters. It can be observed that the level of error increases with every higher order. This is due to the reduced magnitude (and contribution to the reconstruction of the field) of each order, which was discussed above and which leads to an increased susceptibility to variations for these 'weaker' orders. The evaluation shows that, for the array radius  $r$ , the range of errors for individual  $r_i$  of each sensor should be kept below 5%, in order to keep the coefficient error – and consequently the current error – below 0.5%. The range of possible angular position offsets should be limited to  $\pm 0.7^\circ$  in order to meet the precision requirements. Again, as long as these parameters do not vary by the given amounts over time (after determination/calibration of the transfer factors and before the next determination), the precision of the current measurement is not affected. The provided error values are calculated with respect to the ideal case with no sensor mispositioning or misalignment. Since the identification of the 'true' (ideal) coefficient values is not the objective here, and since the analytical formula for the relation  $a_n = k_{a_n}(I_0)$  will not be applied for current determination, the obtained enhanced errors in higher order coefficients is not a point of concern. However, the dependence of the coefficients on the different array parameters is an important characterisation step that allows for a well-founded understanding of the measurement method and may still come in handy, e.g. if substantial variations of array parameters are observed over time.

### Sensor orientation/rotation offsets

The misalignment of the sensor is considered with respect to the measurement axes and thus depends on the sensor position. The in- and out-of-plane rotations are also depicted in Fig. III.12. For

### III.2. 2D magnetic field decomposition in spatial harmonics

the 2D array, with the sensors arranged in a circle and the measurement axes aligned tangentially along  $\vec{B}_\vartheta$ , the adequate choice of orthogonal coordinate axes is  $\vec{e}_x, \vec{e}_r, \vec{e}_\vartheta$ . Consequently, rotations around  $\vec{e}_x$  and  $\vec{e}_r$  result in misalignments with respect to the theoretical measurement axis  $\vec{B}_\vartheta$  and the respective rotation angles are designated  $\beta$  and  $\alpha$  (see III.12).

The errors of coefficients  $a_1$  to  $a_5$  that results from random rotation offsets within the range 0 to  $\pm 2^\circ$  are displayed in Fig. III.13 for the test case. For the simulation of each error range  $\pm\alpha/\beta$ , normally distributed random errors are applied to each of the 10 sensor positions, and the simulation is performed 1000 times to obtain a statistical average of the resulting errors. The simulations show that the measurement method is equally susceptible to both misalignment angles, although variations in  $\beta$  exhibit stronger fluctuations (especially the fourth order) for equal samples sizes. The error that results from a misalignment along both axes simultaneously, i.e. misalignment offsets defined by  $\pm\alpha, \pm\beta$  in which the measurement axis  $\vec{e}_\vartheta$  can be found, is thus a sum of the two errors, so that the simultaneous misalignment must be kept below  $1.7^\circ$ , in order to keep the coefficient error below 0.5%. It should be kept in mind, that, in the interest of comparability, the simulations are performed for a test case that approaches the laboratory conditions, which will be presented later on. For other relative array positions and array parameters (e.g. sensor number), the behaviour and susceptibility to error sources will not be identical. For different application cases, similar simulations should be performed to establish an understanding of the influence of the various parameters.

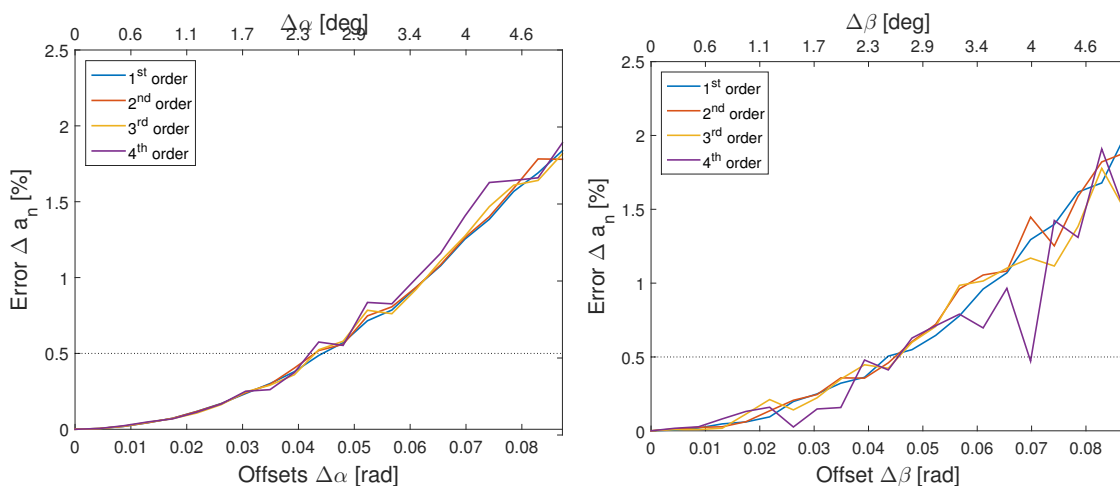


**Figure III.13:** Coefficient errors for rotation offsets around  $\vec{e}_r$ :  $\alpha = 0$  to  $\pm 2^\circ$  (left) and around  $\vec{e}_x$ :  $\beta = 0$  to  $\pm 2^\circ$  (right). Simulated for 1000 random values within a given range and with a normal distribution. The remaining simulation parameters correspond to the 2D test case, with  $d_0 = 6$  cm.

After the study of individual sensor misalignments, it is now possible to return to an error that affects the array as a whole.

### **Out-of-plane rotation of measurement array**

In respect to array positioning and the variation of an array position over time for the 2D measurement problem, it is also important to consider the possibility of deviation from the assumption that the measurement array is perfectly positioned in the plane of the magnetic field. Deviations from the alignment within the plane can be expected to have a stronger impact on the current measurement precision than errors in the array parameters, because they will take place on-site under operating conditions. A characterisation and correction will thus be further complexified.

To study the effect of such out-of-plane rotations of the entire measurement array, the following convention is assumed for a coordinate system in the center of the measurement array/decomposition area: the direction of current flow is defined to be parallel to the  $x$ -axis, i.e. the current flow only results in a field in the  $[y, z]$ -plane. The array can then be rotated out of the ideal measurement plane by rotations around either of the two axes  $\vec{e}_y$  or  $\vec{e}_z$ . For rotations around  $\vec{e}_z$ , the field measurements will reduce in magnitude as the sensor axis is tilted increasingly in the direction of current flow, while for rotations around  $\vec{e}_y$ , the array still measures the correct component of the field  $\vec{B}_\vartheta$  but at positions that deviate from those assumed in the inverse problem formulation. The effects of such rotations (up to  $10^\circ$ ) on the coefficient values for the first four orders is presented in Fig. III.14. The analysis demonstrates that the out-of-plane rotation should be limited to  $< 3$  to  $4^\circ$ , in order to keep the error in the fifth error coefficient below 0.5% in either case and that rotation around  $\vec{e}_y$  is slightly more harmful for the measurement method. A combination of both rotations leads to a summing of individual errors and should therefore not exceed  $2^\circ$ .

The potential error sources listed and examined above need to be taken into account when analysing a specific measurement task. These variations in geometrical parameters may also be induced by temperature variations, wind or mechanical effects on-site, depending on the installation method. The analysis was performed with respect to variations in coefficient values  $a_n$  since these present the direct result of the measurement method. Except for the misalignment effects, for which the errors were comparable for all orders, the higher order coefficients showed a much stronger susceptibility to variations than lower orders. This can be explained by the decreasing relative magnitude of the field contributions with increasing errors.

The majority of the the error sources presented above are expected to be subject to variation during the fabrication process, in which case a characterisation of the sensor array allows for a correction of these errors. If these errors appear over time, it is possible to differentiate between

### III.2. 2D magnetic field decomposition in spatial harmonics

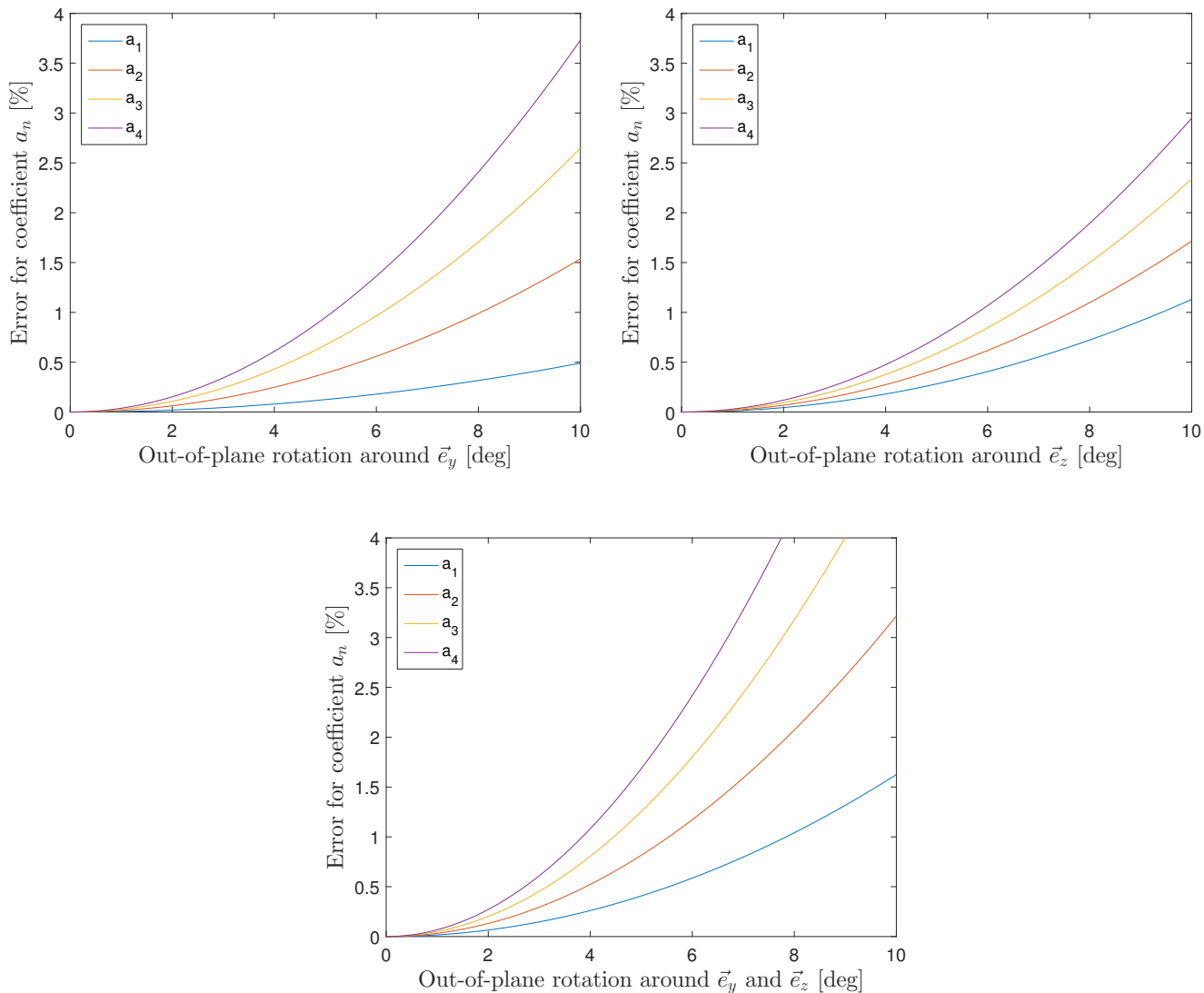


**Figure III.14:** Error induced by out-of-measurement plane rotations of the array around  $\vec{e}_y$  (top left),  $\vec{e}_z$  (top right) or a combination of both rotations (bottom). Simulation parameters: decomposition order  $N = 5$ , 10 mono-axial sensors ( $\vec{B}_\vartheta$ ),  $I_0 = 10$  A,  $d_0 = 6$  cm,  $\varphi_0 = 180^\circ$

a favourable and a less favourable case. The former applies to permanent variations in array parameters, these could be compensated by periodic applications of the calibration method that will be presented in the following section. However, in the second case, the parameters could exhibit random fluctuations within a given parameter range over time. In this case, it would be

very difficult to maintain a certain precision and these variations should thus be kept below the limits obtained for  $\Delta a_4 < 0.5\%$  (or a different coefficient for another application case).

Significant changes in the coefficient values would inevitably lead to a change in transfer factors  $k_{a_n, b_n}$ , which present the central parameters for the precision of current determination. Above, it has already been established that the transfer factors depend on the relative array-to-conductor position, i.e.  $k_{a_n, b_n} = k_{a_n, b_n}(d_0, \varphi_0)$ . Due to the proportionality  $k_{a_n} \propto 1/(d_0)^n$ , this error increases rapidly with each successive decomposition order. The dependence on the angular position is also well-defined by the analytical expression, through  $k_{a_n} \propto \cos n\varphi_0$ . The obtained precision in the transfer factors ultimately defines the robustness of the current measurement method. A means of control over this parameter is thus of paramount importance and a possible solution that allows for a compensation of variations in array position, and also of the variations in array parameters presented above, will be presented in the following section. For reasons of simplicity, the calibration method will be introduced for the 2D measurement problem (in particular because the analytical expressions for the coefficient values allow for a more intuitive explanation). As will be clear from the following discussion, an extension of the calibration method to the three-dimensional measurement problem, which is introduced directly afterwards, will also be possible as long as the coefficients exhibit the same dependence on the current of interest.

A brief overview of the concepts established in this section is meaningful before proceeding with the presentation of the calibration method. Besides the introduction of the spatial harmonics approach and the description of the internal decomposition problem, it was possible to confirm by simulation that the measurement principle offers the necessary geometrical selectivity which is required to measure currents with a precision of  $< 5\%$  in a multi-conductor system. A dimensioning stage allowed the definition of suitable sensor array parameters for a laboratory prototype, which allow for a detection of the desired decomposition order and the established test case then served as a reference for the analysis of error sources that can affect the measurement method. In conclusion, this section provided the necessary proof-of-concept and array design parameters, and thus the theoretical foundation for the implementation of a 2D current sensor prototype, which will be discussed in the following chapter. As noted above, the theoretical framework will be strengthened, through the development of the calibration method, and extended, to a 3D measurement principle, before the practical aspects can be discussed in detail.

### III.3 Calibration procedure (2D case)

#### III.3.1 Calibration of transfer factor - general considerations

To present the developed calibration method, the case of a single cable/conductor is initially investigated and the problem is subsequently complexified to approach the actual on-site conditions. The following considerations concern the on-site calibration of the sensor array, i.e. the determination of the transfer factor  $k_{a_n, b_n}(d_0, \varphi_0)$  that depends on the position of the array with respect to the conductor. It is thus assumed that the intrinsic values of the array, the sensor positions with respect to the center of decomposition (the center of the circle)  $[r_i, \varphi_i]$  have been determined with the required precision either due to sufficiently precise fabrication standards or to an in-factory array calibration step. The array is subsequently installed on-site, where variations in the installation position will occur naturally, and the following two subsections deal with the possibilities to determine the transfer factors once it has been installed. Here, two cases must be differentiated depending on whether it is possible to inject a defined current into the conductor or whether the calibration must be carried out under operating conditions. In either case, a variation of the relative sensor position requires a re-calibration of the transfer factors.

#### **Injection of known current**

If the conditions on-site allow for the injection of a known current  $I_0$ , the linear dependence of the coefficients  $a_n, b_n$  on the current can be exploited to determine the transfer factors (Eq. III.13 for the analytical expression). For example, in the laboratory setup described in the following chapters, a sweep of current values allowed for the determination of the relationship  $a_n(I_0)$  (or  $b_n(I_0)$ ) and thereby the transfer factor for each coefficient value, for a given position of the array after installation. If the array is subsequently moved with respect to the conductor, a new determination of the transfer factor would be required.

#### **Unknown current (operating conditions)**

If the calibration has to be carried out under operating conditions, the current magnitude will not be known during calibration of the sensor position. To solve this problem, it is possible to work

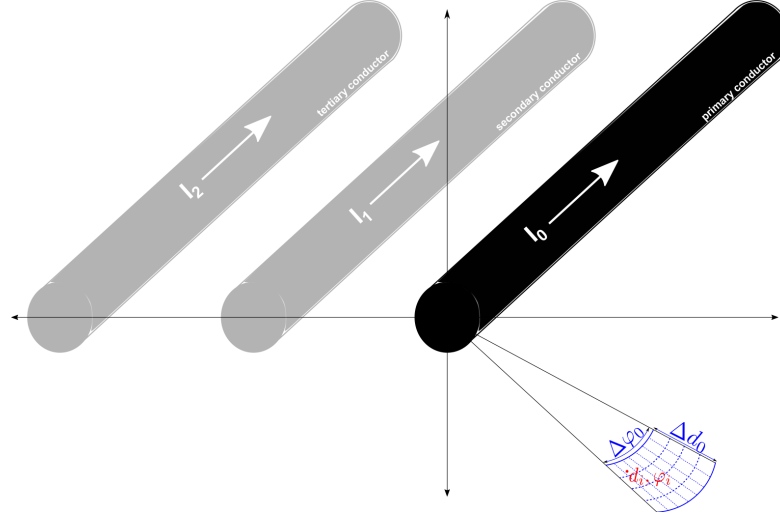


**Figure III.15:** Geometrical considerations for the calculation of a reference matrix  $\mathbb{M}_{n+1,n} [d_{ref}, \varphi_{ref}]$  for a given set of possible array locations  $[d_0, \varphi_0]$ .

with the coefficient ratio  $\frac{a_{n+1}}{a_n} := a_n^{n+1}$  which is independent of the current  $I_0$ .

$$\begin{aligned} \frac{a_{n+1}}{a_n} &= \frac{(n+1)d_0^{n+1}}{nd_0^n} \cdot \frac{I_0 \cos[n\varphi_0]}{I_0 \cos[(n+1)\varphi_0]} \\ &= d_0 \frac{n+1}{n} \cdot \frac{\cos[n\varphi_0]}{\cos[(n+1)\varphi_0]} \end{aligned}$$

These ratio values can be compared to an *a priori* value database  $\mathbb{M}_{n+1,n} [d_{ref}, \varphi_{ref}] = \mathbb{M}_{n+1,n} [k_{a_n, b_n}]$ , which has been calculated for a range of possible array positions (Fig. III.15), in order to determine the correct transfer factors  $k_{a_n, b_n}$ . The database must cover the range of possible transfer factors and thus combinations of  $[d \pm \Delta d, \varphi \pm \Delta \varphi]$ . To improve convergence of the search algorithm, the installer can also enter approximate values  $[d^*, \varphi^*]$  based on his estimation after installation. The best match between the reference values from the *a priori* database and the ratios obtained for a specific sensor position  $(a_n^{n+1}, b_n^{n+1})$  can be used to determine (or at least approximate to a satisfying level) the actual position of the sensor array, which can then (after calibration) be used to deduce the current value at an arbitrary moment in time using the relations  $a_n(I_0), b_n(I_0)$ . For example, the following optimisation is performed for  $\varphi_0 \approx 180^\circ$  (near-zero coefficients  $b_n$ ) To find the sensor position among the set of reference values that best fits the determined values for the

### III.3. Calibration procedure (2D case)

$I_1$ =	Mean error [%]					
	$\Delta d_0$	$\Delta \varphi_0$	$\Delta k_4$	$\Delta d_0$	$\Delta \varphi_0$	$\Delta k_4$
	without noise			with noise (SNR= 33 [dB])		
0 [A]	0.11	0.09	0.25	0.52	0.13	2.02
$0.5I_0$	0.28	0.15	1.15	0.57	0.14	2.25
$1I_0$	0.58	0.16	2.40	0.71	0.16	2.86
$2I_0$	1.20	0.21	4.90	1.22	0.21	4.90

**Table III.2:** Error of calibration procedure for test series of 12c values between  $d_0 \in [5 \dots 12] \text{cm}$  and  $\varphi_0 \in [178 \dots 182]^\circ$  and for various degrees of perturbation. The calibration uses a combination of the ratios  $\frac{b_3}{a_4}$  and  $\frac{a_3}{a_4}$ . Reference matrices calculated with  $N_S = 50$ ,  $N = 20$  and  $r = 3.2 \text{ cm}$  and 1000 steps in each range. Perturbing conductor  $I_1$  at  $x = 40 \text{ cm}$  lateral displacement from  $I_0$ . The same parameters were used to simulate measurements at random positions within the given ranges. The results are also provided for a given signal-to-noise ratio applied to the measurements. For these, the mean error is (additionally) averaged over 1000 simulations to obtain reliable results.

installed array, the following optimisation is carried out:

$$\min_{\forall i,j} \sum_{n=1}^{N-1} \left\| \left[ \begin{array}{c} a_{n+1} \\ a_n \end{array} \right]_{\text{exp}} - \mathbf{M}_{a_n}^{n+1}(i,j) \right\| + \left\| \left[ \begin{array}{c} b_{n+1} \\ a_n \end{array} \right]_{\text{exp}} - \mathbf{M}_{b_n}^{n+1}(i,j) \right\| \quad (\text{III.21})$$

The equation above presents the compound case, for which the sum of deviations of all available ratios for a maximum decomposition order  $N$  is minimized. Evidently, it is also possible to determine the minimum for a single ratio and the reference values or, e.g., for all ratios of the coefficients  $a$  or  $b$  only or using ratios of different coefficients. Once the minimum has been determined, the corresponding indices  $(i, j)$  can be used to deduce the transfer factor  $k_{a_n, b_n}(d_0, \varphi_0)$ . For a calibration under operating conditions, only coefficient ratios involving the higher orders can be employed, in order to minimise the error induced by perturbing sources. For the array dimensions and setup used for the test simulations in the last section, a combination of the ratios  $\frac{b_3}{a_4}$  and  $\frac{a_3}{b_4}$  provides the highest precision for simulations of the calibration procedure. The results are provided in Tab. III.2, which presents the mean error for a test series composed of positions within a defined range (which corresponds to the limits of the reference matrix). The error in the transfer factor  $k$  is the most relevant parameter, since this is used for the current determination. As it depends on both the distance and angular position, the error of the transfer factor will always be larger than those of the geometrical parameters. The fact that the error in the distance  $d_0$  is always larger than that in  $\varphi_0$  can be explained by the different relative step sizes. To calculate the reference matrix for a more equally divided region, it would be necessary to determine an individual number of steps for each parameter. The effect of sensor noise on the calibration precision can also be deduced from

the table. For the given signal-to-noise ratio of  $SNR = 33$  dB, which presents an upper limit for the sensor technology introduced in the following chapter, the mean error of the calibration procedure is significantly increased without perturbations. The influence of the perturbation then becomes increasingly decisive with higher relative current magnitudes, until it becomes the dominant factor at  $I_1 = 2I_0$  (for the given configuration).

Based on the above explanations, it becomes clear that the degree of detail of the reference matrix  $\mathbf{M}$  is decisive for the precision of the transfer factor determination. In turn, this depends on the step size  $\Delta s$  in relation to the sampling volume  $[d \pm \Delta d, \varphi \pm \Delta \varphi]$ . Figure III.16 displays the effect of the step size in  $d_0$  and  $\varphi_0$  on the determination accuracy for both parameters. Obviously, a smaller step size for a given area/volume results in a larger reference matrix and demands more memory storage.

The proposed calibration method thus offers the potential to determine the transfer factors with a high precision under live operating conditions. The exact accuracy depends on the exact application conditions, specifically the distance of the perturbing conductor, which will always carry current of similar magnitude. If the precision obtained with coefficients up to a given order  $N$  is insufficient for a given application, a adaptation of the sensor array to include more sensors and to allow the determination using the next higher order should be considered in order to enhance the geometrical selectivity of the calibration method. The method applies equally to AC and DC measurements. For AC measurements, the attainable precision can be optimized by determining the opportune moment for the calibration method, i.e. the moment in which the primary current is at its peak value, while the dephased perturbing conductors are at considerably lower current magnitudes. This approach offers the potential to improve the geometrical selectivity of the calibration method.

The presentation of the current-independent calibration method concludes the discussion of the 2D measurement approach which is applicable for 2D magnetic fields, as created by straight conductors. A solution that can be applied for all magnetic fields with components in all spatial dimensions is obtained using spherical harmonics and using suitable 3D sensor arrays. The theoretical framework of this will be discussed in the following section. After the discussion of the 3D solution, it will become clear that the calibration method is equally applicable for both approaches. It was presented here, because the analytical formulations that are available for the 2D problem allow for a more intuitive explanation of the operating principle.

### III.4. 3D spherical harmonics decomposition

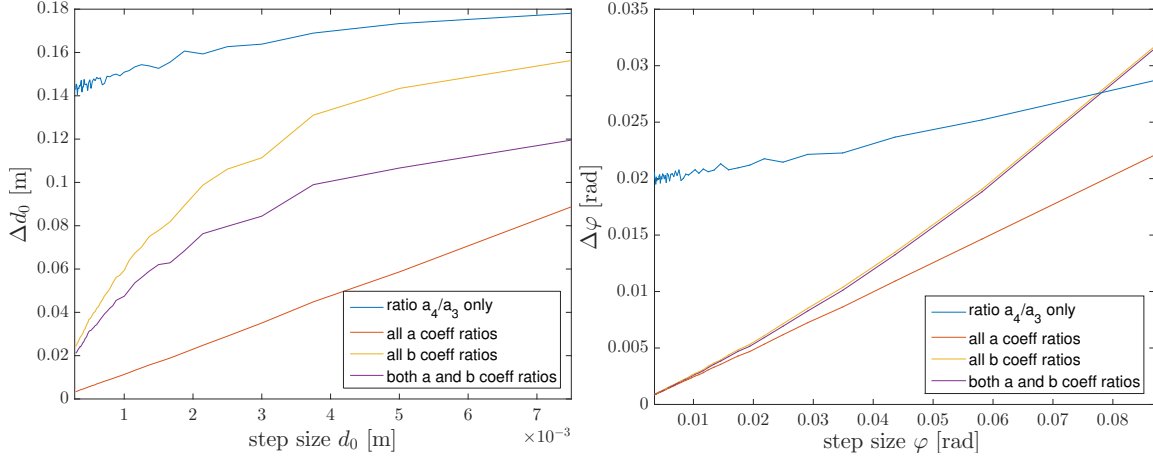


**Figure III.16:** Effect of decreasing step size/interpolation mesh for the determination of  $d_0$  and  $\varphi_0$  using a) the ratio  $\frac{a_4}{a_3}$  only b) all ratios of a coefficients c) all ratios of b coefficients and d) all coefficient ratios. The total area for the decomposition center was  $[r = 0.05 \dots 0.08] \times [\varphi_0 = 50^\circ \dots 80^\circ]$ .

### III.4 3D spherical harmonics decomposition

The use of a three-dimensional model for the field and the according spatial decomposition functions represent a generalization of the two-dimensional solution discussed in the previous section. The basis will be a coordinate system that is suitable for the exploitation of symmetries that may apply based on boundary conditions in three dimensions and the corresponding set of functions that is adapted to these coordinates. The vector potential can then be expanded in terms of these functions. Analogous to the expansion in two dimensions (Eq. III.1) and in accordance with the choice of coordinate system, the three-dimensional scalar vector potential  $\Psi$  must fulfil the Laplace equation in spherical coordinates<sup>[37]</sup>:

$$\Delta \Psi(r, \vartheta, \varphi) = \left[ \frac{1}{r^2} \frac{\partial}{\partial r} \left( r^2 \frac{\partial}{\partial r} \right) + \frac{1}{r^2} \Delta_{\vartheta, \varphi} \right] \Delta \Psi(r, \vartheta, \varphi) = 0$$

with

$$\Delta_{\vartheta, \varphi} = \frac{1}{\sin \vartheta} \frac{\partial}{\partial \vartheta} \sin \vartheta \frac{\partial}{\partial \vartheta} + \frac{1}{\sin^2 \vartheta} \frac{\partial^2}{\partial \varphi^2} \quad (\text{III.22})$$

The spherical harmonics  $Y_{nm}(\vartheta, \varphi)$  are the eigenfunctions of order  $n$  and degree  $m$  of the operator  $\Delta_{\vartheta, \varphi}$ :

$$\begin{aligned} Y_{nm}(\vartheta, \varphi) &= \sqrt{\frac{2n+1}{4\pi} \frac{(n-m)!}{(n+m)!}} P_n^m(\cos \vartheta) e^{im\varphi} \\ \text{with } n &= 0, 1, 2, \dots \quad m = -n, -n+1, \dots, 0, \dots, n-1, n \\ \Delta_{\vartheta, \varphi} Y_{nm}(\vartheta, \varphi) &= -m(m+1) Y_{nm}(\vartheta, \varphi) \end{aligned} \quad (\text{III.23})$$

with the associated Legendre polynomials  $P_n^m(z)$  that are related to the Legendre polynomials  $P_n(z)$  as follows:

$$\begin{aligned} P_n^m(z) &= (-1)^m (1-z^2)^{m/2} \frac{d^m}{dz^m} P_n(z) \\ P_n(z) &= \frac{1}{2^n n!} \frac{d^n}{dz^n} (z^2-1)^n \end{aligned} \quad (\text{III.24})$$

The general solution for the vector potential in spherical coordinates is:

$$\Psi(r, \vartheta, \varphi) = \frac{\mu_0}{4\pi} \sum_{n=0}^{\infty} \sum_{m=-n}^{+n} \left( a_{nm} r^n + \tilde{a}_{nm} r^{-(n+1)} \right) Y_{nm}(\vartheta, \varphi) \quad (\text{III.25})$$

The relevant variable is again the magnetic induction  $\vec{B}$  for which the following relations are obtained for the internal decomposition problem (using functions proportional to  $r^n$ ):

$$\vec{B}(r, \vartheta, \varphi) = -\vec{\nabla} \Psi^{\text{int}}(r, \vartheta, \varphi) = -\frac{\mu_0}{4\pi} \sum_{n=0}^{\infty} \sum_{m=-n}^{+n} a_{nm} \vec{\nabla} [r^n Y_{nm}(\vartheta, \varphi)] \quad (\text{III.26})$$

$$\vec{B}_r(r, \vartheta, \varphi) = -\frac{\mu_0}{4\pi} \sum_{n=0}^{\infty} \sum_{m=-n}^{+n} a_{nm} n r^{n-1} Y_{nm}(\vartheta, \varphi) \quad (\text{III.27})$$

$$\vec{B}_{\vartheta}(r, \vartheta, \varphi) = -\frac{\mu_0}{4\pi} \sum_{n=0}^{\infty} \sum_{m=-n}^{+n} a_{nm} r^{n-1} \frac{dY_{nm}(\vartheta, \varphi)}{d\vartheta} \quad (\text{III.28})$$

$$\vec{B}_{\varphi}(r, \vartheta, \varphi) = -\frac{\mu_0}{4\pi} \sum_{n=0}^{\infty} \sum_{m=-n}^{+n} a_{nm} \frac{r^{n-1}}{\sin \vartheta} \frac{dY_{nm}(\vartheta, \varphi)}{d\varphi} \quad (\text{III.29})$$

Analogous to the two-dimensional problem discussed above, it is possible to expand the magnetic field in a combination of radial and spherical harmonic functions. For this expansion, each order  $n$  is a sum of  $2n+1$  functions with the corresponding number of expansion coefficients. If the expansion is limited to include orders up to a maximum order  $N$ , the total number of coefficients

### III.4. 3D spherical harmonics decomposition

is  $N^2 + 2N$ . This means that the requirement concerning the number of sensors is significantly more demanding than for the two-dimensional problem. To deduce the coefficients from magnetic field measurements as for the two-dimensional problem, it is again necessary to solve the inverse problem

$$\mathbb{A}\vec{x} = \vec{B} \quad (\text{III.30})$$

$$\mathbb{A}_{3D}(r, \vartheta, \varphi)\vec{x} = \vec{B} \quad (\text{III.31})$$

wherein, for the three-dimensional problem, the matrix  $\mathbb{A}_{3D}(r, \vartheta, \varphi)$  now has dimensions (number of measurement points · number of measurement axes), e.g.  $3N_S$  for a given number  $N_S$  of tri-axial sensors. The number of elements of the coefficient vector  $\vec{x}$  depends on the maximum decomposition order  $N$  and is equal to  $N^2 + 2N$ . As for the two-dimensional problem, if the number of available measurements  $\vec{B}_i$  is equal to the number of coefficients (i.e. it corresponds to the desired order of decomposition) and the sensors are well-distributed on a sphere, the inverse problem is well-defined. If there are more or less magnetic field values available than required for a given order (and number of coefficients), then the problem is over- or under-determined respectively. The matrix  $\mathbb{A}(r, \vartheta, \varphi)$  that describes the geometrical configuration of the measurement points with respect to the center of decomposition therefore assumes the following form:

$$\mathbb{A}_{3D}(r, \vartheta_i, \varphi_i) = -\frac{\mu_0}{4\pi} \left( \begin{array}{cccccccc} \overbrace{\sin \varphi_1 \sin(\vartheta_1)} & \overbrace{-\cos(\vartheta_1) \sin(\varphi_1)} & \overbrace{-\sin \vartheta_1} & \dots & \dots & \overbrace{Nr_1^{N-1} Y_{N,-N}(\vartheta_1, \varphi_1)} & \dots & \overbrace{Nr_1^{N-1} Y_{N,+N}(\vartheta_1, \varphi_1)} \\ \overbrace{\cos(\vartheta_1)} & \overbrace{-\sin(\vartheta_1)} & \overbrace{0} & \dots & \dots & \overbrace{r_1^{N-1} \frac{dY_{N,-N}(\vartheta_1, \varphi_1)}{d\vartheta_1}} & \dots & \overbrace{r_1^{N-1} \frac{dY_{N,+N}(\vartheta_1, \varphi_1)}{d\vartheta_1}} \\ \overbrace{-\cos(\varphi_1) \sin \vartheta_1} & \overbrace{-\cos \varphi_1 \cos \vartheta_1} & \overbrace{\sin \varphi_1} & \dots & \dots & \overbrace{\frac{r_1^{N-1}}{\sin \vartheta_1} \frac{dY_{N,-N}(\vartheta_1, \varphi_1)}{d\varphi_1}} & \dots & \overbrace{\frac{r_1^{N-1}}{\sin \vartheta_1} \frac{dY_{N,+N}(\vartheta_1, \varphi_1)}{d\varphi_1}} \\ \vdots & \text{1st order, 1st sensor} & \vdots & \ddots & \vdots & \vdots & \vdots & \vdots \\ \vdots & \vdots & \vdots & \ddots & \vdots & \vdots & \vdots & \vdots \\ \sin \varphi_{N_S} \sin(\vartheta_{N_S}) & -\cos(\vartheta_{N_S}) \sin(\varphi_{N_S}) & -\sin \vartheta_{N_S} & \dots & \dots & Nr_{N_S}^{N-1} Y_{N,-N}(\vartheta_{N_S}, \varphi_{N_S}) & \dots & Nr_{N_S}^{N-1} Y_{N,+N}(\vartheta_{N_S}, \varphi_{N_S}) \\ \cos(\vartheta_{N_S}) & -\sin(\vartheta_{N_S}) & 0 & \dots & \dots & r_{N_S}^{N-1} \frac{dY_{N,-N}(\vartheta_{N_S}, \varphi_{N_S})}{d\vartheta} & \dots & r_{N_S}^{N-1} \frac{dY_{N,+N}(\vartheta_{N_S}, \varphi_{N_S})}{d\vartheta_{N_S}} \\ -\cos(\varphi_{N_S}) \sin \vartheta_{N_S} & -\cos \varphi_{N_S} \cos \vartheta_{N_S} & \sin \varphi_{N_S} & \dots & \dots & \frac{r_{N_S}^{N-1}}{\sin \vartheta_{N_S}} \frac{dY_{N,-N}(\vartheta_{N_S}, \varphi_{N_S})}{d\varphi_{N_S}} & \dots & \frac{r_{N_S}^{N-1}}{\sin \vartheta_{N_S}} \frac{dY_{N,+N}(\vartheta_{N_S}, \varphi_{N_S})}{d\varphi_{N_S}} \end{array} \right) \Bigg\} 3N_S$$

As for the two-dimensional case, the requirements for a successful application of the spatial harmonics decomposition are:

- The development coefficients  $a_{n,m}$  must exhibit a defined dependence on the current of interest, i.e.  $a_{n,m} = f(I)$ , so that their determination allows a derivation of the current magnitude.
- $a_{n,m} \propto B_i/d_i^n$  behaviour for decomposition orders  $n$ , i.e. distant conductors have a reduced impact on higher orders

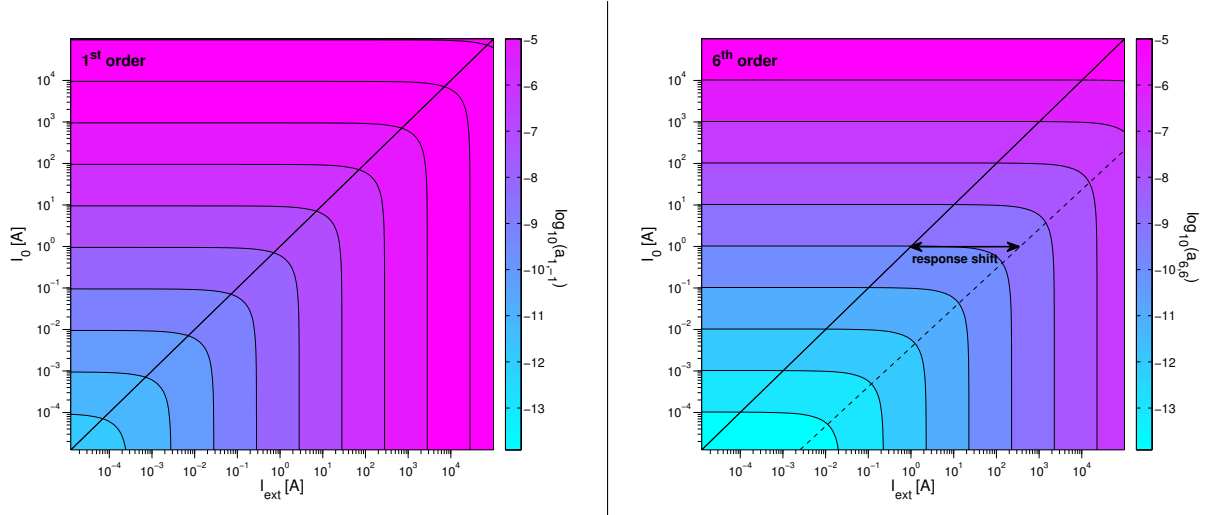


**Figure III.17:** Contour plot of coefficient values for a range of values of  $I_0$  and  $I_1 (= I_{ext})$  (logarithmic scale); left:  $a_{1,-1}$  right:  $a_{6,6}$ ; sphere radius  $r = 4$  cm, decomposition order  $N = 6$ , for 360 triaxial measurement points on the sphere.

- higher orders have significant signature/contribution on/to the magnetic field structure

For the simulation of the measurement conditions and to test the application of the spatial harmonics decomposition, a two-conductor system as shown in Fig. III.1 is employed for the 3D cases. The sensor array is placed close to one conductor and at a maximum distance to the distant conductor. The field measurements ( $B$ ) are simulated at various sensor positions and used in conjunction with the geometrical parameters (included in matrix  $\mathbb{A}$ ) to determine the vector of decomposition values from the inverse problem (Eq. III.31). To confirm the first two requirements given in the list above, a single conductor is initially examined without external perturbations, in order to obtain the relationship  $a_{n,m} = f(I)$ . Their fulfilment, which is the basis for a successful application of the spatial harmonics decomposition, was confirmed by the simulation studies. The coefficients exhibit a distinct, i.e. linear, correlation to the current values and the impact of distant conductors is in fact reduced for higher order coefficients, as shown, for a first and a sixth order (for increased visibility of the shift) coefficient, in Fig. III.17.

While the first two requirements present fundamental criteria that are provided by the theoretical framework and which have been confirmed by simulation, the third requirement only depends on the geometrical parameters of the sensor array and its position with respect to the conductor(s). As for the 2D case, the fulfilment of this last criterion must be ensured by careful definition of the geometrical parameters within the constraints imposed by the installation conditions and/or

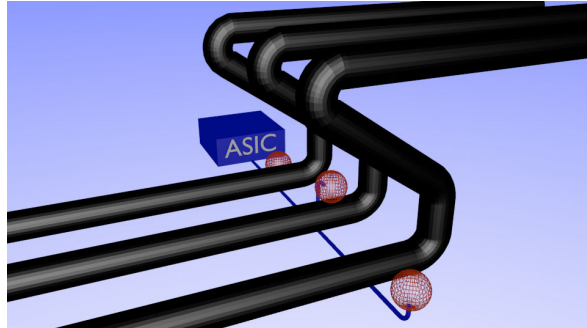


**Figure III.18:** Exemplary conductor path for 3D model simulation study. In contrast to the 2D model, the use of spherical harmonic functions and a 3D decomposition can be applied to arbitrary conductor paths, e.g. linear conductor path (left) or an example of a deformed conductor paths that can be found at specific points in the grid (right).

the array fabrication process (including minimum sensor head dimensions). Analogous to the 2D case above, these dimensioning aspects will be presented for the 3D application and will be followed by an analysis of potential errors sources in section III.4.3. For the discussion of the various parameters, it is necessary to consider the broader application scope of the 3D model, which is also suitable for non-linear cable path. This aspect will be discussed below, before the parametric analysis.

#### III.4.1 Linear and non-linear conductors

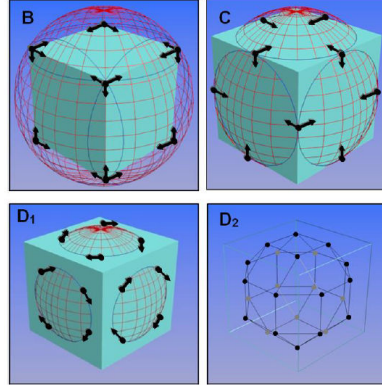
As detailed in the first part of this chapter, the decomposition of the magnetic field in 2D spatial harmonics imposes the fundamental constraint that it can only be applied to 2D fields and thus, in the scope of electrical cables, to conductors that run along a straight path. With the 3D formulations developed above, it is now possible to apply the decomposition in spatial harmonics to any field distribution and thus any conductor path. The application of the three-dimensional model is thus tested for two exemplary conductor paths, the linear conductor path that is also suitable for the 2D model (and common for aerial power lines) and a strongly deformed conductor path, which applies e.g. to power accessories and for which the application of the 2D model would fail. A Z-shaped conductor form is selected and examined as way of example for deformed conductor paths. For the sake of simulation, the cables are assumed to arrive from and extend to  $\pm\infty$ . The two conductor paths are displayed in Fig. III.18. Deformed conductor paths result in more complex distributions of the magnetic field than the radial structure of straight conductors (Fig. III.4). These enhanced spatial variations of the field can be beneficial for a study of spatial harmonics of

	relative magnitude $\left[ \frac{\sum_{m=-n}^{+n} a_{nm} r^n}{\left[ \frac{1}{-1} a_{1m} r \right]} \right]$			
	linear conductor	Z-shaped conductor		
		min	mean	max
1 <sup>st</sup> order	1			
2 <sup>nd</sup> order	0.33	0.01	0.29	0.48
3 <sup>rd</sup> order	0.16	0.01	0.16	0.38
4 <sup>th</sup> order	0.08	< 0.01	0.08	0.28
5 <sup>th</sup> order	0.04	< 0.01	0.05	0.22

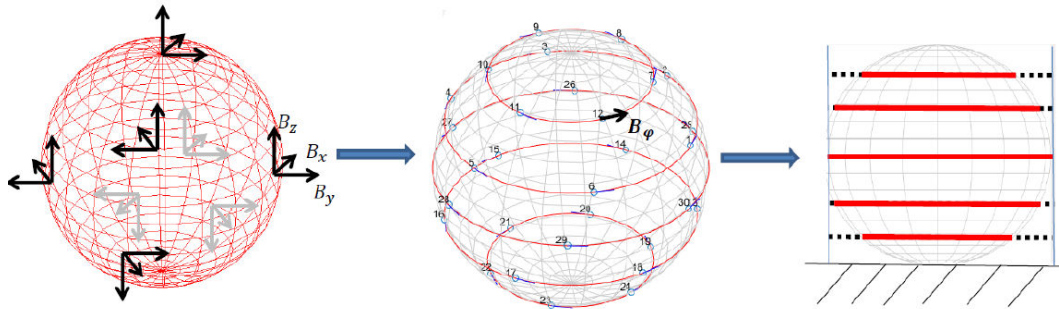
**Table III.3:** Relative magnitude of higher order contributions to the reconstruction of the magnetic field, with respect to the magnitude of the first order. The simulation is performed for an array of 100 triaxial sensors on a sphere of radius  $r = 4.5$  cm (using the 'sphere' distribution, see below) and a decomposition up to the 8<sup>th</sup> order. The array is located at  $d_0 = 0.08$  m above the conductor. For the Z-shaped conductor, the statistical values result from a shift of the decomposition center along a path above the conductor.

higher orders, since the coefficient values and thus the relative magnitude are no longer constant along the conductor path (resolution of the radial symmetry). To demonstrate this, the coefficients are determined by simulation for an over-determined problem, including eight orders in the decomposition ( $N_S = 100$  sensors well-distributed on a sphere of radius  $r = 4.5$  cm, maximum decomposition order  $N = 8$ ), and with the array located  $d_0 = 8$  cm above the linear conductor (a single position), and at various positions along a path that lies at the same distance above the deformed conductor. The simulation results for the first five orders are summarized in table III.3, which indicates that for the positioning along the deformed conductor paths, there are positions that provide an enhanced relative contribution of a specific higher order in comparison to the case of a linear conductor. There are also positions with unfavourable conditions for the detection of higher order contributions, but the positioning can be adapted to avoid these. In general, it can be concluded that a deformed conductor path offers the opportunity for an increased detectability of higher orders if the position dependence is exploited. This fact also opens the potential for an intentional manipulation of the conductor path or cross-section which will be discussed as a future perspective in the outlook of this work. For such applications, it should be kept in mind that in locations where the spatial distribution of the field includes stronger contributions from higher orders, it may be necessary to increase the number of orders and/or measurements to maintain the same reconstruction quality/accuracy.

### III.4. 3D spherical harmonics decomposition



(a) Solutions that allow for fabrication of an array based on a cube (e.g. of PCBs). The sensors can be placed on the vertices of a cube inscribed in a circle (configuration **B**), the edges (**C**) or faces (**D1** and **D2**) of a cube with smaller side length (intersection of sphere and cube present circles). Configuration **D2** presents the special case of a rhombicuboctahedron, which provides a good distribution of the points across the sphere.



(b) From left to right: For simulations, tri-axial sensors can be placed without constraints so that the problem is reduced to finding algorithms of optimal distributions. For practical implementations the sensors can be placed on a given number of discs. Here the cross-sections of the sphere are distributed symmetrically around a central cross-section which has the same radius as the sphere. Tangential placement of the sensor heads on the circle defined by each cross-section provides measurement of  $\vec{B}_\varphi$  directly.

**Figure III.19:** Various test configurations for practical implementations involving the placement of a given number of sensors (measurement points) on a sphere.

#### III.4.2 Sensor distribution

Similar to the influence of the number of field measurements used for the determination of the development coefficients via the inverse problem, the distribution of the sensors plays a pivotal

role in the reconstruction quality of the magnetic field. In two dimensions, the development area is circular and the placement of the sensors is intuitive. An equidistant distribution of the sensors along the circle proved to be the optimal solution, so that the selection of a practical solution can be reduced to the determination of the necessary number of sensors. In three dimensions and for the placement of the sensors on a sphere, the question of optimal sensor distribution is more complex. This is underlined by the fact that the task of optimally distributing points across a sphere (equal-area distributions) is a topic of active discussion in multiple fields<sup>[42,43]</sup>.

It should also be noted that the sensor distribution on the sphere is initially considered independent of the magnetic field, so that the developed sensor provides a robust solution for different spatial field distributions (i.e. different conductor paths). However, it is conceivable that for a given conductor path and sensor array position, the spatial variation of the field is particularly enhanced in a defined segment of the sphere and that the accumulation of sensors (spatially increased sensor density) in this area improves the reconstruction quality of the approach. This would present a highly customized version that would allow for little flexibility/adaptability to other application cases, which is not desired in this work.

Furthermore, while an optimal distribution of points on a sphere is desirable for theoretical considerations and simulations (and was employed for the simulations presented in this chapter), the (precise) placement of sensors on a sphere is difficult to implement in practical solutions. Not only do the sensor heads need to be positioned on a sphere, but the full sensor (including the electronics, predominantly placed on a printed circuit board (PCB)) must also be accommodated. In search of feasible designs for a 3D sensor array, the focus was initially placed on polyhedra inscribed in a sphere, so that the vertices present points on the sphere, or larger than the sphere, so that the dissection of the polyhedron and the sphere forms circles on the faces of the polyhedron. The simplest structure would be a cube inscribed in a sphere. Depending on the relative size of the cube, the vertices (side length  $a = \frac{2 \times \text{radius}}{\sqrt{3}}$ ) or edges (side length  $a = \text{radius} \times \sqrt{2}$ ) present points on the sphere, or the intersection of the cube and sphere creates circles on each face of the cube on which the sensors can be placed ( $2 \times r < a < \text{radius} \times \sqrt{2}$ ). More complex solutions include other polyhedra that provide well-distributed intersection points with the sphere.

Archimedean solids composed of regular polygons that meet in identical vertices prove particularly interesting, since their vertices are equidistant from one another. The rhombicuboctahedron is composed of 18 identical triangular faces and 8 identical square faces, which meet in 24 vertices. This sort of construction seems to be a limit for manufacturable solutions (at least for a reasonable price). Another promising solution is the placement of the sensors on parallel slices that dissect the sphere, with the sensitive elements of the sensor being placed tangentially on the intersection

circles. This configuration is advantageous since it presents a direct extension of the 2D configuration, with the adaptation that the slices are of varying radius depending on their relative position within the sphere.

Ensuing questions arise for the distribution on cross-sections (discs) of a sphere and concern the number of discs and their separation, the number of sensors on each disc as well as the relative angular offset between the individual discs. These questions are subject to practical considerations that will be detailed in the following chapter. From the theoretical standpoint, it can be noted that an optimal solution would use a decreasing number of sensors per disc for polar angles approaching the poles of the sphere, in order to approximate an equidistant distribution of the sensors. Furthermore, the distribution is ideally symmetrical for the upper and lower hemispheres, while the angular offset of a specific disc should also be chosen to avoid measurements at the same azimuthal angles as the disc above or below. With respect to these considerations and the practical implications (sensor dimensions) detailed in the next chapter, the disc configurations that emerged as promising candidates consisted of one large central disc (with disc radius = sphere radius) flanked by pairs of smaller sized upper and lower discs (at  $\pm\vartheta$ ).

The number of measurement axes of the individual magnetic field sensors is also a central element of these considerations. The ideal solution would involve sensors providing tri-axial measurements that can be considered punctiform, since this would allow for the determination of the magnetic field along any set of three orthogonal vectors at each point. In consequence, the sensors could be distributed without further consideration of the angular orientation. On the contrary, the distribution of bi- or mono-axial sensors should take the formulation of the theoretical problem into account. As presented in the previous chapter and here above (Eqs. III.5, III.6 and III.29), the decomposition of the field in spatial harmonics is performed with respect to polar and spherical coordinates for the 2D and 3D problems respectively. If a transformation of the measurement at a given point to corresponding components of the magnetic field ( $\vec{B}_r$ ,  $\vec{B}_\vartheta$  and, for the 3D case,  $\vec{B}_\varphi$ ) is not possible (as for bi- and mono-axial sensors), it is therefore meaningful to privilege such configurations that allow for the direct determination of the relevant components of the magnetic field. On this basis, the positioning of sensors on cross-sections of the sphere proves superior to other solutions, for the case of mono-axial sensors, since the tangential placement along each cross-section directly returns the component  $\vec{B}_\varphi$  which can be input into the inverse problem to determine the coefficient values.

It proves meaningful to consider the possibilities provided by multi-axis sensors for which the positions of the axes do not coincide or for which these axes do not present an orthogonal set. As will be discussed in following chapter, the two prototypes that correspond to the 2D and 3D test

$N_S$	Coefficient of determination $R^2$			
	Sensor distribution			
	<i>sphere</i>	<i>circles on cube faces</i>	<i>five discs</i> $\frac{N_S}{5} \cdot [1 \ 1 \ 1 \ 1 \ 1]$	<i>five discs</i> $\frac{N_S}{30} \cdot [4 \ 7 \ 8 \ 7 \ 4]$
30	0.99	0.54	0.98	0.99
60	1.00	0.58	1.00	1.00

**Table III.4:** Reconstruction quality using different sensor distributions. The values present the coefficients of determination  $R^2$  for a comparison between the real magnetic field of a Z-shaped conductor and the field reconstructed using coefficients determined with the given sensor number ( $N_S$  mono-axial sensors) and configuration (distribution), a decomposition up to the fourth order and a distance  $d_0 = 12$  cm. In the case of using multiple discs for sensor placement, the sensor number can be adapted to achieve a better approximation of an equal-area distribution.

cases defined in this chapter, do in fact use sensors with two measurement axes, of which however only one is used. The primary reasons for this are size considerations, which e.g. prohibit the placement of both axes in plane of the magnetic field for the 2D prototype (without significantly increasing the array radius), and a limited number of DAQ channels. However, for future developments, it should be considered that it is in principle possible to adapt the formulation of the measurement problem (effectively the inversion problem) to include secondary or tertiary sensor axes that are displaced or misaligned with respect to a primary axis (or with respect to the desired values, if a shift/misalignment is identified after fabrication). In this case, the matrix  $\mathbb{A}$  would have to be adapted to include the misalignment angles  $\alpha_i, \beta_i$  (in 2D, third alignment angle  $\gamma_i$  in 3D) and position of each shifted sensor at point  $P_i$ . Through the inclusion of these additional parameters (between 1-3 in 2D and 1-4 in 3D for each specific sensor), any sensor can be included in the decomposition problem. As stated above, a tri-axial sensor for which the measurements are punctiform and the axes orthogonal remains the optimal solution since it reduces the number of parameters (and potential sources of error) to be included in the measurement problem and because it allows a coordinate transformation at will. Table III.4 presents a comparison of the sensor distributions that were considered for a prototype configuration and thus also for the definition of a test case (see below). The analysis is performed for a Z-shaped conductor and sensor numbers  $N_S = 30$  and 60 (the former value to represent the practical implementation described below, the latter for sake of comparison). Mono-axial sensors were also employed to emulate realistic measurement conditions (Ch. 4). One way to analyse the various configurations would be to use a measure of the distribution of points across the sphere. Here, a more intuitive measure, which provides a direct impression of the applicability of a specific configuration for the task at hand, is used to

#### III.4. 3D spherical harmonics decomposition

---

compare the configurations: for each configuration the decomposition is performed with the given parameters, and the field reconstructed using the determined coefficients ( $a_{n,m}$ ) is compared to the actual field for a large number of well-distributed points ( $< 500$ ) inside the decomposition volume (on a sphere with  $r_{\text{check}} = r/2$ ). The coefficient of determination  $R^2$  between these two fields provides a direct indication of the reconstruction quality for a given configuration.

For the given number of sensors the distribution of sensors across the sphere without constraints ('sphere distribution', based on an algorithm developed by *Rakhmanov et al.*<sup>[44]</sup>) provides a near-perfect reconstruction of the field. The distribution of the sensors along a circle on each face of a cube, wherein the circles present cross-sections of the same sphere, proves to be an excludable solution since the reconstruction of the field must be considered incomplete. The radius of the circles could still be optimized for a given conductor shape, but, for the cases studied here, this type of distribution was never competitive with the alternatives. In contrast, the disc configuration introduced above exhibits only a marginal degradation of reconstruction quality with respect to the unconstrained distribution, while providing the advantages for practical implementation detailed above. Furthermore, although an adapted number of sensors on each disc provides a better approximation of a equal-area distribution across the sphere, the equinumerous distribution of sensors per disc also presents a workable solution of comparable quality, thus extending the range of possible implementations (more details are provided in chapter 4). After the general discussion of the effect of the conductor path and the sensor distribution on the decomposition problem, it is now possible to proceed with the parametric analysis for the 3D model for the decomposition of the magnetic field in spatial harmonics. This is accomplished by analysing the effects of the various parameters, while successively increasing the degree of specification of the simulation/test case in a practically and scientifically justifiable manner.

#### III.4.3 Parametric analysis - dimensioning and error sources

The objective of dimensioning the measurement volume and relative position (with respect to the field source(s)) is again to determine: (a) up to which order the decomposition must be performed for a given source configuration (range for  $d_1/d_0$ ) and (b) the required size for the decomposition volume (i.e. the radius for a sphere) that allows for the detection of the desired order. Here, the problem is again solved for a system of two (linear) conductors. The order required to determine the current value with a precision of  $\Delta I_0 \leq 0.5\%$  can be deduced from Fig. III.20 for a given ratio  $d_1/d_0$ . For this analysis an array of  $N_S = 100$  tri-axial sensors are used to determine the field up to the order  $N = 10$  and the array is positioned at  $d_0 = 6$  cm, while the perturber  $I_1 =$

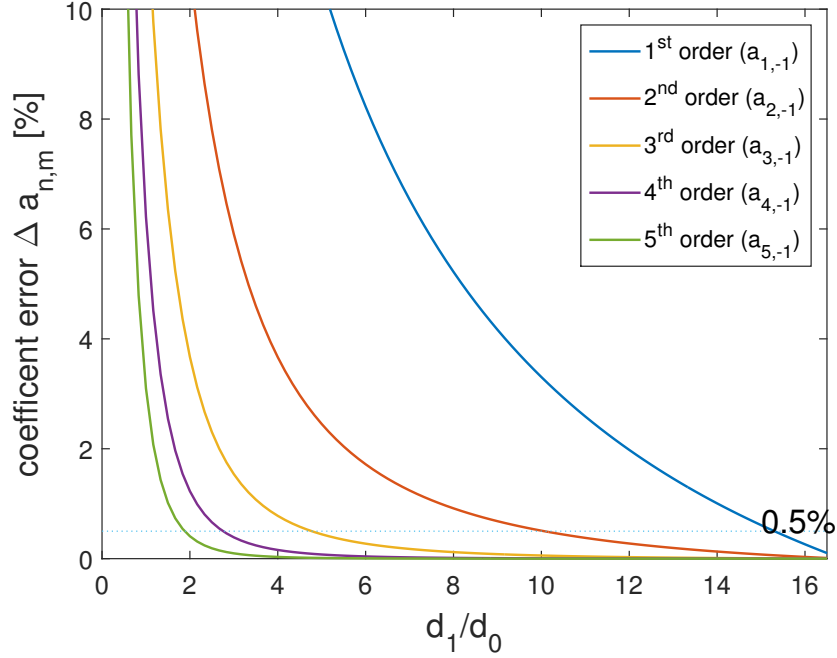


**Figure III.20:** Error in coefficient values for the strongest contributions of each order  $a_{n,-1}$ , for the decomposition of a two-conductor system with  $I_0 = I_1$  using a sensor array of  $N_S = 100$  tri-axial sensors and a maximum decomposition order of  $N = 10$ . The array is located at  $d_0 = 6$  cm, while the perturbing conductor is displaced along the line that intersects the conductors and the center of the array.

$I_0$  is displaced along the line that intersects all three components. The analysis shows that for typical application cases in the electrical grid (where  $d_1/d_0 > 3$ ), can again be employed to achieve the desired precision. The knowledge of the required decomposition error already allows the determination of the minimum number of field measurements that must be performed to identify the coefficient values from the inverse problem, which is  $N^2 + 2N = 24$  for the 3D application. The second required condition concerns the detectability of the this component.

As is evident from Eq. III.29, the relative magnitude, and thus the detectability of higher order contributions to the decomposition/reconstruction of the magnetic field depends, as for the 2D case, on the ratio  $r/d_0$ . For example, the effect of varying the array radius is shown in Fig. III.21 which confirms that, for a fixed array/decomposition center, the array size should be comparable to the dimensions of the conductor (with insulation), in order for higher orders to be of detectable magnitude. The number of orders required to achieve a certain quality of reconstruction depends on the center of decomposition and the array size. It is thus necessary to find a compromise be-

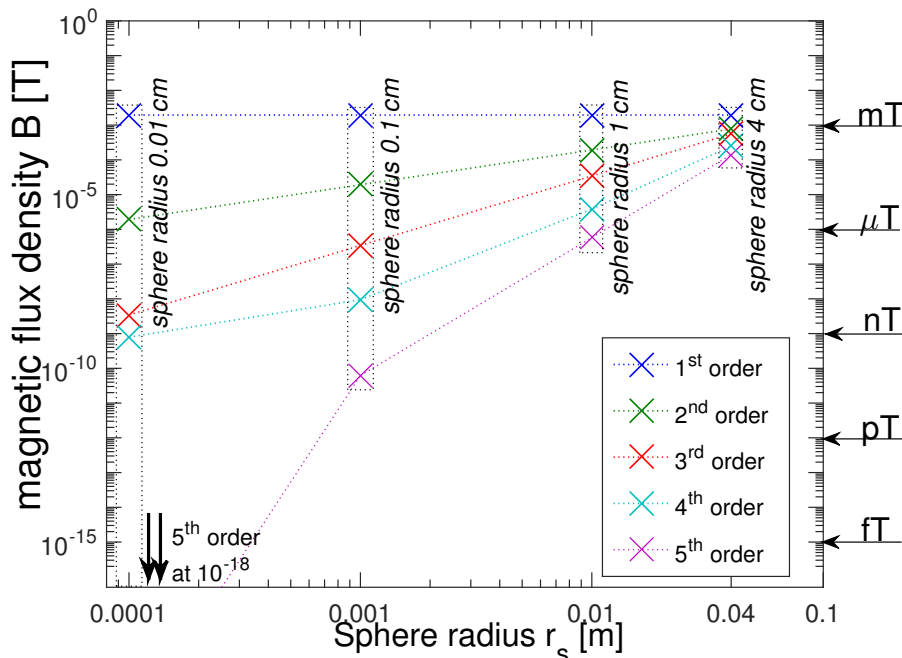


**Figure III.21:** Magnitude of decomposition orders by radius  $r$ . Maximum decomposition order  $N = 6$ , 60 triaxial sensors on sphere,  $I_0 = 1000$  A in a Z-shaped conductor and no perturbation. The center of the spherical sensor array is positioned at  $d_0 = 8$  cm besides the conductor.

tween the desired maximum miniaturisation of the array and the detectability of high orders for a high-precision measurement. The behaviour is given by Eq. III.29 and confirmed by simulation, the results of which are provided in Fig. III.22. As for the 2D case, it can be concluded that the sensor array must be of comparable dimensions as the array-to-conductor distance  $d_0$ . Since the distribution and placement of sensors is more complex for the 3D case (placement on a sphere), practical considerations also play a more significant role in the definition of an array radius. The practical aspects are discussed in detail in the following chapter. In combination with these practical implications, the simulation results resulted in the definition of a sphere radius of  $r = 4.5$  cm.

Once a suitable array radius, number of sensors and sensor distribution have been defined, it is possible to study the effect of potential errors sources on the measurement accuracy. This analysis is provided in the following.

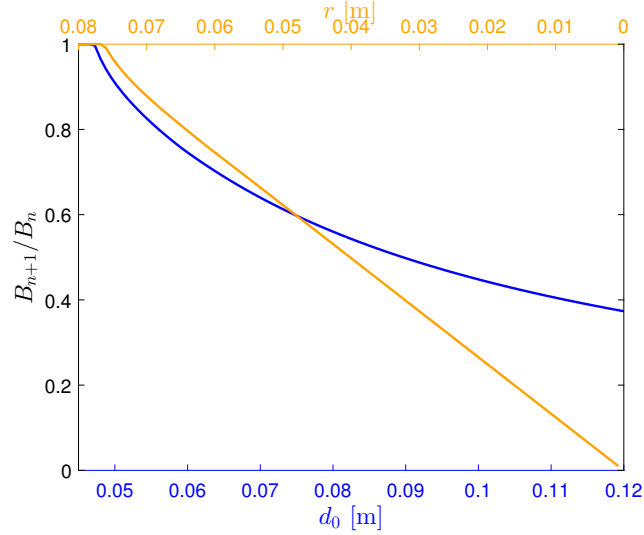


**Figure III.22:** Relative magnitude of decomposition orders with respect to the next lower order and in dependence on the array radius  $r$  (upper scale, with  $d_0$  fixed at 8 cm) and on the array-to-conductor distance (lower scale, with  $r = 4.5$  cm). Simulation for a single straight conductor, 100 triaxial sensors, a decomposition up to the order  $N = 8$  and at  $I_0 = 10$  A.

### Test case for laboratory conditions

The definition of a test case for simulations that corresponds well with the eventual experimental conditions is based on a conclusion that will be presented in more detail in the following chapter: since no suitable three-axial sensor solutions were available amongst commercial products, only mono- and bi-axial solutions could be considered. In this case, as detailed above, the distribution of the sensors equidistantly along cross-sections of the sphere provide the optimal solution since they allow for direct measurements of  $\vec{B}_\varphi$ . The first step toward the definition of suitable dimensions for a laboratory case (and thus the simulation test case) is again the conclusion from Fig III.20, that for typical laboratory dimensions, i.e.  $d_0$  equal to several centimetres and  $d_1$  a few tens of centimetres, the decomposition should be performed up to the fourth order. This again enforces implications for the number of sensors/measurements ( $N_S \geq 24$ ) and the array radius, which must allow for the determination of the fourth order. In order to be able to perform current determinations with a varying number of sensors and different subsets of sensors, the array includes 30 sensors allowing for the same number of measurements of  $\vec{B}_\varphi$ , thus resulting in an over-determined inverse problem if more than 24 measurements are employed. The sensors are placed on five discs and are effectively distributed across a sphere of radius  $r = 4.5$  cm. Given the sensor dimensions

### III.4. 3D spherical harmonics decomposition

---

(see Ch. 4), the central disc of identical radius thus allows for a placement of 6 sensors. Five discs are used in total, with corresponding disc pairs at  $\pm 1.5$  cm and  $\pm 3.0$  cm above/below the central disc. Since the setup parameters are independent of the array, they are the same as for the 2D case, with the sole difference being the fact that different angular positions of the 3D array can be advantageous for a particular conductor shape and should consequently be studied carefully. The parameters for the 3D test case are summarized below

**3D sensor array parameters:** sensors distributed on sphere with  $r = 4.5$  cm;  
 $N_S = 30$  on five discs with  $\varphi_i = j \cdot \frac{2\pi}{6}$  for  $j = 0, 1 \dots 5$   
 central disc  $r_0 = 4.50$  cm  
 discs at  $\pm 1.5$  cm  $r_{\pm 1} = 4.24$  cm;  $\varphi_{\pm 1} = \varphi_i \pm \frac{\pi}{6}$   
 discs at  $\pm 3.0$  cm  $r_{\pm 1} = 3.36$  cm;  $\varphi_{\pm 2} = \varphi_i \pm \frac{2\pi}{6}$

**Setup parameters:**  $d_0$  in the cm range,  $\varphi_0 = \pi$ ;  
 $x > d_0$ ,  $d_1 = \sqrt{x^2 + d_0^2}$ ,  $\varphi_1 = \frac{\pi}{2} + \tan^{-1}\left(\frac{d_0}{x}\right)$

As will be detailed in the following chapter, in particular the lower limit for the array radius is strongly dependent on the available sensor solution. In the case of the 3D laboratory prototypes, a feasible design was only possible if the sensors on the three interior discs could be placed on the plane of the disc. The sphere radius of  $r = 4.5$  cm was therefore a direct consequence of the sensor size, since it presents the smallest possible diameter that allows the placement the six sensors in a planar arrangement for the three interior discs. The possibilities for future prototypes are also discussed in Ch. IV. Here, the parameters resulting from the considerations of the theory and practical implementation, which are listed above, are employed for the simulation studies presented below.

#### Error sources

For the analysis of potential error sources, it proves meaningful to differentiate between the 'array parameters' included in the geometry matrix  $\mathbb{A}$  and potential rotation offsets of the field measurement axes, just as the for the 2D case.

#### Intrinsic array parameters and array position

Errors can result from imprecisions in the fabrication process and in this case, the values assumed in the calculation of the matrix  $\mathbb{A}(r_i, \vartheta_i, \varphi_i)$  do not correspond to the actual values of these pa-

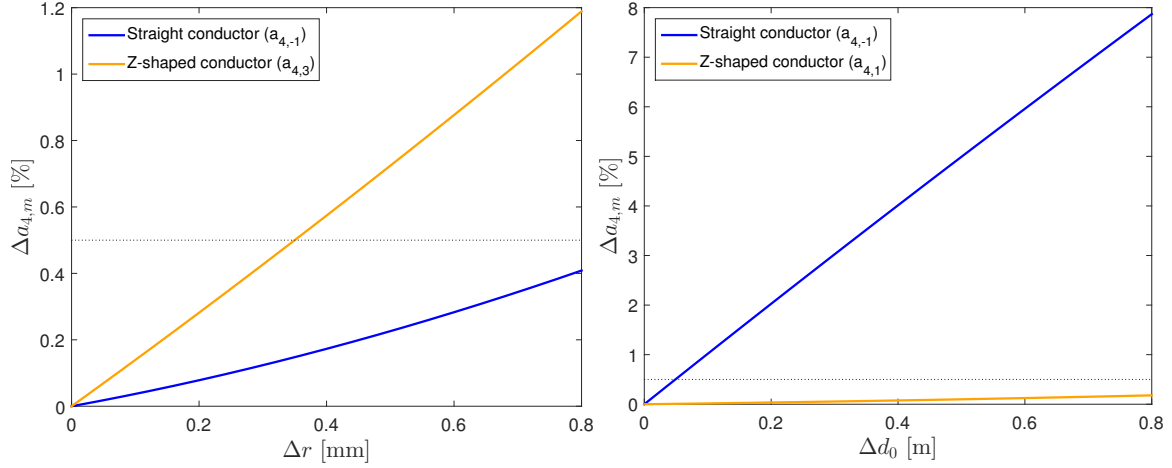


**Figure III.23:** Error in a fourth order coefficients for 'fabrication errors' up to 2 mm in the array radius  $r$  and 'placement' errors in  $d_0$ . The simulations are performed with a reference radius of  $r = 4.5$  cm, a reference distance  $d_0 = 6$  cm and for both conductor paths.

rameters. The effect of a collective error in the array radius  $r$  and the effect of a positioning error  $\Delta d_0$ , is presented in Fig. III.23. For these first sets of potential error sources, the simulations are performed for both kinds of conductor paths, in order to give the reader a feel for the different implications of the two paths. For the linear conductor path, the array is always placed above the conductor of interest. For the Z-shaped conductor path, the results depend strongly on the position of the array, since the local field gradients are stronger. For the radius variation, the array (test case parameters), is placed above the within the lower bend of the Z-shaped conductor, while it is positioned outside the lower bend for the Z-shaped conductor for the analysis of the variation in  $d_0$ . These positions are the result of a coarse comparison of results obtained along the conductor path. For either conductor path, the variation in the largest fourth order coefficient is displayed.

For different conductor paths, different coefficients assume the dominating role in the fourth order contribution. At the given position, the error  $\Delta d_0$  is very small for position variations. However, due to the large spatial variation of the field, these results cannot be taken as an absolute reference, but, it has become evident that the determination of an optimal sensor location will be a central point of applications for non-linear conductor paths. The large error that results for the fourth order coefficient due to position variations can be significantly reduced by finding an optimal rotational orientation of the sensor array. For the simulations performed here, the five discs with the 30 sensors were always aligned perpendicular to that of the 2D array.

A better solution for the application of the 3D sensor array with a straight conductor would

be to emulate 5 discs parallel to the circle of the 2D array, in order to measure maximum field strengths and to reduce the susceptibility to error sources. For systematic errors in the array radius, it is possible to conclude (for this test case) that the fabrication error should be below 0.4 mm for the Z-shaped and below 0.9 mm for the straight conductor, or should be determined and corrected to that degree after fabrication, in order to respect the requested 0.5% accuracy.

The different measurement conditions with either conductor path can be investigated further by studying the coefficient spectrum obtained for the same array (test case) above a straight conductor and at the same location but with the conductor rising in the vicinity to follow the Z-shaped conductor path. The results for this setup are provided in Fig. III.24, where the coefficients  $[a_{n,m}]$  are multiplied by  $r^n$ , in order to obtain terms that are proportional to the field contributions of the specific order. The 24 coefficients up to and including the fourth order are displayed. For the straight conductor, it can be observed that the component  $a_{n,-1}$  either provides the largest contribution to a specific order, or is amongst the largest contributors (for the fourth order). The distribution of coefficient magnitude is more diverse for the deformed conductor path, which can both be an advantage due to a more distinct signature of the source, but can also reduce the detectability of higher order coefficients, if the contribution of that order is spread across several terms.

The further analysis focuses on the Z-shaped conductor path, as an example of a deformed conductor path, for which the 3D array was conceived. Current measurements in straight conductors can be measured using the 2D array. As discussed above, the results obtained for the Z-shaped conductor depend strongly on the relative position of the sensor array. For the analysis of the effect of variations in intrinsic array parameters, the array of radius  $r = 4.5$  cm is placed centrally above the bottom part of the conductor and near the first bend ( $90^\circ$  upwards) of the conductor. The results confirm once again, that the higher orders, with the weaker relative magnitudes, are impacted the strongest by variations in array parameters. Due to the strong variations with array position, the implications will be summarized below for the given simulation parameters, instead of providing graphs for individual parameters as for the 2D case, in order to avoid the impression that the results are generally applicable. Systematic and random errors in the radial and angular positioning precision of each individual sensor, i.e. for possible errors in the coordinates of the sensor locations  $r_i, \vartheta_i, \phi_i$ , yield the following results for the given position, surrounded by the Z-shaped conductor:

- the distribution of random errors in sensor radii should not surpass 0.6 mm, in order to limit the error in the fourth order coefficient to below 0.5%. This constraint is comparable to the results obtained for the 2D array.

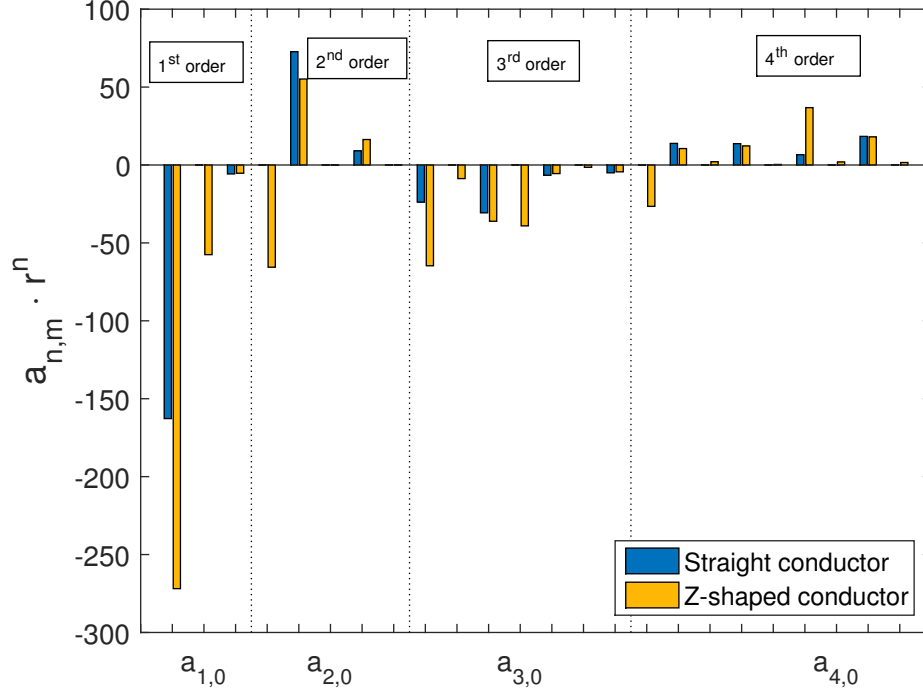


**Figure III.24:** Coefficient spectrum for different conductor types. Uses array composed of five disks, with a total number of 30 sensors on a sphere of radius  $r = 4.5$  cm. The spectrum is determined above a straight conductor and at the same position but with the Z-conductor rising vertically at 5 cm from the array center.

- random errors in angular positions should be limited to  $< 1.2^\circ$  for  $\vartheta_i$  and  $\varphi_i$ , and will sum up if both angles vary within the same range.
- the margins of error for systematic angular position offsets should not exceed  $\Delta\vartheta = 2.3^\circ$  and  $\Delta\varphi = 1.7^\circ$ . The errors are comparable for the different orders and the (largest) first and second order coefficients even exhibit a slightly larger offset than the higher orders. This behaviour is again strongly dependent on the position of the array with respect to the conductor. If both angular variables are simultaneously subject to systematic errors, the coefficient errors are substantially stronger and exceed 0.5% close to  $2.3^\circ$ . These would therefore need to be corrected (e.g. after fabrication), or a new transfer factor determination/calibration would have to be performed. For a given conductor path, the search for an optimal placement conditions (within any given constraints on the placement) already offers the potential for a increased robustness to systematic errors in angular positions.

The systematic and random errors are generally of comparable order with respect to the depen-

dencies observed for the 2D prototypes. The main difference lies in the increased heterogeneity of the magnetic field, which leads to a large spatial variation of the obtained results. Nevertheless, the example of the Z-shaped conductor shower, that there are indeed advantageous positions that can be exploited for current measurements and which may even have enhanced higher order contributions.

Besides variations in angular and radial positions, sensor misalignment again presents a source of error for the measurement principle and will be studied in the following.

#### **Sensor misalignment**

As for the 2D case, it is also necessary to study the effect of potential sensor axis misalignments on the measurement accuracy. In the test case, the sensors are oriented to measure along  $\vec{e}_\varphi$ . Possible misalignments are therefor possible within the cone defined by rotation around  $\vec{e}_r$  ( $\pm\alpha$ ) and  $\vec{e}_\vartheta$  ( $\pm\beta$ ). Under the given conditions, the former resulted in fourth order coefficient above 0.5% for misalignments  $\alpha > 2^\circ$ . Misalignments  $\beta$ , already reach the same level of fourth order coefficient error at  $1^\circ$ , are thus the dominant source of misalignment error and also dominate the error when the two misalignments are observed simultaneously with comparable magnitude.

Given the disc configuration and assuming that these are fixed rigidly to one another, it is also possible to assume that rotations will only be possible around the axis in the plane of the disk and orthogonal to the measurement axis and/or around the vertical axis at the point. Misalignments with respect to these axis yield comparable result, again with the observation that the robustness of the method is dependent on the relative position of the array.

This last point of the parametric analysis concludes the description and analysis of the 3D measurement principle. As discussed, the fact that no analytical formula for the coefficient values exists for the 3D case makes the examination of errors sources more complex and primarily reliant on simulation. Furthermore, the strong spatial variations of the magnetic field created by a deformed conductor path, e.g. such as the Z-like conductor form, make it difficult to draw conclusions from the parametric analysis that provide a level of generalizability. Some values for a specific test case and array position were provided for orientational purposes above. The results however stress the importance of an optimisation procedure for a given conductor form. Deformed conductor forms will provide favourable and less favourable conditions for robust and repeatable measurements. Installation constraints may however limit the volume available for array installation. The analysis proved that this positioning problem should be studied carefully and does not have an obvious solution as for the 2D case.

Besides the assessment of potential error sources, the considerations presented above provide the basis for a dimensioning of a suitable measurement sphere and the well-adapted positioning/distribution of sensors (of a given technology) in a corresponding array, thus allowing for the identification of the coefficient values which are the key to precise current determination in a perturbed environment. The susceptibility to the most critical error sources was also analysed and can serve as a toolbox for fault analysis or as precision standard for fabrication processes. Before the proposed measurement principle is put to the test, the last missing element of the application of the (internal) spatial harmonics decomposition to current measurement is provided with the discussion of AC measurement algorithms in the following.

### III.5 AC measurement methods

The measurement principle for 2D and 3D fields was presented above for the determination of a given current value  $I_0$  and given perturbing currents  $I_1$  and  $I_2$ . These considerations can be applied directly to DC measurements. For AC measurements the conclusions drawn above remain applicable but evaluation algorithms must be slightly adapted and the two possible implementations are presented below. The typical application case for measurements in the electrical grid implies a phase offset of  $\frac{2\pi}{3} = 120^\circ$  or  $\frac{4\pi}{3} = 240^\circ$  between the individual phases respectively.

#### III.5.1 Pointwise evaluation

The pointwise evaluation algorithm is a direct extension of the DC evaluation method, i.e. the inverse problem  $\vec{x} = \mathbb{A}^{-1}\vec{B}$  is solved for every measurement point (every vector of field measurements at the various locations acquired (quasi) simultaneously). The result is a coefficient vector  $\vec{x}(t)$  for each measurement point, wherein the number of points per period only depends on the sampling frequency ( $f_{\text{samp}}$ ):

$$\vec{x}(t) = \mathbb{A}^{-1}\vec{B}(t) \quad \forall \quad t = t_0 + 1/f_{\text{samp}} \quad (\text{III.32})$$

The resulting coefficients can then be multiplied by the pre-determined transfer factors  $k_{x_{n'}} = \frac{x_{n'}}{I_0}$  (for a coefficient value  $x_{n'}$ , i.e.  $a_n$  or  $b_n$  for the 2D problem or  $a_{n,m}$  for the 3D problem). This allows a reconstruction of the current  $I_0(x_n)$  for each individual order, wherein the higher order calculation will again exhibit a reduced or even negligible effect of perturbing sources (depending on the exact array configuration and measurement conditions). This evaluation method therefore provides the advantage of allowing for a pointwise current reconstruction which can be meaningful

for the detection of faults and the determination of their origin (e.g. nearby or distant conductor).

#### III.5.2 Fast Fourier Transform of field measurements

An evaluation method that can be applied once multiple periods of the AC signal have been acquired is a Fast Fourier Transform (FFT). This can be applied to the signals  $B_i(t)$ , in order to extract the relevant component at  $f_{\text{FFT}} = f(I_0)$ . The evaluation uses a Discrete Fourier transform (DFT) for a given number of samples  $N_{\text{samp}}$ :

$$FFT(k) = \sum_{t=0}^{N_{\text{samp}}-1} B_i(t) e^{-2\pi jtk/N_{\text{samp}}} \quad (\text{III.33})$$

where  $j$  is used to denote the imaginary unit. The advantage of this algorithm for the current determination is the discrimination between the signal of interest (i.e. at 50 Hz for current measurements on the grid) and signal components (e.g. the DC component or intrinsic sensor offsets). The application of the DFT to the sensor signals for a given period then yields measurement values that can be input into the inverse problem to obtain coefficient values that can again be converted to current values using the transfer factors. This evaluation method therefore provides limited temporal resolution since multiple periods must be input into the FFT and each application of the FFT results in a set of values for the current determined using the various orders, via the solution of the inverse problem:

$$\vec{x}_{\text{FFT}} = \mathbb{A}^{-1} \vec{B}_{\text{FFT}} \quad (\text{III.34})$$

## III.6 Conclusion

The above formulation for both the 2D and 3D models for a decomposition of the magnetic field in spatial harmonics thus provides the necessary geometrical selectivity for a current measurement in a multi-source environment. The simulations confirm the increased selectivity for higher orders. The subsequent analysis of potential error sources underlines the importance of precise fabrication standards and correction means for the application of the contactless current measurement method. After fabrication, the calibration method developed above allows for on-site and repeated calibration, and significantly increases the robustness of the method against variations of array position over time. The theoretical framework and parametric analysis then provides the basis for an adequate design and fabrication of laboratory prototypes for the application of the 2D and 3D models respectively. The main objective for the practical implementation of the theoretical models

is to determine the 'feasibility'. While the simulations can be carried out for a large number of (triaxial) field sensing positions and, accordingly, a decomposition up to a high order at the 'mere' cost of increased computation time, a practical solution must use a reasonable number of sensors of a commercially available technology as well as a suitable sensor arrangement to provide the field measurements for the determination of the coefficient values. The necessary development steps for the laboratory prototypes will be presented in the following chapter.



---

## Prototypes and laboratory setup

---

---

IV.1	Sensor technology for laboratory tests: Stefan Mayer fluxgate sensors . . . . .	96
IV.2	2D prototypes . . . . .	98
IV.3	3D prototype . . . . .	99
IV.4	Laboratory setup . . . . .	101
IV.5	Magnetic sensor characterization and offsets . . . . .	102

---

As indicated in Fig. II.1, the theoretical framework detailed in the last chapter provides the measurement principle that serves as a basis for current measurement applications. Depending on the conditions imposed by a specific measurement task/geometry, it is then necessary to select an appropriate sensor technology for the practical implementation of this measurement principle. The selection of a sensor technology and (commercially) available product is accompanied by design aspects that seek to merge the simulation results with the desired sensor performance, i.e. to simplify the sensor configuration (arrangement of the  $N$  required magnetic sensors) so that the fabrication effort and cost can be minimised. This chapter serves to present the considerations and choices made for the implementation of laboratory prototypes adapted to the 2D and 3D decomposition approach respectively and can be used as a reference for analogue considerations for future applications that involve different constraints. The selection of the magnetic field sensor technology will be presented first, followed by a description of the design aspects which may in large be adopted directly for other applications.

Before the magnetic sensor technology and the design of the 2D and 3D prototypes are described

below, it is meaningful to recall the influence of the following aspects on the spatial harmonics decomposition:

**Sensing area/ Number of magnetic sensor axes** Besides the measurement characteristics, such as precision and range, of the magnetic sensor technology, there are also two geometrical properties that are essential in determining the suitability of a specific sensor solution. On the one hand, since the measurement method relies on the spatial resolution of the magnetic field in the various orders of decomposition functions, the sensing elements should offer measurements that are as punctiform as possible. For the spatial harmonics distribution, each field measurement is input with its respective coordinates and if the field measurement cannot be considered punctiform, i.e. if the field is averaged over an area of considerable extent (in the extreme case this area may overlap with that of adjacent sensing elements), then the decomposition will fail. Furthermore, as stressed in the precedent chapter, the number of sensor axes is also a decisive criterion. It must, however, be kept in mind that the sensor axes must be aligned to measure components of the magnetic field that can be input directly into the formulation of the inverse problem presented above (in polar or spherical coordinates) or must be transformable into the relevant components. For three-axial sensors, this is theoretical possible but requires that the three axes have the same origin. The same conclusion applies to the use of secondary or tertiary axes for the correction of the measurement along the primary axes which is aligned to measure a desired component. In consequence, the use of bi- or tri-axial sensors is not necessarily advantageous to that of mono-axial sensors, especially if it ensues a significant increase in sensor dimensions.

**Sensor size and distribution** The second geometrical consideration concerns the overall dimensions of a magnetic sensor (e.g. sensing element with PCB and electronics). Since the measurement method involves the use of several sensing elements and/or individual sensors that must be placed on a circle or sphere of a certain radius, the sensor dimensions must allow for a placement of the sensing elements on these boundaries.

## IV.1 Sensor technology for laboratory tests: Stefan Mayer fluxgate sensors

To meet the requirements of the measurement task at hand, it is necessary to identify a sensor solution which is adapted to the field magnitudes in the immediate proximity of the conductor of interest (in order to optimise the ratio  $d_0 : d_1$ ) and which offers a precision and signal-to-noise

Supplier	Product	Technology	No. of axes	Range [ $\mu\text{T}$ ]	Precision	Noise (peak-peak)	Frequency range	Sensitivity [ $\text{mV}/\mu\text{T}$ ]	Size [sensing element]
Stefan Mayer Instruments	FLCX52-500	Fluxgate	2	$\pm 500$	$\pm 0.5\% \cdot  B_{\text{meas}}  + 5\mu\text{T}$	$< 5 \text{ nT}$ (0.1 to 10 Hz)	DC-1 kHz	10	$29 \times 16 \text{ mm}$ [ $L = 11 \text{ mm}$ ]
Honeywell	HMC1022	AMR	2	$\pm 600$	0.4%FS (for $\pm 300\mu\text{T}$ )	$\sim \mu\text{T}$	DC-5 MHz	$0.01/V_{in}$	$10 \times 6 \text{ mm}$ [ $< 5 \times 3 \text{ mm}$ ]
Aichi	MI-CB-1DL	MI	1	$\pm 300$	0.2%FS	200 nT (0.1 to 10 Hz)	DC-10 kHz	3	$31 \times 6 \text{ mm}$ [ $< 1 \times 1 \text{ mm}$ ]

**Table IV.1:** Commercial magnetic sensor technology for laboratory prototype.

ratio that allow for a sufficiently precise detection of higher order contributions to the magnetic field. Further relevant sensor parameters include the frequency range, sensitivity and the operating temperature range. To test the measurement principle under laboratory conditions, the search for a suitable magnetic sensor technology was thus focused on identifying commercially available magnetic field sensor solutions that have overall dimensions in the low centimetre range (or below), which are commonly classified as miniature sensors, and that meet the field range and precision requirements. Various sensor technologies were examined and two exemplary candidates are listed below along with their advantages and the reason for their exclusion.

- Honeywell AMR sensor:** belongs to a wide range of 1-, 2- or 3-axis magnetic field sensors based on the anisotropic magnetoresistive effect. This technology consists of four resistive elements, of which one is sensitive to magnetic fields, arranged in a Wheatstone bridge. The bridge output voltage is the image of the magnetic field. For example, the bi-axial Honeywell 1022 sensor offers the advantage of a very small size (overall dimensions:  $[10 \times 6] \text{ mm}$ , sensing element  $< [5 \times 3] \text{ mm}$ ). This offers the potential of 2- or 3-axis measurements that can be considered punctiform. The Honeywell AMR sensors also offer a favourable range ( $\pm 600 \mu\text{T}$ ) at an attractive price of  $< 10 \text{ €}$  per unit. However, the main disadvantage of this product lies in the low sensitivity  $0.1 \text{ mV}/\text{V}/\mu\text{T}$ , which requires the development of additional amplification stages and appropriate signal treatment. The sensor, therefore, cannot provide the necessary precision for the application. This conclusion is supported by the fact that AMR sensors with additional electronic components are sold/marketed by Honeywell for compassing applications.
- AICHI magnetoimpedance sensor:** these magnetic sensors, e.g. the single-axis MI-CB-1DL, employ very small sensing elements ( $< 1 \text{ mm}^2$ , overall dimensions:  $[31 \times 6] \text{ mm}$ ) and a good precision (0.2% FS). However, although they include additional electronic components, the AICHI MI sensors have a sensitivity ( $3 \text{ mV}/\mu\text{T}$ ) and a noise level (200 nT for 0.1 to 10 Hz) that would make the determination of contributions to higher orders to the

magnetic field extremely difficult, if not impossible. In addition to the noise problem, the use of the MI-CB-1DL is also hampered by their limited measurement range of  $\pm 300 \mu\text{T}$ .

Among the commercially available magnetic field sensing solutions, the miniature fluxgate series from Stefan Mayer Instruments were eventually identified as the most suitable magnetic sensors. After discussion with the manufacturer, it was possible to obtain a customized version with an extended range up to  $500 \mu\text{T}$ . The sensor characteristics are provided in Tab. IV.1. They cover a range of field magnitudes that allows for measurements up to 100 A in the laboratory (depending on the distance to the conductors) and provide precision and noise characteristics that allow for a determination of the fourth decomposition order when placed in an adapted configuration. As a consequence, the use of the FLCXS2-500 allows for an array radius in the low centimetre range. Sensors with stronger noise characteristics would require larger array radii, in order to increase the magnitude of the fourth order contribution. It is pointed out again that the selection process served to find the best commercially available solution for laboratory tests and the selection criteria were defined accordingly. In contrast, the selection of a sensor solution for industrial applications must also take other sensor parameters into account as essential selection criteria, e.g. power consumption (also in view of possibly autonomous sensors) or cost per unit (for mass fabrication), and may also weigh the criteria differently than in the selection process highlighted above. After the selection of a suitable sensor technology of dimensions that allow for placement of the magnetic sensors on a circle/sphere and with specific radii  $r$  in mind for each case respectively, it is possible to design the 2D and 3D prototypes which will be described in the following.

## IV.2 2D prototypes

As described in the previous chapter, the optimal sensor configuration for the measurement of a (predominantly) two-dimensional field is provided by an equidistant distribution of the magnetic sensors along a circle. For the detection of the spatial harmonic components up to the fourth order, which requires at least 8 measurements, 10 miniature fluxgate sensors from Stefan Mayer were placed on a decagonal support at angles  $\vartheta_i = i \cdot \frac{2\pi}{10}$  for  $i = 0, 1 \dots 9$ . A 2D laboratory prototype is displayed in Fig. IV.1. The measurement of the second axis of each sensor cannot be used for the solution of the decomposition problem, since the measurement along this axis is out of the plane of the magnetic field. The size of the individual sensors does not allow for a positioning of both axes in the measurement plane for a circle of radius  $r = 3.2 \text{ cm}$ . The fabrication of a single PCB with mono- or bi-axial sensors at each angular position  $\theta_i$  should be considered for future prototypes. The secondary axis could however be utilized to determine the orthogonality of the

sensor array with respect to the conductor (for a given current flow) or of the misalignment of a particular sensor. For such investigations, it is furthermore necessary to keep in mind that the two measurement axes of the FLCXS2-500 do not have the same origin, which may complicate a utilisation of the secondary axis for corrective measures during current measurements. The secondary axis may, however, be employed for alignment verification in uniform and static magnetic fields, provided that the two axes have limited misalignment between one another. The parameters of the 2D prototype are thus:

**2D sensor array parameters:**  $r = 3.2$  cm;  $N_S = 10$  at  $\vartheta_i = i \cdot \frac{2\pi}{10}$  for  $i = 0, 1 \dots 9$

Two identical prototypes have been fabricated in order to enable repeatability tests for the measurement procedure.

### IV.3 3D prototype

Initial considerations concerning the design and practical implementation of a 3D prototype have already been presented in section III.4.3, in order to allow for simulation studies for which the results are applicable to the experimental tests. As detailed above, the optimal distribution of sensors across a sphere and the conception of practical solutions are not as straightforward as for the 2D case. Practicality plays a much more central role when it comes to the selection of suitable 3D sensor configurations. Since no adequate tri-axial sensor solutions are currently available for the application in mind, the design of the prototype focuses on sensor arrangements that are well adapted to the punctiform mono-axial measurements that can be obtained using the FLCXS2-500.

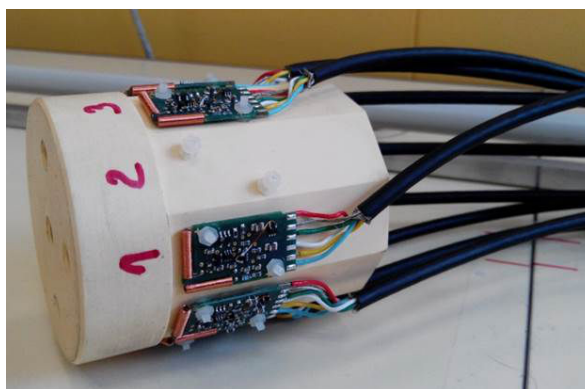


*Figure IV.1: 2D prototype.*

### IV.3. 3D prototype

As explained in section III.4.3, the placement of the sensors on several discs that represent cross-sections of the sphere prove to be a well-adapted solution since all sensors then measure the field along  $\vec{B}_\varphi$  and these measurements can be input directly into the inverse problem. The design of the 3D prototype is provided in Fig. IV.2. The parameters for the 3D sensor array are summarized again below:

**3D sensor array parameters:** sensors distributed on sphere with  $r = 4.5$  cm;  
 $N_S = 30$  on five discs with  $\varphi_i = i \cdot \frac{2\pi}{6}$  for  $i = 0, 1 \dots 5$   
 central disc  $r_0 = 4.50$  cm  
 discs at  $h_{\pm 1} = \pm 1.5$  cm ;  $r_{\pm 1} = 4.24$  cm ;  $\varphi_{\pm 1} = \varphi_i \pm \frac{\pi}{6}$   
 discs at  $h_{\pm 2} = \pm 3.0$  cm ;  $r_{\pm 2} = 3.36$  cm ;  $\varphi_{\pm 2} = \varphi_i \pm \frac{2\pi}{6}$

The array of the central disc (and thus of the sphere) is a direct consequence of the magnetic sensor dimensions ( $2.9 \times 1.6$  cm), since this is the limit for the planar placement of the sensors on the three interior discs, which is a requirement for minimal sphere sizes with the given sensors. The two symmetrical outer discs can have smaller radii, since the sensors can be inclined without changing the orientation of the measurement axis<sup>1</sup>. A remaining constraint was the requirement of a central hole through all discs, in order to allow for the passage of the sensor cables (nine

<sup>1</sup>The term 'disc' therefore does not describe the shape of the outer levels precisely, but is still applicable for the sensor placement and will be used in the following

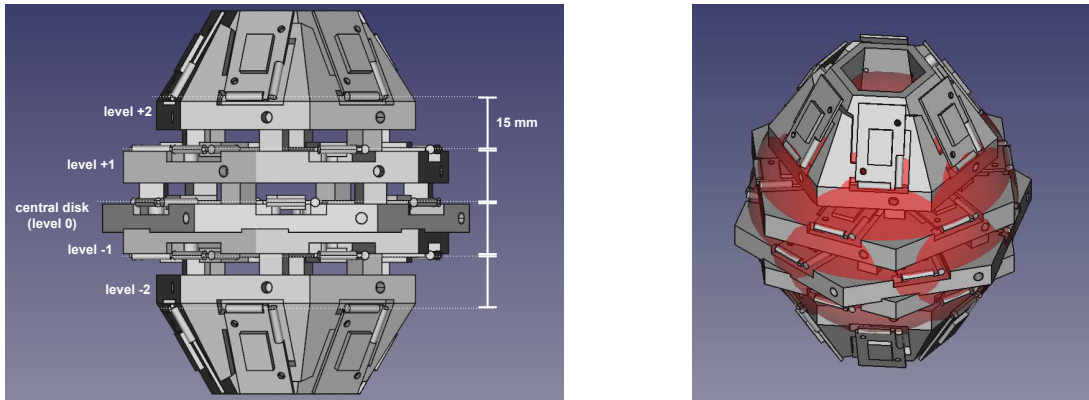


**Figure IV.2:** Design of the 3D prototype with six miniature fluxgate sensors of the type FLCXS2-500 located on five discs, in a way that one sensitive axis of each sensor is located on the sphere (red) of radius 4.5 cm. The distribution across the sphere is further improved by a relative angular offset  $20^\circ$  with respect to adjacent discs.

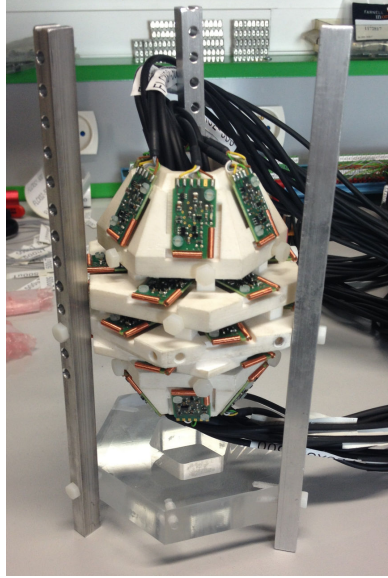


**Figure IV.3:** 3D prototype with 30 miniature fluxgate sensors. Half of the cables of the 18 interior sensors exit the sensor array at the top/bottom respectively and are then joined by six cables from the outer level. The array is attached to three pillars with a series of holes to allow for height adjustment with respect to a conductor passing below the array.

cables to each side of the array, where they are joined by the remaining 6 cables of the outer disc). After the design phase was completed, the sensor support was fabricated using a 3D printer and holes were drilled into the support to allow for the fixation of the sensors (2 diagonal holes per sensor). To reduce the number of pieces, one of the discs of the first level was attached to the central disc (so that the thickness of this piece equals the height of the first level [1.5 cm]). The four remaining pieces are separable and the distances are assured by spacers created during the printing process. An image of the completed prototype is provided in Fig. IV.3, which also depicts the three aluminium pillars used to hold the sphere in place and to adjust the relative height above the conductor between 5 and 12 cm using screws.

#### IV.4 Laboratory setup

A photo of the laboratory setup is provided in Fig. IV.4 and shows the two straight conductors  $I_0$  and  $I_1$  and the first (2D) sensor array prototype, as well as the computer for data acquisition. A set of three KEPCO power units is used to induce direct currents (DC) between 0 and 30 A and can be controlled via a LabVIEW® interface which can also return current values  $I_0(a_n)$  derived from

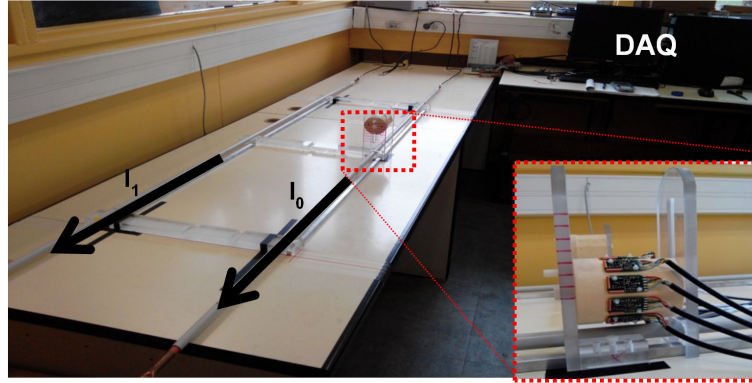


**Figure IV.4:** Laboratory setup with two conductors and the PC for data acquisition. The sensor array (first 2D prototype) is placed above the primary conductor  $I_0$  (adjustable height between  $d_0 = 5.5$  and  $11$  cm) and the distance to the secondary, perturbative conductor can also be adjusted  $\Delta x = 20$  or  $40$  cm.

the solution of the inverse problem, if the array parameters (matrix  $\mathbb{A}(r, \vartheta_i)$  and transfer factors  $k_{a_n/b_n}$ ) are input. A PCIe-6323 card from National Instruments® is used for data acquisition. It provides 32 analog inputs with 250 kS/s at resolution of 16 bit. This allows the acquisition of the sensor signals from the array. In addition, the card includes four analog outputs, used to command the KEPCO current sources, and 48 channels of digital input/output. Two connecting blocks are used to wire the sensors of the various configurations/prototypes to the inputs of the PCIe. Each fluxgate sensor provides the measurement with respect a reference at  $0.5 \cdot [\text{supply voltage}] \pm 1\% = [6 \pm 1\% \text{ V}]$ . The reference signals are connected in parallel via resistances of  $R = 100 \Omega$ , which allow for the equalization of potential differences, so that a unique reference potential is used for the measurements. The signals are also passed through a filter, in order to eliminate noise at other frequencies, e.g. the excitation signal of the fluxgate sensors (next section). The balanced reference signal can then be connected to the reference input of the DAQ card ('AI SENSE') and the sensor signals can be connected directly, thus maximising the number of usable input channels. The measurements from two shunts (one connected in series with each conductor) are connected as differential inputs and employed as references for DC measurements.

## IV.5 Magnetic sensor characterization and offsets

Based on the sensor characteristics, the following effects must be considered in the evaluation of the measurements:

- **Sensor offset:**

Intrinsic sensor offset: typically  $V^{\text{off}} < 10$  mV, can be characterized (in a "zero-field" chamber) and subtracted

- **Sensor noise:**

- Noise due to the excitation coil signal at 16.7 kHz ( $< 40$  mV peak-to-peak, which corresponds to  $4 \mu\text{T}$ ) and which can be reduced using a signal filter (capacitor-input/ $\pi$  filter)
- Intrinsic sensor noise:  $< 5$  nT (peak-to-peak) for 0.1 to 10 Hz

- **Contribution of external field sources:**

On the one hand, the geomagnetic field, approx.  $\pm 50 \mu\text{T}$ , depends on the position and orientation of the sensor array, but also the sum of fields from ferromagnetic materials/ current flows in the environment. The latter depend strongly on the specific environment. This fact was highlighted by the different conditions that were determined after a relocation of the institute during the course of this thesis. While the geomagnetic field was the dominant environmental field before the move (on the university campus in Grenoble) and exhibited only minor variations over time, a three times stronger field ( $\sim 150 \mu\text{T}$ ) was observed after the relocation (new site: Polygone Scientifique in Grenoble), where the field also showed much stronger spatial (on the sub-meter scale) and temporal variations (over the course of one day). While these ambient fields complicate measurements that serve the detailed characterization of the sensor arrays, e.g. the determination of potential sensor misalignments, to the extent that these are rendered impossible, they do not affect the current determination using spatial harmonics, since the influence of the surrounding field can be eliminated using differential measurements (as long as the temporal variations do not occur on the scale of seconds or below) for DC measurements or by application of an FFT for AC measurements. The ambient noise would otherwise impact the fourth order contribution to the field.;

The overall measurement function is:

$$V^{\text{out}}[\text{mV}] = |\vec{B}^{\text{meas}} + \vec{B}^{\text{EMF}}|[\mu\text{T}] \cdot \frac{10 [\text{mV}]}{[\mu\text{T}]} + V^{\text{off}}[\text{mV}] + V^{\text{noise}}[\text{mV}] \quad (\text{IV.1})$$

Where the field measurement  $\vec{B}^{\text{meas}}$  ideally only includes the field resulting from the current flow in the conductor below the sensor array (and the perturbative current flow). In reality, it does of course also include all other ambient magnetic fields, especially that from the return conductors. The path of the return conductors was thus chosen to maximise the distance of the measurement

#### IV.5. Magnetic sensor characterization and offsets

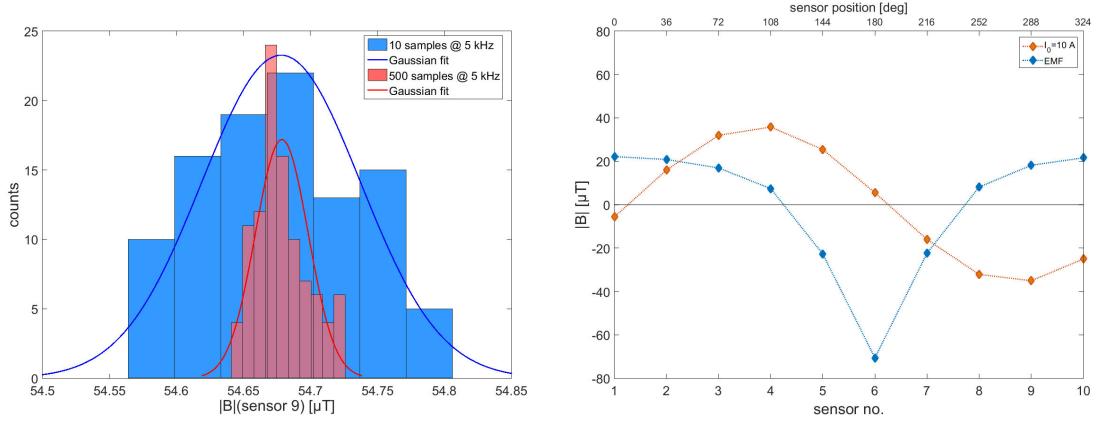


**Figure IV.5:** Influence of data acquisition parameters and the geomagnetic field on magnetic field measurements. Left: distribution of 100 field values measured with sensor no. 9 ( $\vartheta_i = 288^\circ$ ) for  $I_0 = 30$  A;  $d_0 = 11$  cm with 10 samples (blue) and 500 samples (red) at 5 kHz. Fit with the normal distribution and the following parameters:  $[\mu_{10samp.} = 54.68 \mu\text{T}$ ;  $\sigma_{10samp.} = 0.06 \mu\text{T}$ ] and  $[\mu_{500samp.} = 54.68 \mu\text{T}$ ;  $\sigma_{500samp.} = 0.02 \mu\text{T}$ ]. Right: Comparison of the magnitude of the magnetic field for  $I_0 = 30$  A;  $d_0 = 11$  cm and the geomagnetic field (for the given sensor configuration and orientation).

from bends in the conductor path and the return currents. Since it was possible to return the conductors along the ceiling, the distance to the sensor arrays was 2 – 3 m, thus rendering the influence of the return conductors negligible with respect to the perturbing conductor at  $\Delta x < 0.5$  m. For the measurements made on the university campus in Grenoble, the relative amplitude of the geomagnetic field is provided on the right-hand-side of Fig. IV.5 for the given orientation and is compared to the field measured with the sensor array 6 cm above a conductor carrying a current of 10 A. After the correction of the intrinsic offset and the deduction of the ambient magnetic field contribution (for a given setup) the measurement function is reduced to

$$V^{\text{out}}[\text{mV}] = |\vec{B}^{\text{meas}}|[\mu\text{T}] \cdot \frac{10 [\text{mV}]}{[\mu\text{T}]} + V^{\text{noise}} \quad (\text{IV.2})$$

The effect of sensor noise can be further reduced by using a statistical average of a stable magnetic field. For example, the left side of Fig. IV.5 shows that the acquisition of 500 samples of  $\vec{B}^{\text{meas}}$  at a frequency of 5 kHz, provides a significant reduction of measurement noise in comparison to the acquisition of 10 samples at the same frequency. This can be applied directly to DC measurements, so that all results presented for DC measurements in the following chapter are determined using statistical averages (100 samples at 5 kHz), while the feasibility of such data processing for on-site measurements must be studied carefully for subsequent test phases. It can already be stated, that

the same temporal averaging is not possible for AC measurements, which, in turn, profit from the application of a direct FFT.

This chapter served to detail the practical implementation of the sensor arrays for the application of the 2D and 3D decomposition of the magnetic field in spatial harmonics. The design had to allow for the placement of the sensors on a circle/sphere of a given (or minimum) radius, which is selected to enable the detection of desired higher order contributions to the field (which provide enhanced geometrical selectivity). Furthermore, a suitable magnetic field sensor technology was identified amongst the commercial products and its dimensions were also a decisive element of the design process. With the sensor arrays and laboratory setup detailed above, it is now possible to proceed with the description of the performed measurement series and the evaluation of the measurement results, which will be presented in the following chapter.



---

## Experimental results

---

---

V.1	2D measurement arrays . . . . .	<b>108</b>
V.1.1	Transfer factors . . . . .	108
V.1.2	Effect of perturbing conductor . . . . .	111
V.1.3	Reproducibility (second sensor array) . . . . .	115
V.1.4	Calibration method . . . . .	121
V.1.5	AC measurements . . . . .	124
V.2	3D measurement array . . . . .	<b>131</b>
V.3	Conclusion and Perspectives . . . . .	<b>133</b>

---

Chapter III introduced and detailed the measurement principle which provides the basis for spatially selective current measurements. Chapter IV then described the necessary technical considerations that allow the application of the measurement principle to a specific task, i.e. current measurements in the laboratory for the given case. Only the combination of these two fundamental building blocks results in a complete current measurement method, which is adapted to the application (Fig II.1). Therein, the considerations concerning the technical implementation are based entirely on the conclusions drawn from the study of the theoretical framework, which emphasizes again, that the design and selection of a suitable sensor technology and configuration acts as the enabling/bridging element between measurement principle and application, and can be exchanged or adapted for different measurement conditions. Since the two elements have been established and studied in detail for current measurement in the laboratory, it is now possible to proceed with

the presentation and discussion of the experimental results, with a focus on the validation and quantification of the geometrical selectivity provided by the approach. The analysis of the different parameters that influence the measurement accuracy or are relevant to the future development and maturation of the measurement method present further points of interest. For example the possibility and means of calibration is a decisive factor for the applicability of the proposed solution. The experimental results are presented below with an increasing level of complexity (of the measurement conditions), and accordingly with increasing detail, thus emulating in large the chronological order of the measurement series.

## V.1 2D measurement arrays

To test the applicability of the 2D measurement principle using the setup described in the previous chapter, the sensor array (radius  $r = 3.2$  cm) is placed at a distance  $d_0 = 11$  cm above ( $\varphi_0 = 180^\circ$ ) the primary conductor and a DC current between 10 and 30 A (for reference: a current of 10 A at 10 cm results in a magnetic field magnitude of  $|\vec{B}| = 20 \mu\text{T}$ ). The distance is rather large at first, to ensure that the decomposition with 10 sensors and thus up to the maximum order  $N = 5$  is sufficient to reconstruct the field. It is thus possible to perform magnetic field measurements and to determine the coefficients ( $a_1$ – $a_4$ ,  $b_1$ – $b_4$ ) from the solution of the inverse problem.

### V.1.1 Transfer factors

For the setup described above, only the development terms governed by the coefficients  $a_1$  –  $a_4$  result in significant contributions (near-zero values for coefficients  $b_n$  at ( $\varphi_0 \approx 180^\circ$ )). The relationship  $a_n(I_0)$  obtained can be compared to the analytical expression:

$$a_n(I_0) = \frac{\cos(n\varphi_0)}{nd_0^n} I_0 = k_{a_n} I_0 \quad (\text{V.1})$$

$$b_n(I_0) = \frac{\sin(n\varphi_0)}{nd_0^n} I_0 \xrightarrow{\varphi_0 \approx 180^\circ} b_n \approx 0 \quad (\text{V.2})$$

However, a linear and reproducible relationship  $a_n(I_0)$  is of paramount importance, since once a transfer function has been defined, it can be used instead of the analytical expression to determine the current values based on the obtained coefficient values.

The determination of the transfer factors were the first measurements to be completed for the laboratory setup and prototype. At this point only the first prototype (A) was ready for testing. Figure V.1 shows the data values for  $a_4$  obtained throughout the DC range. The linear fit of the

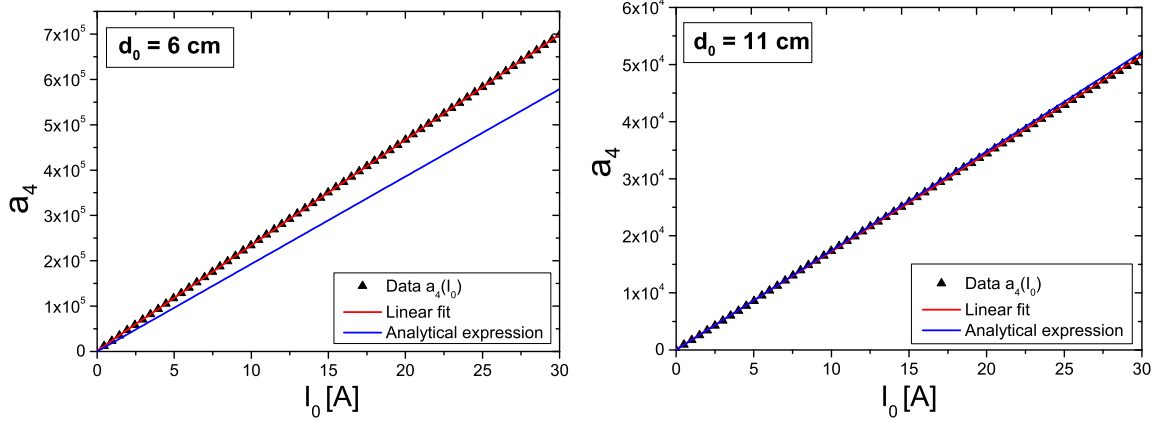


**Figure V.1:** Transfer factor  $k_n$  for array A at two different positions  $d_0 = 6$  and  $11$  cm above the conductor  $\varphi_0 = 180^\circ$ .

data points and the analytical function are provided for reference and comparison purposes. The slope of the linear fit can be compared to the factor  $k_{a_n} = \frac{\cos(n\varphi_0)}{nd_0^n}$  from Eq. V.2.

A comparison of the theoretical and experimentally obtained transfer functions is provided in TableV.1, along with the adjusted  $R^2$  values which confirm that the transfer functions is indeed linear. The reproducibility of the obtained results can be confirmed using both curves obtained at  $I_1 = 0$  and with a constant perturbing current  $I_1$ , since this only results in a constant contribution/offset of the curve  $a_n(I_0)$ . The coefficients obtained during the tests of the perturbing current (presented in the next section), can thus also be exploited here and are presented on the right-hand side column of TableV.1. These values were, however, acquired after the array had been shifted several times between the different heights above the conductor. The difference in transfer factors, which is especially strong for higher orders, can thus be explained with a variation in  $d_0$  (and possibly  $\varphi_0$ , but with a smaller resulting error). This is however not a problem for precision measurements, because the array is usually not moved intentionally after the transfer factor has been determined. Here the evaluation of multiple curves, simply serve to demonstrate the repeatability of the transfer factor determination once the array is installed. At  $d_0 = 11$  cm, the obtained transfer factors  $k_{a_n}$  exhibit good correspondence to the theoretical expression, indicating that the decomposition up to the fourth order provides an accurate reconstruction of the field at this position. The deviation from the analytical factors for the higher orders at  $d_0 = 6$  cm was expected after the analysis of the measurement geometry in Chapter III. Since an increasing number of orders is necessary to accurately describe and reconstruct the field as the decomposition center approaches

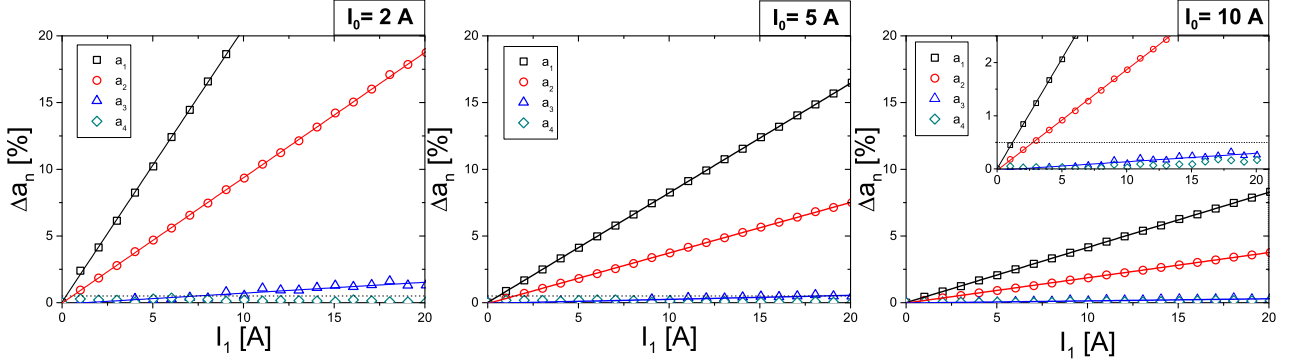
V.1. 2D measurement arrays

	Analytical factor $k_{a_n} = \frac{\cos(n\varphi_0)}{nd_0^n}$	Experimental data			mean value for 40 curves $I_0 \in [0; 10]$ A and $I_1 = \text{const.} \in [0; 20]$ A $\pm$ std. dev.
		for $a_n(I_0 = 0 \dots 30\text{A})$		adj. $R^2$	
		slope	$a_n(I_0 = 0)$		
<b><math>d_0 = 11</math> cm</b>					
$k_{a_1}$	-9.13	-9.42	-0.6	1	$-9.45 \pm 0.05$
$k_{a_2}$	41.70	42.50	2.1		$42.4 \pm 0.2$
$k_{a_3}$	-253.9	-256.6	-27		$-256 \pm 2$
$k_{a_4}$	1739	1713	98		$1703 \pm 22$
<b><math>d_0 = 6</math> cm</b>					
					(20 curves)
$k_{a_1}$	-16.67	-16.9	-0.9	1	$-17.65 \pm 0.01$
$k_{a_2}$	138.9	140.6	8.5		$153.26 \pm 0.02$
$k_{a_3}$	-1543	-1618	-122		$-1851.7 \pm 0.4$
$k_{a_4}$	19290	23245	1790		$27862 \pm 16$

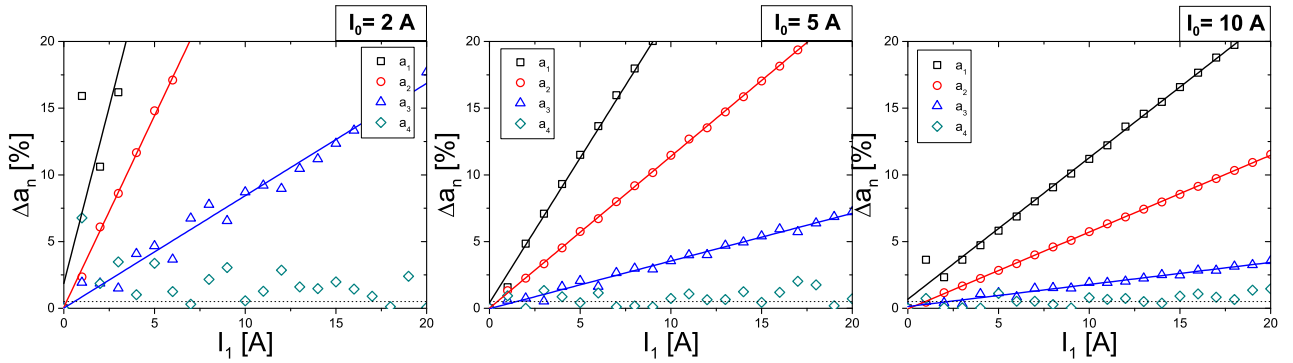
**Table V.1:** Summary of the linear regression results for  $a_n(I_0)$  and comparison with the theoretical values of Eq. III.13. Besides measurements at  $I_1 = 0$ , curves obtained at  $I_1 = \text{const.}$  can also be evaluated to increase the number of reference curves for the reproducibility tests (right-hand column).

Measurement setup: [ $d_0 = 11$  cm,  $\varphi_0 = 180^\circ$ ]; [ $d_1 \approx 41.48$  cm,  $\varphi_1 \approx 105.4^\circ$ ] and [ $d_0 = 6$  cm,  $\varphi_0 = 180^\circ$ ]; [ $d_1 \approx 40.45$  cm,  $\varphi_1 \approx 98.5^\circ$ ].

the source, the analytical expressions will no longer hold for a limited maximum order after a given limit. The decreasing relative magnitude of the contributions of higher orders further serves to explain the fact that the deviation from the analytical expression is strongest for these orders. In this case, the decomposition up to the fourth order is insufficient to describe the field at  $d_0 = 6$  cm and the fifth order would theoretically be necessary to obtain the exact and analytical expressions. This explanation is supported by the fact, that a simulation with the same array parameters and position yields a value of  $k_{a_4} = 24928$ , which is closer to the experimental value than the analytical solution. However, as stated above, a precise reconstruction of the theoretical relationship is not the primary objective. As long as the transfer function is linear (as indicated by the adjusted  $R^2$  values), reproducible (as indicated by the low standard deviation for multiple linear regressions) and determinable, it is possible to deduce the current value from the coefficients. The next step is to examine the effect of a perturbing conductor on the coefficient values, which will be detailed in the following section.



(a) Measurement setup: Array A at  $[d_0 = 6 \text{ cm}, \varphi_0 = 180^\circ]$ ;  $[d_1 \approx 41.48 \text{ cm}, \varphi_1 \approx 105.4^\circ]$ .



(b) Measurement setup: Array A at  $[d_0 = 11 \text{ cm}, \varphi_0 = 180^\circ]$ ;  $[d_1 \approx 40.45 \text{ cm}, \varphi_1 \approx 98.5^\circ]$ .

**Figure V.2:** Coefficient error  $\Delta a_n$  for increasing perturbation current  $I_1 = 0$  to 20 A and three different primary current magnitudes  $I_0 = 2, 5$  and 10 A. The values at  $I_1 = 0$  serve as references. The lines present the linear fit for  $a_1$  to  $a_3$ .  $a_4$  does not exhibit a measurable linear dependence.

## V.1.2 Effect of perturbing conductor

After confirmation of the linear relationship  $a_n(I_0)$ , it is possible to examine how this relation is affected by the magnetic field from a secondary conductor. For this purpose, a current is run through the conductor  $I_1$  which is initially positioned at a distance of  $x = 40 \text{ cm}$  from the primary conductor and thus at  $[d_1 \approx 41.48 \text{ cm}, \varphi_1 = 90^\circ + \tan^{-1}(\frac{11 \text{ cm}}{40 \text{ cm}}) \approx 105.4^\circ]$ .

The effect of the perturbing field on the coefficient values is provided in Fig. V.2, where for three different current values in the first conductor ( $I_0 = 2, 5$  and 10 A), the perturbing current is swept from  $I_1 = 0$  to 20 A and thus up to 10 times the nominal current in the primary conductor. Fig. V.2 shows that the effect of the magnetic field emanating from the perturbing conductor is strong for the coefficients of lower orders. For  $a_1$ – $a_3$  the error depends on the relative magnitude of the

nearby and distant conductors  $\frac{I_0}{I_1}$ . For  $a_4$  the impact of the perturbing conductor is negligible and the remaining offset is of random nature and does not show a measurable dependence on  $I_1$ . This confirms the simulation results and demonstrates the effectiveness of the measurement principle. In these first results, the error for current determinations using the coefficient  $a_4$  can be limited to below  $\Delta a_4 = \Delta I_0 \leq 2.5\%$  for large array-to-conductor distances ( $d_0 = 11$  cm,  $d_1/d_0 = 3.8$ ) and substantial current magnitudes ( $I_0 \geq 5$  A). For lower current magnitudes ( $I_0 = 2$  A), the variation can be limited to  $\Delta a_4 = \Delta I_0 \leq 7\%$ , although all but one value even lie below 5%. If the array is approached closer to the conductor ( $d_0 = 6$  cm,  $d_1/d_0 = 6.7$ ), the error can be limited to  $\Delta a_4 = \Delta I_0 \leq 0.5\%$  overall, and may reach significantly lower values for large current magnitudes  $I_0$ , due to the reduction of noise in the measured values.

Fig. V.2 shows that, for low current values (i.e. low field magnitudes) or large array-to-conductor distances, the signal-to-noise ratio is reduced, so that the identification result is increasingly subject to perturbations (several outliers can be observed). If the distance from conductor to sensor is decreased (from 11 to 6 cm) or the current is increased, the variations in coefficient values are reduced. This is due to the fact that, for a given sensor noise characteristic, the signal-noise ratio is dependent on these two parameters. The behaviour is amplified by the fact that the contribution of higher orders is also reduced with increasing array-to-conductor distance  $d_0$  (see Chapter III). The lower magnitude of the higher (specifically: the fourth) order coefficients and of the resulting relative contribution to the total magnetic field  $B_4/B_{\text{total}}$  makes these coefficient values more susceptible to variations (and to the influence of noise) at larger distances. Further possible sources of errors can be attributed to the characteristics of the sensor array (misalignment of individual sensors) and the intrinsic sensor noise. This underlines the interest in performing further sensor (array) characterization to further reduce the determination error. With respect to the obtained precision, it is also important to note again, that the experimental data provided above is obtained with statistical averages (100 magnetic field measurement samples at 5 kHz) to reduce sensor noise. The feasibility of such statistical processing must be assessed carefully for on-site measurement conditions.

The measurements with the two-conductor system also demonstrate that the dependency of lower coefficients on the perturbing conductor  $a_1(I_1)$ – $a_3(I_1)$  is in fact also a linear relationship (as expected), while  $a_4$  appears to be independent of  $I_1$ . The results of the linear regressions are summarized in Table V.2. The slope/dependence of  $a_2(I_1)$  corresponds well to the theoretical value, while the slope of  $a_1(I_1)$  includes some contributions from other field sources (most notably the conductor return paths). Since the disturbing conductor  $I_1$  is further away from the sensor array than the conductor with  $I_0$  ( $x = 40$  cm); the relationship  $a_1(I_1)$  is much more sensitive to

	Analytical factor $k_{a_n} = \frac{\cos(n\varphi_1)}{nd_1^n}$	Experimental data	
		mean value for 40 curves with $I_0 \in [0; 10]$ A and $I_1 \in [0; 20]$ A slope $\pm$ std. dev.	adj. $R^2$
<b><math>d_0 = 11</math> cm</b>			
$k_{a_1}$	-0.64	$-1.01 \pm 0.03$	1.00
$k_{a_2}$	-2.50	$-2.45 \pm 0.03$	1.00
$k_{a_3}$	3.37	$4.47 \pm 0.15$	0.98
$k_{a_4}$	4.02	non-linear	0.17
<b><math>d_0 = 6</math> cm</b>			
(20 curves)			
$k_{a_1}$	-0.37	$-0.72 \pm 0.01$	1.00
$k_{a_2}$	-2.92	$-2.90 \pm 0.01$	1.00
$k_{a_3}$	2.18	$2.93 \pm 0.20$	0.92
$k_{a_4}$	7.73	non-linear	0.54

**Table V.2:** Summary of the linear regression results for  $a_n(I_1)$  and comparison with the theoretical values of Eq. III.13.

Measurement setup: [ $d_0 = 11$  cm,  $\varphi_0 = 180^\circ$ ]; [ $d_1 \approx 41.48$  cm,  $\varphi_1 \approx 105.4^\circ$ ] and [ $d_0 = 6$  cm,  $\varphi_0 = 180^\circ$ ]; [ $d_1 \approx 40.45$  cm,  $\varphi_1 \approx 98.5^\circ$ ].

other field sources. Like  $I_1$ , the return conductor of the measurement setup [located  $2 \sim 3$  m diagonally ( $\varphi_2 \approx \pi/4$ ) above the setup] can also contribute to the slope of  $a_n(I_0)$ , with the same decreasing effect for each higher order. The measurement setup was conceived to minimize the effect of the return conductor within the constraints defined by the laboratory dimensions. The point of measurement (array position) is placed at the middle of the two parallel conductors ( $I_0$  and  $I_1$ ) and the return conductors then rise vertically at the end of the laboratory on either side. The vertical sections create a field in a perpendicular plane to that of the investigated currents. The circuit is then completed with a parallel section, which is placed at a maximum distance (attenuation factor for  $d_0 = 6$  cm:  $d_2/d_0 \approx 2.5/0.06 \approx 42$ ), since it creates a field in the same plane as the measurement plane and thus acts as a secondary perturbing current  $I_{\text{return}} = I_2$ . For a precise analysis the entire return circuit must be simulated with the exact conductor paths. This is not a primary point of interest here, but a very basic first approximation is possible: given the symmetry of the vertical sections and, consequently, assuming that the parallel section of the return path is the main contributor, its effect can be estimated using the analytical formulas to amount to  $k_{a_n}(I_2) = \frac{\cos(n\pi/4)}{n(2.5)^n}$ , and thus to  $k_{a_1}(I_2) = 0.28$ ,  $k_{a_2}(I_2) \approx 0$ ,  $k_{a_3}(I_2) = -0.02$  and  $k_{a_4}(I_2) = 1$  for the individual orders. A noticeable contribution of this part of the return circuit can therefore only be observed for the first order, where the contribution is of the same order of

magnitude as that of  $I_1$  (attenuation factor  $d_2/d_1 \approx 2.5/0.4 = 12.5$ ). Since the angular placement of the return conductor is advantageous for the second order coefficient  $a_n$  [ $\varphi_2 \approx \pi/4$  and  $a_2(I_2) \propto \cos(2\varphi_2)$ ], the contribution of the parallel section of the return conductor should be near-zero. The dependence  $a_3(I_1)$  already exhibits a significant deviation from the linear relationship and the coupling to  $I_0$  is already weak. Other (dynamic) field sources within the environment can also contribute to the relationship, but the value of the intercept shows very good correlation with the (constant) value of  $I_0$ . Due to the superposition of the magnetic fields, the contributions to the coefficient values from the individual magnetic field sources (currents) can be written as follows for the ideal (perfect) 2D case:

$$a_n = \sum_{i=0}^{N_C} \frac{\cos(n\varphi_i)}{nd_i^n} I_i \quad (\text{V.3})$$

Nevertheless, the linearity of  $B$  with  $I_i$  allows to write more generally:

$$a_n = f_0 \cdot I_0 + f_1 \cdot I_1 + \dots \quad \text{with} \quad f_i = k_{a_n}(I_i) \quad (\text{V.4})$$

This relation is confirmed by the experimental results, with the deviations from the theoretical transfer factors described above. This observation provides the opportunity to exploit lower order coefficients, in order to determine (or at least estimate) the current value in the distant conductor and to thereby enhance the combination of results from several sensor arrays (at each conductor).

Furthermore, depending on the relative angular positions of the conductor system, individual coefficients may exhibit an advantageous (reduced) dependence on a perturbing conductor, as seen for the coefficient  $a_2$  and the parallel part of the return conductor  $I_2$  above. The proportionality to  $\cos(n\varphi)$ , can lead to near-zero contributions for a perturbation at a given angle. In this case, i.e. a very specific geometrical arrangement, a lower order could potentially also show better rejection of the perturbing conductor than higher orders and this effect could be exploitable to enhance the geometrical selectivity or reduce the number of required sensors in a given case. However, such a setup would increase the dependence on geometrical parameters and the robustness with respect to variations in the geometrical configuration would have to be studied carefully.

The first series of test with array A have confirmed that the measurement method can achieve the required precision in current measurement ( $\Delta I_0 \leq 0.5\%$ ) and it is now possible to confirm the reproducibility of the results, by performing identical measurements with a second sensor array B, produced with the same geometrical parameters and equipment. The level of possible variations in array parameters is strongly dependent on the fabrication conditions for these laboratory proto-

types, so that for future prototypes with different configurations, sensor technology and fabrication equipment, a similar analysis would have to be repeated. Nevertheless, the results and conclusions that are presented in the following section serve to establish a valuable knowledge base for the effect of possible (minor) variations in array parameters and it can be assumed that the fabrication precision (e.g. sensor placement or alignment) can at least be matched, if not improved, for industrial prototypes.

### V.1.3 Reproducibility (second sensor array)

A further decisive factor for the application of the measurement principle for long-term measurements (in the grid) is the reproducibility of the measurement results. To study possible deviations between measurement arrays, a second measurement array with identical dimensions and sensor distribution was manufactured (at G2Elab). The two arrays are designated array A and B, in order of their fabrication. Since the transfer factor is the central element that links the coefficients obtained from the measurement (via the solution of the inverse problem) to the current values, they are used as indicators for the reproducibility with either array. After fabrication of the second 2D array, both arrays can be fixed at the same relative position to the conductor and the trans-

Experimental data				
	fixed	rotated	fixed	range [%]
<b>Array A</b>				
$k_{a_1}$	-9.71	-9.73	-9.74	$\pm 0.02$
$k_{a_2}$	42.6	41.4	42.7	$\pm 1.7$
$k_{a_3}$	-260	-254	-262	$\pm 1.6$
$k_{a_4}$	1738	1800	1754	$\pm 1.8$
<b>Array B</b>				
$k_{a_1}$	-9.56	-9.63	-9.57	$\pm 0.4$
$k_{a_2}$	40.6	42.2	40.6	$\pm 2.2$
$k_{a_3}$	-272	-275	272	$\pm 0.6$
$k_{a_4}$	2416	1567	2409	$\pm 22.9$

**Table V.3:** Reproducibility test for two 'identical' 2D measurement arrays. Each array is secured in a fixed relative position to conductor  $I_0$ , then rotated by  $\vartheta_r = 180^\circ$ , thus effectively making sensor no. 1 assume the position previously occupied by sensor no. 6. The array is then returned to the original orientation and the procedure repeated for the second array. After each change of position, the height is manually set to  $d_0 = 6$  cm.

fer factors can be compared. The summary of this comparison is provided in Table V.3. In the initial, 'normal' configuration, the transfer factors of the first three orders correspond rather well between the two arrays. However, the fourth order transfer factor  $k_{a_n}$  exhibits a significant deviation. While either array would be equally operational once the respective transfer factors have been determined, an analysis of this difference is meaningful, in order to increase the understanding of the measurement method. Since the value obtained with array A is significantly closer to the theoretical value of  $k_{a_4}^{\text{theo}} = 1739$  at  $d_0$  (at which the correspondence between theory and experiment is strong, see previous section and Ch. III) and also shows a much better reproducibility, it is possible to focus the search for an explanation on variations in the configuration of array B. A first approach to finding the root of the offset in array B is to determine the transfer factors for a different configuration.

Since it is possible to rotate the entire array by  $180^\circ$  and to thereby shift the distribution of magnetic field values (the sensor positions are rotated to  $\theta_i + 180^\circ$ , e.g. the first sensor takes the place of the sixth sensor). With respect to the magnetic field created by the current flow, this effectively means that sensors that were previously positioned and oriented to measure low (near-zero) field values will now measure stronger field values and vice versa. In consequence, the effect of sensor misalignments will change. Effectively, the sensors on the half of the sensor array which was initially further away from the conductor are subject to larger field magnitudes after rotation, and the sensors measuring near-zero field values also change with rotation (from sensors 4 and 8 to 3 and 9, see Fig. IV.5). As shown in Table V.3, the rotation of array B did indeed shift the fourth order transfer factor toward the value of array A as well as the theoretical value, while resulting only in minor modifications in the other orders. After the rotation, the evaluation is performed once again in the original configuration to confirm the observed changes. A misalignment of one or more (sensors) in array B thus presents a possible explanation for the variations. This will be studied in detail below.

### **Misalignment analysis**

To determine whether misalignments of individual sensor axes can explain the observed deviation in the transfer factor  $k_{a_4}$  between the two arrays, the field measurements were compared to tri-axial reference measurements. Since these measurements cannot be performed in the same location, their comparison requires a spatially homogeneous field. As mentioned in the previous chapter, the entire engineering school (and research labs) moved to the brand new GreEn-ER building across Grenoble in July 2015: the setup was relocated to a new location during the experimental phase. In the first location, the ambient magnetic field (predominantly the geomagnetic

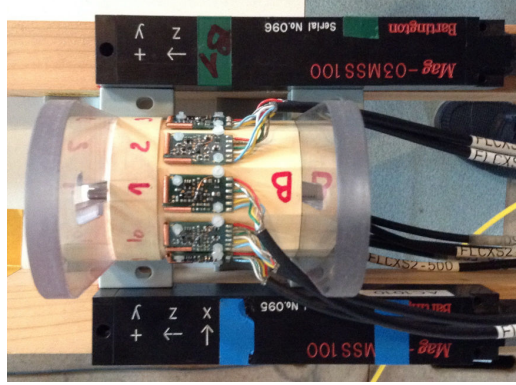


**Figure V.3:** Setup for misalignment determination. The sensor array (array B in the photo) is placed between two tri-axial Fluxgate magnetometers in a stable ambient magnetic field (predominantly the geomagnetic field). Photo taken during the measurements at LMMCF (second test series), for which the z-axis of the reference magnetometers is pointing southward. In this setup, the reference values provided by the Bartington sensors amounted to  $||[\vec{B}_x, \vec{B}_y, \vec{B}_z]|| = [-1.71, 40.87, -23.07] \mu\text{T}$ .

field) was sufficiently homogeneous on the scale of the array to allow for a misalignment analysis. Since the ambient field now exhibits much stronger spatial (and temporal) variations in GreENER, the same analysis could not be performed in the laboratory after relocation (and thus after the fabrication of the second 2D array). In fact, measurements with identical reference sensors on either side of the array (and with the same orientation) were subject to variations up to several microtesla, i.e. the field is inhomogeneous even across the diameter of the array. After relocation it was thus necessary to perform the misalignment analysis at the Low Magnetic Fields Metrology Laboratory (LMMCF) of G2Elab outside the city, built in a carefully selected location where the field can be considered spatially homogeneous. The setup for the misalignment measurements is displayed in Fig. V.3.

The employed tri-axial magnetometers were two fluxgate magnetometers Mag-03MSS100 (range:  $\pm 100 \mu\text{T}$ , noise:  $< 10 \text{ pT}_{\text{RMS}}/\sqrt{\text{Hz}}$  at 1 Hz, precision  $< 0.5\%$ , orthogonality error  $< 0.5^\circ$ ) from Bartington Instruments. These reference magnetometers were aligned with the stand of the 2D array on either side of the arrays. Given the tri-axial reference measurements,  $[B_x^{\text{ref}}, B_y^{\text{ref}}, B_z^{\text{ref}}]$ , and under the assumption of a spatially homogeneous magnetic field, the magnetic flux density  $B_\vartheta(\vartheta_i)$  measured at a position  $\vartheta_i$ , can be related to reference measurements using the misalignment angles  $\alpha_i, \beta_i$  as follows:

$$B_\vartheta(\vartheta_i) = \cos(\alpha_i) \cos(\beta'_i) B_x^{\text{ref}} + \sin(\alpha_i) B_y^{\text{ref}} + \sin(\beta'_i) B_z^{\text{ref}} \quad \text{with} \quad \beta'_i = \beta_i + \frac{2\pi}{10} \cdot (i-1) \quad (\text{V.5})$$

The substitution  $\beta'_i = \beta_i + \frac{2\pi}{10} \cdot (i - 1)$  serves to incorporate the rotation of the sensor axis depending on the angular position of a particular sensor and so that the misalignment  $\beta_i$  corresponds to its definition as a misalignment with respect to ideal axis orientation ( $\beta_i = 0$ ). To determine a set of angular orientation offsets  $\alpha_i$  (rotation around the radial axis  $\vec{e}_r$ ) and  $\beta_i$  (rotation around the axis  $\vec{e}_x$  parallel to the conductor, Fig. III.12) that define the cone within which the axis can be misaligned, it is thus principally necessary to perform multiple field measurements. This is easily understood, by considering the cone created by the angles  $\alpha_i, \beta_i$ , for which multiple combinations of the two misalignment angles can result in the measurement of the same magnetic field magnitude along a given sensor axis. The problem corresponds to the minimization of the function that describes the difference between array and reference measurements ( $|B_{\text{array}}(r, \theta_i) - B_{\text{ref}}(r, \theta_i)|$ ). The second measurement must be performed with a different orientation of the array (and reference sensors) with respect to the (homogeneous) ambient magnetic field (a rotation by  $90^\circ$  presents a favourable case). The combination of both measurements then provides two equations for the two unknowns, or a combined function to be minimized. More than two measurements can further increase the accuracy of the minimization problem. For array A, two measurements were performed at different times and at the two different locations, and they can be combined to solve the system of two equations of type Eq. V.5 or the minimum of the difference function can be determined to obtain the angles  $\alpha_i$  and  $\beta_i$  that account for the deviation between the measured and reference values. The results obtained by the resolution of the equations are provided in Tab. V.4. The majority of values lies in the cone defined by  $[\alpha_i, \gamma_i] \in \pm 0.6^\circ$ , but some significant outliers can be observed. In particular, three misalignment angles exceed  $2^\circ$ , which is difficult to explain with the given array fabrication and sensor placement method. The fixation of the sensors should not allow for such larger misalignments and the alignment of the sensor axis on the PCB was provided at  $< 1^\circ$  by the manufacturer. A plausible explanation for this behaviour could be the missing consideration of angular position offsets  $\Delta\theta_i$  in the formulation of Eq. V.5. These are expected to influence in particular the determination of the misalignment angle  $\beta_i$ , since the two angles describe mispositioning/misalignment within the same plane. Further measurements should be made to obtain a larger number of equations, which would allow for an inclusion of the angle  $\theta_i$  in the description of the problem. The set of all three angles should be determined and used in the further evaluation of the measurement array, and they should especially be considered in the calculation of the reference matrix. While the combined effect of these misalignments on the current determination precision is negligible, since they do not influence the transfer factor of the array (at a given position), they should be taken into account for the calibration method. The simulation parameters for the determination of the reference matrix should correspond as well as

Sensor no.	Experimental data						Misalignment angles	
	Array A at Campus			Array A at LMMCF			$\alpha_i$	$\beta_i$
	$B_{\vartheta}(r, \theta_i)$	$B_{\vartheta}^{\text{ref}}$	$\Delta B_{\vartheta}$	$B_{\vartheta}(r, \theta_i)$	$B_{\vartheta}^{\text{ref}}$	$\Delta B_{\vartheta}$	[°]	
[μT]								
1	-5.25	-5.13	-0.12	-1.25	-1.68	-0.43	-0.84	0.16
2	16.58	17.05	-0.47	22.99	22.69	-0.30	-1.24	-0.25
3	32.52	32.72	-0.20	38.60	38.40	-0.20	-0.67	-0.07
4	36.13	35.89	0.24	39.77	39.44	-0.33	0.08	-2.25
5	25.30	25.35	-0.05	25.28	25.42	0.14	-0.10	0.16
6	5.03	5.13	-0.10	1.45	1.68	0.23	0.21	0.25
7	-16.71	-17.05	-0.34	-23.89	-22.69	1.20	2.36	0.50
8	-32.67	-32.72	0.05	-38.37	-38.40	-0.03	0.11	-0.05
9	-35.34	-35.89	-0.55	-38.55	-39.44	-0.89	-0.07	4.06
10	-24.98	-25.35	-0.37	-24.68	-25.42	-0.74	-0.37	1.02

**Table V.4:** Comparison of magnetic field measurements from the sensors on array A with the reference values for a spatially homogeneous field. The reference values are the average of two measurements with tri-axial fluxgate magnetometers. The measurement was performed on the university campus in Saint-Martin-d'Hères, near Grenoble, where the ambient field is predominantly determined by the geomagnetic field. The misalignment angles  $\alpha_i$  and  $\beta_i$  are determined by minimising the deviation  $\Delta B$ .

possible to the real conditions, in order to reduce the error in the obtained transfer factors.

With respect to the second sensor array (B), the primary interest of the misalignment analysis was to find an explication for the difference in the transfer factor  $k_{a_4}$ , which was observed during the DC sweep calibration described in the previous section. Due to the fact, that the fourth order contribution is the weakest amongst the employed (and detectable) orders, it shows the strongest susceptibility to misalignments in sensor axes. Since the measurement principle relies on the exploitation of the spatial variations of the magnetic field, significant misalignments of individual sensors or an unfavourable combination of smaller misalignments could result in the creation of a 'fake', i.e. additional, fourth order contribution which is not related to the magnetic field created by a current flow. As explained above, the single available measurement for array B does not allow an unambiguous determination of the misalignment angles. The values for this measurement are provided in Tab. V.5 and would only allow for a determination of local minima in the vicinity of the start point  $\alpha = \beta = 0^\circ$ . In order to evaluate the possible source of error in array B, it is therefore only instructive to focus on the observed difference between the measured field values and the reference values  $\Delta B$ . The variations observed for the sensors of array B (summarized in Tab. V.5) show that, besides sensor no. 1 and no. 6, which are aligned to measure near-zero field values,

Sensor no.	Experimental data		
	Array B at LMMCF		
	$B_{\vartheta}(r, \theta_i)$	$B_{\vartheta}^{\text{ref}}$	$\Delta B_{\vartheta}$
	[ $\mu\text{T}$ ]		
1	-0.66	-1.74	-1.08
2	23.46	22.65	-0.81
3	38.85	38.38	-0.47
4	39.26	39.45	0.19
5	26.02	25.46	-0.56
6	0.18	1.74	1.56
7	-22.86	-22.65	0.21
8	-38.27	-38.38	-0.11
9	-39.24	-39.46	-0.22
10	-24.51	-25.46	-0.95

**Table V.5:** Comparison of magnetic field measurements from the sensors on array B to the reference values for a spatially homogeneous field. The reference values are the average of two measurements with tri-axial fluxgate magnetometers. The measurement was performed at G2Elab’s LMMCF controlled-field facility in Herbeys, where the ambient field is predominantly determined by the geomagnetic field.

the second, fifth and tenth sensor exhibit the largest relative variation ( $\vartheta_2 = 3.6\%$ ,  $\vartheta_5 = 2.2\%$ ,  $\vartheta_{10} = 3.7\%$ ) from the reference value. However, since the single measurement does not allow for definite conclusions concerning the misalignments, this initial indication will be combined with a more reliable evaluation method.

To continue the search for the source of deviation in array B, it is possible to take advantage of the fact that the sensor array was intentionally conceived to pose an over-determined problem. Since the array employs ten sensors instead of the minimum eight required for the decomposition up to the fourth order, the evaluation (solution of the inverse problem) can also be performed for a current measurement using nine-element subsets of the ten sensors, to determine the eight coefficient values. For array B, this analysis shows that an omission of the fifth or seventh sensor results in a change in  $k_{a_4}$  from 2413 (mean of two measurements using 10 sensors, without rotation, Tab. V.3) to 1680, which is much closer to the result obtained with array A ( $k_{a_4}^{\text{Array A}} = 1746$ ), the result obtained with array B rotated by  $180^\circ$  ( $k_{a_4}^{\text{rot B}} = 1567$ ) and the theoretical value of  $k_{a_4}^{\text{theo}} = 1739$  at the given distance  $d_0 = 6$  cm. The omission of sensors whose axes are rotated by  $180^\circ$  with respect to one another results in an equal change in the transfer factors. The symmetry of the measured components of the magnetic field if the sensor array is positioned symmetrically above the conductor (see Fig. IV.5) is a plausible explanation for this correspondence. Omission of other sensors

(of other sensor pairs) either did not result in a significant (let alone comparable) improvement of the transfer factor or degraded the correlation of the transfer factors. In general, the standard deviation of the transfer factor  $k_{a_4}$  for the omission of each individual sensor is much smaller for array A ( $1738 \pm 277$ ) than for array B ( $2416 \pm 528$ ), underlining once again the superior robustness of array A. Together with the misalignment analysis which identified sensors 2, 5 and 10 as potential sources of error, the inversion without individual sensors, suggests that the fifth sensor could be the reason of deviation in the measured results. A repositioning of this sensor presents a logical next step, but will only be performed after additional misalignment measurements have been performed for array B, in order to arrive at a final, fully substantiated conclusion.

As discussed above, even though array B displays a significantly different fourth order transfer factor (using all ten sensors), it is still possible to obtain results of comparable quality using the respective transfer factor, since the relationship  $a_4(I_0)$  is linear and reproducible with the same array. However, the above analysis, however showed that array A does not only provide results that are close to the theoretical reference values but also proves to be more robust with respect to variations in array parameters, while array B appears to suffer from the mispositioning/misalignment of an individual sensor. Given this linear relationship between the coefficients and the current and the precision obtained for array A above, it is then necessary to increase the robustness of the measurement method, in particular with respect to variations in relative array position  $d_0, \varphi_0$ . For this purpose, the determination of the transfer factors using a DC sweep, as performed above, must be replaced by the current-independent calibration method. The experimental results for this approach are presented in the following section.

#### V.1.4 Calibration method

The precision in current measurement obtained above relies on the determination of the transfer factor(s)  $k_{a_n}(d_0, \varphi_0)$  once the sensor array has been installed at a given distance and angular position to the conductor of interest. For the results provided above, the transfer factors are determined by injecting a known current in the conductor. As explained in Chapter III, live operating conditions require a calibration method that can be performed autonomously after the installation of the array. The description of this calibration procedure is also provided in section III.3.

In order to test the calibration procedure, which is based on the comparison of (ratios of) coefficient values obtained from measurements with those of a reference matrix calculated for probable array positions, the array (A) is installed at various distances to the conductor and the calibration method is employed to determine the transfer factors. The relevant parameter for current mea-

surement precision is always the transfer factor  $k_{a_n}(d_0, \varphi_0)$ , more specifically the transfer factor of the order of interest (the order used to attain the geometrical selectivity). For a greater level of detail, it is also meaningful to examine the array coordinates  $d_0, \varphi_0$  that are determined by the calibration method. Since the transfer factor is a function of the two coordinates, the imprecision in its determination will always be superior to that of the individual coordinates. For test purposes, the array is positioned above the conductor (i.e.  $\varphi \sim 180^\circ$ ) at  $d_0 = [5, 5.5 \dots 11]$  cm (12 values). At each position, the primary current is swept between 0 and 30 A, in order to obtain reliable reference values  $k_{a_4}^{\text{ref}}$  using the method of injecting currents of defined magnitudes. In a second and separate evaluation step, the transfer factors are determined only using field measurements at one current value (here, the largest possible  $I_0 = 30$  A in the interest of maximising the signal-to-noise ratio). The coefficients determined (via the inverse problem and using the matrix  $\mathbb{A}(r, \theta_i)$ ), or more precisely the ratios of suitable combinations of coefficient ratios, can then be compared to those of a reference matrix calculated for the coordinate range defined by  $d_0 \in [5 \dots 12]$  cm and  $\varphi \in [178 \dots 182]^\circ$ .

The results for the application of the calibration procedure for a given combination of coefficient ratios are summarized in Table V.6. All possible combinations of ratios involving coefficients from the second to fourth order were tested. Since, for the given angular position of the array, the coefficients  $b_n$  have near-zero values, they are only used in the numerator of coefficient ratios. Ratio combinations involving the second order coefficient  $a_2$  significantly improved the precision, and amongst them, several combinations provided comparable precisions for the determination of the transfer factor  $k_{a_4}$ . The minimization of the difference between the reference matrix and the experimental coefficients is performed for a combination of  $\frac{b_3}{a_4}$  and  $\frac{a_2}{a_3}$ , which is an example of multiple combinations involving second to fourth order coefficients that result in comparable precision. In contrast to the simulation, the use of more ratios does not necessarily lead to an increased precision (in theory, the best precision is always equal to that of the combination involving all available coefficients). This can be explained by larger variations (e.g. due to noise, especially for the second order) and thus a reduced precision in coefficient values for the experimental case. The calibration returns values for the array-to-conductor distance  $d_0$ , which can only be compared to the targeted set values  $d_0^{\text{set}}$  which were established manually with a precision of  $\pm 0.05$  cm. The values returned by the calibration procedure all fall within the resulting interval, so that this distance could be determined with the same precision. This result is also interesting in view of alternative applications of the sensor array, since it allows for a characterization of the source (position) based on the coefficient values. The mean value and standard deviation of the reconstructed angular position define an interval  $\varphi_0 = (180.2 \pm 0.1)^\circ$  for the 13 positions, and the true

---

CHAPTER V. EXPERIMENTAL RESULTS

---

Calib. results	Set values $d_0^{\text{set}}$ [cm]											
	5.0	5.5	6.0	7.0	7.5	8.0	8.5	9.0	9.5	10.0	10.5	11.0
$d_0$ [cm]	5.01	5.51	6.02	6.97	7.49	8.05	8.55	9.05	9.55	10.08	10.54	11.10
$\varphi_0$ [deg]	180.3	180.3	180.2	180.0	180.2	180.1	180.3	180.2	180.4	180.1	180.1	180.2
$k_{a_4}$	-55 983	-36 240	-24 454	-12 764	-9 399	-6 872	-5 324	-4 180	-3 336	-2 660	-2 206	-1 783
$k_{a_4}^{\text{ref}}$	-56 956	-36 463	-24 570	-12 776	-9 397	-6 813	-5 250	-4 104	-3 256	-2 567	-2 115	-1 695
$\Delta k_4$ [%]	-1.7	-0.6	-0.5	-0.1	0.02	0.9	1.4	1.8	2.5	3.6	4.3	5.2

**Table V.6:** Result of calibration for measurements at different set values  $d_0^{\text{set}} \in [5, 5.5 \dots 11] \pm 0.05$  cm (the missing point at  $d_0 = 6.5$  is due to a measurement error) and  $\varphi_0^{\text{set}} = (180 \pm 0.5)^\circ$  and using a combination of the coefficient ratios  $\frac{b_3}{a_4}$  and  $\frac{a_2}{a_3}$ . The reference matrix is calculated for  $d_0^{\text{set}} \in [4.5 \dots 120]$  cm and  $\varphi_0 \in [178 \dots 182]^\circ$ , with step sizes of 0.07 mm and  $0.24'$ , respectively. The reference values for the fourth order transfer factor  $k_{a_4}$  are calculated from DC sweeps at each position and subsequently compared to the values obtained from the calibration method.

value should thus also be part of this range. As explained above, reliable reference values for the transfer factor  $k_{a_4}$  can be obtained from a DC sweep at each position and these are provided in the table. When compared to the values obtained from the calibration procedure, a distinct increase in error can be observed as the array is moved further away from the conductor, even if this tendency is less distinct for  $d_0 < 8$  cm and an outlier is present at  $d_0 = 5$  cm. This increase can be explained by the fact that the fourth order contribution is strongest as the array is closest to the conductor and subsequently reduces as the array is moved further away (Chapter III). At larger distances, the fourth order coefficients, and consequently the transfer factor  $k_{a_4}$  obtained via the calibration method, are more susceptible to sensor noise or other perturbations. The objective of the calibration method is the determination of the transfer factor with an error below 0.5%, since this error contributes in full to the current determination precision. For the test series, this objective could only be met for three positions, all of which fulfil  $d_0 < 8$  cm, and in this range the error seems to be subject to random variations. While the good reconstruction of the array position is a very promising result that confirms the applicability of the calibration method, the insufficient precision in the transfer factors underlines the necessity for further refinement of the procedure. Furthermore, it is of paramount importance to guarantee the robustness of the calibration procedure by employing only orders that exhibit no or only very limited susceptibility to perturbations, since the procedure must be operational in the presence of adjacent conductors and/or other field sources. At this point, it is important to recall once again, that the result obtained above are strongly dependent on the sensor technology and configuration. If, in the future, the sensor technology can be replaced by one with an even better signal-to-noise ratio, or if it is possible to produce an array with sufficient sensors and an adequate radius (and/or position), to reliably detect the fifth order contribution (and

to use the fifth order coefficients in the calibration procedure), a noticeable improvement of the determination accuracy can be expected.

The application of the measurement principle to the measurement of DC magnitudes could thus be confirmed, while the precision and reproducibility proved to be strongly dependent on the installation conditions and calibration possibilities. A number of steps that can be undertaken to improve the performance of the 2D measurement array for precision DC measurements have been discussed throughout the presentation of the results above and will be summarized again at the end of this chapter. Before this can be done in a comprehensive manner, it is important to extend the application range to AC measurements, thus taking an essential step closer to the industrial application that serves as objective for this work.

### V.1.5 AC measurements

AC measurements were performed both using the identical setup as for the DC measurements presented above and also at the Nexans Research Facility (NRF) in Donchery, in order to perform measurements in a more complex environment, also using a complete three-conductor system, and to allow for comparison with reference sensors available on site. The first two-day test series in Donchery was performed at a very early stage after initial tests had only been completed at 15 Hz (due to the output impedance of the employed capacitor-input filters, which were consequently cleared for operation at 50 Hz). A second (three-day) test series was thus conducted three months later after further tests and development had been completed in the G2Elab laboratory. In correspondence to the chronological order of these measurements the AC measurement results are discussed in the following order below:

- Analysis of the **transfer factors** obtained by two different methods and compared to values obtained by DC sweeps. These results are based on measurements performed during the first test series at the Nexans Research Facility, for which two of the KEPCO DC sources utilized at G2Elab were taken along with the sensor arrays.
- Determination of attainable precision for the **two-conductor** setup at G2Elab.
- Results obtained during the second tests series at the Nexans Research Facility, using a **three-conductor system**.

These tests at the Nexans Research Facility allow for an evaluation of the sensor performance in a different, less controllable environment. The measurement setup is displayed in Fig.V.4. While the overall geometrical setup was conserved (perturbing conductors at  $x = \pm 40$  cm), other

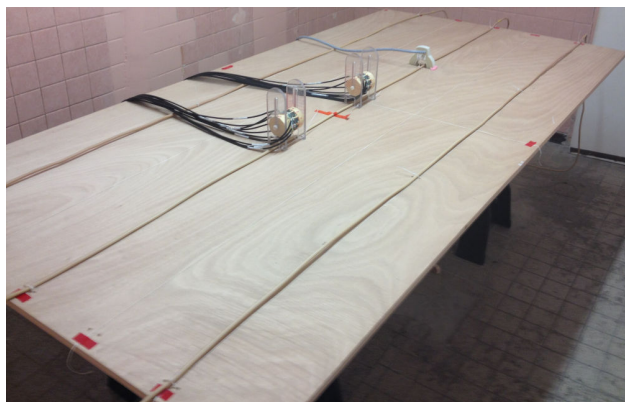


**Figure V.4:** AC measurement setup at Nexans in Donchery. The two 2D sensor arrays are placed above the central conductor and a perturbing conductor is situated at 40 cm on either side of the primary conductor. The PC for data acquisition, AC source and reference sensors are located in the adjacent room. A Nexans sensor based on the Rogowski principle is positioned in-line behind the 2D prototypes, around the central cable and is used for comparative measurements.

parameters changed, e.g. the cable material was less flexible, so that the cable paths were generally less straight and the positioning and orientation of the return conductors were also less optimal. Most importantly, although the 2D sensor arrays and conductors were again placed on a table, the positioning of the sensor arrays was not as precise as with the specifically designed fixations employed at G2Elab. Since the tests were performed over a period of two or three days, respectively, the conditions must therefore be considered less stable. For all AC measurements,  $N_{\text{samples}} = 10000$  samples of the sensor data were acquired with a frequency of  $f_{\text{sampling}} = 10$  kHz, so that each acquisition (given combination of  $I_0$ ,  $I_1$  and, at the NRF,  $I_2$  and respective phases) lasted one second (50 AC oscillations).

### **Transfer factors (Nexans)**

After installation of the sensor arrays at the NRF, reference DC test confirmed the operability of the arrays, so that it was possible to proceed with the AC tests. The two possibilities of evaluating measurements made with the sensor array for alternating currents have been introduced in section III.5. A clear distinction between the two methods is possible based on the moment of the application of a fast Fourier transform (FFT) to the signals: as detailed above, the FFT can be performed either directly on the sensor signals ( $B_i$ ), or on the coefficient curves  $a_n(t)$  which are obtained from a pointwise application of the inverse problem for every moment  $t$  at which an acquisition is made. Both evaluation methods were applied to the measured magnetic field data.

Method	Transfer factors			
	$k_{a_1}$	$k_{a_2}$	$k_{a_3}$	$k_{a_4}$
<i>Array A</i>				
DC sweep	-16.3	141.1	-1615	23 052
AC sweep	-16.3	140.8	-1613	22 885
AC direct	-16.3	141.5	-1620	22 934
<i>Array B</i>				
DC sweep	-16.3	141.9	-1709	25 948
AC sweep	-16.2	141.2	-1674	25 700
AC direct	-16.2	141.6	-1710	25 838

**Table V.7:** Transfer factors  $k_{a_n}$  obtained during the test series at the Nexans research facility in Donchery using the three calibration method based on the injection of a known current. For either array the transfer factors are determined using DC/AC sweeps or from a single AC measurement (and a single current period).

The obtained results exhibit a high degree of correspondence. For the discussion below, the point-wise approach is selected, because it provides a greater level of detail and thus insight into the application of the measurement principle (due to the later point of application of a FFT during the evaluation process).

In the interest of following a test protocol with increasing complexity, the first measurements were performed with the primary conductor only. The main purpose of these measurements is again to determine the transfer factors: their knowledge then allows the examination of the effect of perturbing conductors.

In order to make the transition from coefficient values  $a_n(I_0)$  to current values  $I_0$  it is again necessary to know the transfer factors after installation of the array. Three methods were employed to determine the transfer factors for AC measurements:

- DC (sweep) calibration: calibration by injecting a known direct current after installation of the array (either before and/or during and/or after the AC measurements). The procedure is identical to that presented for the DC measurements above.
- Multi-value AC (sweep) calibration: using measurements at different AC magnitudes  $I_{0,rms} \in [2, 4 \dots 30]$  A. This approach uses the FFT results for a single current (no perturbations) and the procedure is otherwise analogous to the DC calibration. However, this method does not require the availability of a DC source.
- Instantaneous (direct) AC calibration: takes advantage of the variation of  $I_0$  during the AC cycle, i.e. in the range  $[-I_{0,max}, \dots, 0, \dots, +I_{0,max}]$ . In contrast to the sweep methods, the

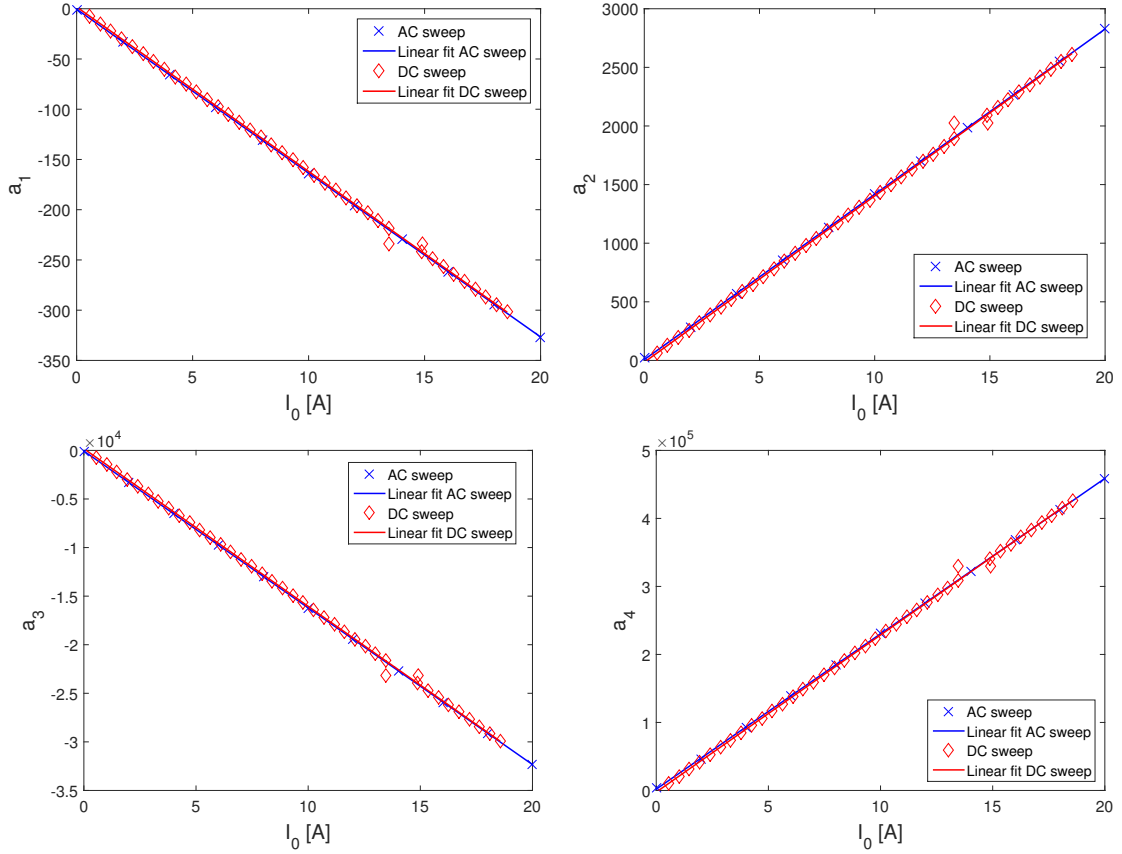


**Figure V.5:** Comparison of DC and AC sweep calibration using known current values for array A. The slopes of the curves  $a_n(I_0)$  correspond to the transfer factors  $k_{a_n}$ .

$I_0$  values are not equally distributed, due to the nature of the AC oscillation. The number of values for  $I_0$  in the given range is defined by  $f_{\text{sampling}}/f_{\text{AC}}$ , in this case  $10 \text{ kHz} / 50 \text{ Hz} = 200$  data points per period. This calibration method can be performed in a much short time frame  $< 1 \text{ s}$ . Here, one period (20 ms at 50 Hz) of the current variation was used to obtain the transfer factors during the laboratory tests. However, this method still requires a reference value for  $I_0$  and measurement without perturbations.

The results obtained for a given position after installation and using the various calibration methods are summarized in Table V.7 and the relations  $a_n(I_0)$  are shown in Fig. V.5 for the AC and DC sweep methods. For the two AC methods, the same set of measurement data is employed for the evaluation, wherein the direct approach is simply applied to the maximum current primary current magnitude only. A very good correlation can be observed in general. Some observations

can be made based on the relative variations between the methods. The overall correlation of the fourth order transfer factor, which is of primary interest for the geometrical selectivity and current determination precision, is good ( $\Delta k_{a_4} < 0.5\%$  for array A and  $< 0.5\%$  for array B). For the obtained results, the direct AC and the DC sweep method exhibit the best correlation, and the more surprising result is the deviation between the two AC methods, which were applied to the same measurement data. Since the direct AC method correlates well with the DC results, which have been confirmed in a larger number of repeated measurements, they can be considered more accurate. With respect to variations in the position of the array with respect to the conductor, and thus the transfer factors, the sensor array should, as discussed above, either be fixed securely with respect to the investigated conductor, or a calibration should be performed at a frequency that corresponds to or exceeds the time scale on which the variations take place. The larger values for  $k_{a_4}$  (and to a lesser extent for  $k_{a_3}$ ) for array B with respect to array A correspond to the results obtained at G2Elab, which were explained above by the effect of sensor misalignments.

Given the good correlation of the transfer factors obtained via a DC sweep or the direct AC method, the two determination methods are equally applicable, with the direct AC method providing the greatest ease of application (since one value for  $I_0^{\text{RMS}}$  is sufficient), thus presenting the method of choice for subsequent evaluations. The transfer factors determined in this way can then be used during the examination of the effect of a perturbing conductor on AC measurements. For this, the relative position  $d_0, \varphi_0$  of both sensor arrays are left unaltered and perturbing currents  $I_1$  (and  $I_2$  at the NRF) are injected into (a) conductor(s) at a distance of  $x = \pm 40$  cm to the primary conductor. The AC sources in both laboratories also allow for a control of the relative phase between the conductors. The results obtained with two- and three-conductor systems, at the respective laboratories, are presented in the following.

### **Current determination – two-conductor system (G2Elab)**

A CHROMA 3-Phase Programmable AC Source was used to generate alternate currents of varying magnitude and phase difference for the primary and perturbing conductor of the G2Elab setup. The shunts were again employed as references for the current flow.

Measurements were performed at various phase differences, frequencies and magnitudes. The conclusions for the measurement principle correlate for different measurement conditions. Therefore, in order to emulate real grid conditions, the results at 50 Hz with phase difference of  $\Delta\phi = 120^\circ$  are provided in Fig. V.6 (left). The results obtained by both evaluation methods (FFT and point-by-point) described in section III.5 exhibit a near-perfect degree of correlation and confirm that a precision of  $I_0^{\text{RMS}} \leq 0.5\%$  can be obtained using third and fourth order coefficients. As

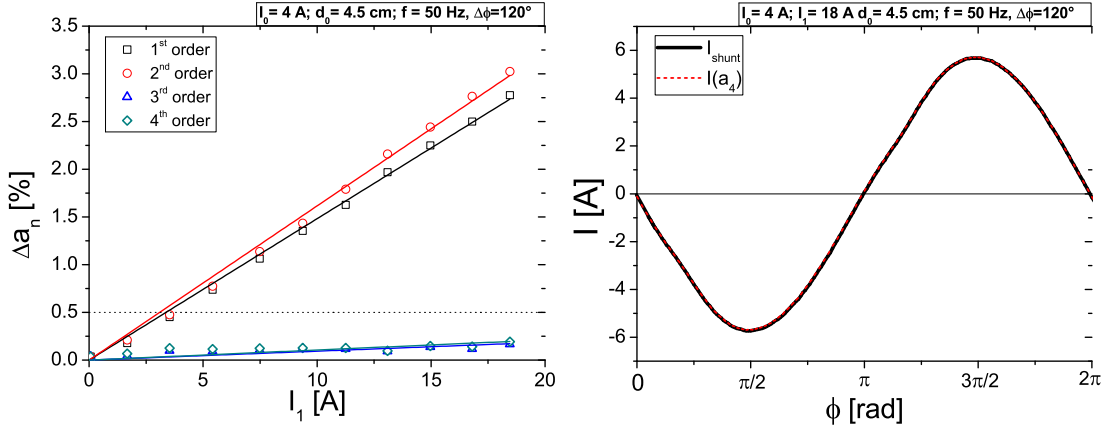


**Figure V.6:** Current reconstruction precision for two-conductor AC system. Left: coefficient error using the different orders and increasing perturbing conductor, for  $f = 50$  Hz,  $\Delta\phi = 120^\circ$ . Right: reconstruction of the primary current using the pointwise evaluation method and fourth order coefficient (dashed red line) and reference curve measured by shunt (solid black line).

described in the introduction of the evaluation methods, both methods reject the DC component using a FFT, but this is only applied at the last step for the point-by-point approach (on the curves  $a_n(t)$ ).

The results also exhibit very good correlation to simulations of the measurement setup. A very notable observation with respect to the DC measurements, is that the lower orders provide significantly enhanced precision, remaining below 4% for all orders and the maximum perturbing current for the standard phase difference. For other phase differences the behavior is slightly modified but the general observation remains unaltered and also corresponds to simulation results. Furthermore and in contrast to the DC results, a strong similarity can be observed in the attainable precisions using the first and second as well as for the third and fourth orders. As shown in Fig. V.6 (left), for a given phase difference, the third order may provide results of comparable qualities as the fourth order, however, the latter always provided superior precision and is more robust to variations in measurement parameters or environment.

As discussed above, the point-by-point, evaluation method provides a high temporal resolution, corresponding to the number of measurement points, at the price of a larger computing effort. The reconstruction of one AC oscillation using the fourth order coefficient is provided in Fig. V.6 (right). The results show that the current waveform, as measured for reference using the shunt, can be reconstructed perfectly even in the presence of a significant perturbation ( $I_0^{\text{RMS}} = 4$  A and  $I_1^{\text{RMS}} = 18$  A). It should be noted, that the fluxgate sensor suffer an intrinsic phase offset (typically

$\Delta\phi = 8 - 10^\circ$ ), which is, however, constant and corrected for the displayed results.

Given the confirmation of the applicability of the measurement principle for a two-conductor AC system, further validation of the approach can be obtained through probing of the laboratory prototypes in increasingly complex and unfavorable measurement conditions. In this interest, the 2D prototypes were installed for a second test series at the NRF, where the less controllable conditions described above and the availability of a second perturbing conductor provided the desired increased complexity and better approximation of on-site conditions. These results of this test series are presented below.

### **Current determination – three-conductor system (Nexans)**

For the second test series, the 2D prototypes are installed at  $d_0 = 7.5$  cm (to also allow for measurements up to RMS currents of 60 A without saturating the fluxgate sensors) above the central conductor with the perturbing conductors at  $x = 40$  cm on either side. The current magnitudes and phases are continuously monitored using a LEM reference sensor<sup>1</sup> on each conductor.

The results obtained with array A, using the fourth order coefficient and for increasingly strong perturbing currents  $I_1 = I_2$  at the typical phase differences of  $\Delta\phi = \pm 120^\circ$ , and for different primary currents  $I_0$  are provided in Fig. V.7. As for the DC measurements and the two-conductor AC setup, the results confirm that the primary current value can be obtained with very high precision even at perturbing currents that are up to eight times stronger than the primary current. An offset in the attainable precision values can be observed for low perturbing currents and increases with the magnitude of the primary current  $I_0$ . This offset does not correspond to simulations and cannot be explained within the given theoretical framework and its origin is possibly attributable to experimental artifacts or an imprecision in the evaluation process. Repeated measurements are necessary to identify and eliminate the origin of this (systematic) error, which, for the given measurements, increases with the primary current magnitude. For the assessment of the measurement principle, the more significant conclusion that can be drawn from Fig. V.7, is that the precision obtained with the fourth order coefficient exhibits very weak to no dependence on the magnitude of the two perturbing currents, with the extent of variation (if any significant slope is observable at all) depending on the magnitude of the primary current.

Since the results obtained outperform the expected values by far, it is absolutely necessary to perform repeated measurements before a conclusion can be drawn. These measurements will be completed at G2Elab, where the control over individual parameters and the overall measurement

---

<sup>1</sup>Model: IT1000-S/SP1 ULTRASTAB, precision (linearity, offset, temperature coefficient) < 60 ppm

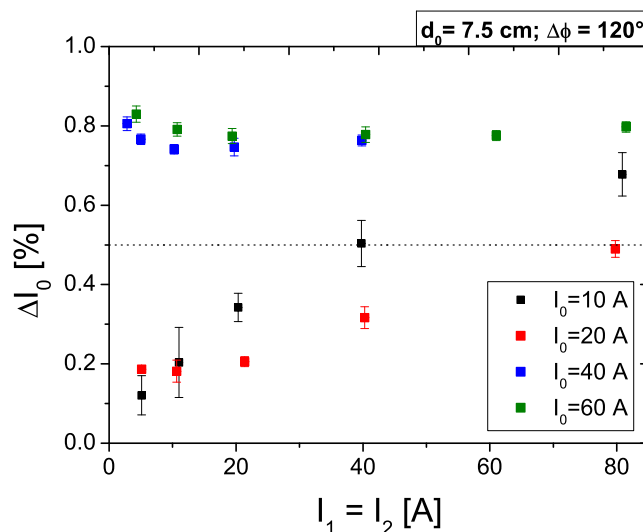


**Figure V.7:** Precision of primary current determination using the fourth order coefficient  $a_4$  for the evaluation of the three-conductor system at the NRF. The conductors are separated by  $x = 40$  cm and the results provided for different primary current values  $I_0$  and increasing perturbing current values  $I_1 = I_2$  (all values provided are RMS values).

conditions will be enhanced. The change of measurement setup and conditions (conductors, AC source, ambient field, etc.) could already lead to the elimination of a possible source of error for the results obtained at Donchery. Prior to the evaluation of these additional measurements, it is not possible to draw conclusions concerning the attainable precisions for AC determinations.

## V.2 3D measurement array

Testing of the 3D measurement principle and prototype was performed analogously to the 2D procedure and thus initially using the simplest measurement conditions involving straight conductor paths and direct current. These measurements were performed toward the very end of this thesis work and their results thus conclude the presentation of the experimental work.

As explained in Ch. IV, only one axis of the 30 fluxgate sensors is employed and the spherical coordinate system with its origin at the center of the sphere (and reconstruction volume) is chosen so that all sensors axes, oriented tangentially on the five parallel circles, measure the component  $B_\phi$  of the field. Therefore, in order to measure the magnetic field of the straight primary conductor, the array is positioned horizontally above the current flow, so that each circle, and active sensor axis, is in a plane perpendicular to the conductor in which the magnetic field is created. A

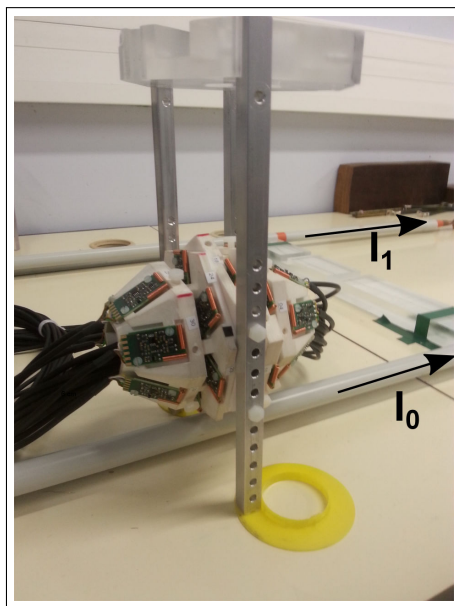


**Figure V.8:** Placement of the 3D prototype at  $d_0 = 6$  cm above the primary conductor  $I_0$ , with the perturbing conductor  $I_1$  at a lateral displacement of 40 cm, for DC measurements. The 30 active fluxgate axes, positioned tangentially on each of the parallel circle, measure the components in the plane perpendicular to the current flow.

photograph of the setup is provided in Fig. V.8.

For the evaluation of the results, it is initially necessary to determine the coefficients with the strongest contribution to the spherical harmonics decomposition for each order, i.e. the spherical harmonic function which provides the dominant contribution to the reconstruction of the field. This behaviour was presented in the form of a coefficient spectrum for both straight and deformed conductor paths in Fig. III.24 of the theoretical discussion. The specific degree of the function for each order depends on the relative positioning of the array with respect to the field and the choice of origin and orientation of the spherical coordinate system.

The error induced in the respective coefficient values as a result of a perturbing current  $I_1$  is presented for primary currents of  $I_0 = 5$  and 2 A in Fig. V.9. Measurement and evaluation confirms that, as for the 2D case, higher orders exhibit a reduced susceptibility to the perturbation and the error in the third and fourth order coefficient values remains below 0.5 % up to  $I_1 = 4 \cdot I_0$  for the given geometry, characterized by  $d_1/d_0 = 6.7$ . For a weak primary current of  $I_0 = 2$  A, the fourth order coefficient error is still below 0.8 %, even when the perturbing current is ten times

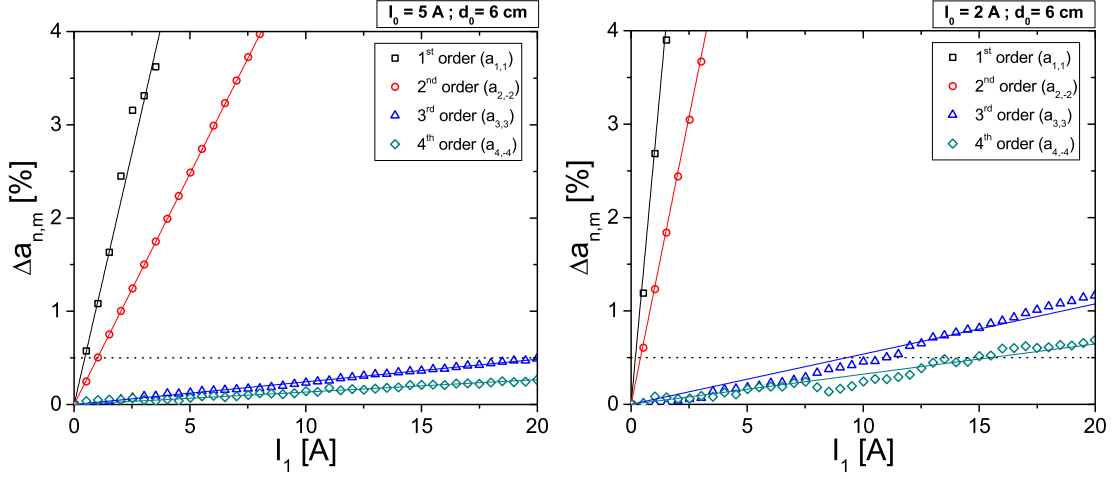


**Figure V.9:** Coefficient error for 3D prototype and DC measurements. The primary conductor is carrying a current of  $I_0 = 5\text{ A}$  (left) and  $2\text{ A}$  (right), respectively, and the perturbing current  $I_1$  (at  $x = 40\text{ cm}$ ), is increased to four, respectively ten, times that value. The coefficient with the strongest contribution is evaluated for each order.

stronger. The 3D results therefore confirm the enhanced geometrical selectivity provided by higher order coefficients and the applicability of the measurement principle. The prototype is however not optimized for application with a linear conductor, for which the 2D solution remains the best suitable solution, especially with respect to its simplicity.

### V.3 Conclusion and Perspectives

The following central results were obtained during the tests with the laboratory prototype:

- **2D – DC measurements**
  - The linear dependence  $a_n(I_0)$  of the coefficient values on the primary current was confirmed and the determination of the transfer factors  $k_{a_n}$  that establish the link between the development coefficients was possible using the DC sweep calibration method and reference current measurements.
  - With the determined transfer factor  $k_{a_4}$  it was possible to determine the current  $I_0$  with a precision of  $\Delta I \leq 0.5\%$  even with a perturbing current of significantly higher magnitude  $I_1 = 10 \cdot I_0$  for a setup providing  $d_1/d_0 = 6.7$  ( $d_0 = 6\text{ cm}$ ). An excellent reproducibility was observed for measurements at this precision. This confirms

- the strong geometrical selectivity of the measurement method, which is based on the exploitation of higher order contributions to the decomposition of the magnetic field.
- At larger distances ( $d_0 = 11$  cm) from the primary conductor and a reduced rejection factor  $d_1/d_0 = 3.8$  the geometrical selectivity is reduced accordingly and, together with the deteriorated signal-to-noise ratio and lower magnitude of the fourth order contribution, results in larger errors in the current determination, typically a few percent  $\leq 5\%$ , but up to 7% for low primary currents  $I_0 = 2$  A. At this (sufficiently large) distance, the obtained transfer factors approach the analytical values and an even better correlation can be expected as the distance is increased further.
  - If the sensor arrays are placed close to the primary conductor (e.g.  $d_0 = 6$  cm), the experimental coefficients do not correspond to the analytical formulation, since the maximum decomposition order of  $N = 4$  is insufficient for a precise reconstruction of the actual magnetic field. However, it was possible to demonstrate that, as long as  $a_n(I_0)$  is a linear relationship (as confirmed by the experiments), it suffices to determine the transfer factors  $k_{a_n}$  by means of a suitable calibration method, in order to allow for the application of the method with the necessary precision.
  - Besides the DC sweep calibration which relies on the injection of a known current as reference, the applicability of a current-independent calibration method using ratios of coefficient values was demonstrated. Without perturbing currents, it was possible to calibrate the transfer factor  $k_{a_4}$  to within a precision of  $\leq 1.8\%$  for positions  $d_0 \leq 9$  cm, and to  $\Delta k_{a_4} = 0.5\%$  at  $d_0 = 6$  cm. These results were obtained without the consideration of fabrication and positioning errors  $\Delta r_i, \Delta \vartheta_i$  or misalignment angles  $\Delta \alpha_i, \Delta \beta_i$ . Their determination and inclusion in the reference matrix offers a potential for improvement in the precision in the calibration method. The objective remains to achieve similar calibration precisions using third and fourth order coefficients only, in order to increase the geometrical selectivity of the calibration method and to allow for its application in the presence of perturbing currents (which, for the given setup, have a sufficiently strong impact on the second order coefficient, to render it useless for the calibration).
  - The fabrication of a second 2D prototype demonstrated that the transfer factors  $k_{a_4}$  and their reproducibility can vary significantly due to variations in fabrication and/or sensor placement precision. The misalignment of individual sensor axes was identified as a possible explanation for this and the analysis was supplemented by an inversion

with a nine-sensor subset. The misalignment of a single sensor (no. 5) was identified as a possible source of error, however, further array characterization is necessary to allow for a final conclusion on this subject. The range of possible fabrication errors will also depend on the specific fabrication method.

- **2D – AC measurements**

- Different test series, both under well-controlled conditions at G2Elab and under more complex conditions at the Nexans Research Facility confirmed the applicability of the measurement principle for AC measurements. The obtained results exhibit very good correlation with simulations and confirm that higher order coefficients provide enhanced geometrical selectivity between individual conductors. It was possible to validate the performance of the 2D prototypes for conditions that approach on-site parameters, i.e.  $f = 50$  Hz,  $\Delta\phi = \pm 120^\circ$  (while being equally applicable at other phase differences and frequencies). The maximum current magnitude is limited by the employed sensor technology but transition to stronger current magnitudes (using a suitable sensor technology) is direct and does not affect the applicability of the approach.
- Two different methods for the determination of the transfer factors were employed and showed very good correlation between each other and to reference DC measurements, and the direct AC methods allows for a quick and repeated determination of the transfer factors.
- Two tests series at the Nexans Research Facility demonstrated that the prototypes provide a good robustness for application in less well-defined, complex environments, indicating the promising potential for extension to the application of industrial prototypes.

- **3D – DC measurements**

- First tests using the 3D prototype with two straight DC conductors confirm the applicability of the 3D measurement principle with its respective formulations and the solution of the more extensive inverse problem employing 30 sensors and 24 coefficients. It was again possible to demonstrate the enhanced geometrical selectivity of higher order contributions. For the straight conductor system the 3D array is unnecessarily complex in comparison to the 2D array, but this setup allowed for a validation of its functionality, thus laying the groundwork for a direct transfer to more complex

conductor systems, for which the increased robustness and applicability will come into effect.

Overall, it can be concluded, that the presented results validate the measurement principle and confirm its applicability to current measurements in multi-conductor systems, for which an enhanced geometrical selectivity is obtained while providing the desired facilitated installation options. Further development is required to reach a stage of industrial application, but, although this will certainly encounter challenges along the way, it can be considered a more straight forward step given the groundwork of a validated measurement principle.

The above summary and discussion of the results does not mark the end of the measurement efforts. It rather presents a milestone at the end of three years of work on the subject. The SOGRID project ends in August 2016 and will see further measurement series, e.g. temperature-dependent measurements or completion and extension of the misalignment analysis. Together with the results presented above these measurements should serve to lay the basis for the development of a new generation of prototypes, scaled to industrial demands. The further improvement of the calibration method will also remain a pivotal criterion for the success of the measurement method. The confirmation of the enhanced geometrical selectivity obtained above for DC measurements using the fourth order coefficient allowed for an experimental proof of concept for the simulated result and should serve as a benchmark and motivation for the further development of the sensor solution.

# Conclusion and Outlook

---

## VI.1 Conclusion

In the introduction of this thesis, the necessity for the development of an innovative current sensor for the (smart) electrical grid was motivated in a top-down manner based on the evolution of the power grid in recent years. In an effort to respond to the challenges posed by a complexified grid, the sensor development was included as a separate task in the SOGRID project, with the objective of creating a new generation of current sensing solutions. The objectives and time frames defined in the SOGRID project guidelines, therefore, serve as a first basis of valuation for the completed work. Since a project that brings together partners from the world of university research and the industry has the clear objective of providing mature technological solutions, which are ready for installation and application in the grid, the industrialization of a specific solution serves as a decisive benchmark. In order to place the development work presented in this thesis back into the context of the SOGRID project and its value for smart grids in general, the technological readiness scale will be employed as a common method for the assessment of technological developments. An example of this is provided in Fig. VI.1.<sup>1</sup> The scale extends from the observation of the basic principles that govern a technology towards its deployment and passes through nine well-defined stages.

The SOGRID project was set out for a duration of three years, was initially scheduled to over-

---

<sup>1</sup>Originally introduced by NASA for space programs, the technological readiness level (TRL) is now also used by the European Commission in the context of research in general for the assessment of research projects, particularly those part of the research program Horizon 2020.

## VI.1. Conclusion

---



**Figure VI.1:** Technological readiness scale based on the definition of the European Commission.<sup>[45]</sup>

lap closely with the timeline of this thesis and will end six months after the submission of this manuscript. In the definition of the project task pertaining to the current sensor development, the objective was initially to adapt, supplement or extend existing MEMS sensor solutions for applications in smart grids. This approach would have allowed for a development based on technology concepts that have already been employed and tested (at G2Elab) or for which at least a substantial knowledge base could have been consulted. Consequently, it would have been possible to pass through the (usually time-consuming) first two stages of the TRL in a significantly compressed period by basing the development of a novel solution on existing concepts and procedures and to consequently advance further on the scale. In this case, it would have been feasible to reach level nine by the end of the project.

However, the refocusing of the development efforts from the adaptation of existing MEMS technology to smart grid applications towards the development of an innovative current sensor meant that the problem would now be tackled at its very root. This decision was made in close exchange with Nexans as the industrial project partner, thus ensuring that these efforts meet the current and/or future demands for the management of the grid infrastructure.

With this shift of focus, the development thus started at the lowest TRL. This also explains the shift between the motivation of the work in a top-down manner in the introduction to the bottom-up presentation and development of the measurement method in the following chapters. The presentation of the measurement principle, the sensor technology and configuration and the experimental results follows the first four TRLs and presents fundamental research, while keeping track of the intended application as a central element to all considerations and decisions. Inevitably, the shift

in development objective also results in a re-definition of the timeline for this specific task. Since all TRLs must be completed, including the time-consuming first levels, it was immediately clear that the industrialization of the newly proposed innovative sensor could not be completed within a three-year time span. As noted above, the submission of this thesis marks an intermediate milestone in the project timeline and can be taken as an opportunity to assess the state of development based on the TRL. Since two prototypes have been developed for different applications (2D and 3D for linear and non-linear conductor paths), it is necessary to evaluate them individually, although their developments show different degrees of transferability of the results.

In Chapter III, the basic measurement principles were introduced for both the 2D and 3D approaches and the attainability of the critical function, i.e. the increase in geometrical selectivity using the spatial harmonics decomposition, was proven in theory. Both the 2D and 3D solution have thus completed the third TRL. Furthermore, prototypes have been designed and fabricated for both cases thus preparing the following stages.

For the 2D and 3D prototype, the measurement principle and implementation have been confirmed for DC measurements and the operating ability was established. For these measurements, it can thus be concluded that the 2D and 3D (laboratory) prototypes have completed TRL 4 ( $\Delta I_0 < 0.5\%$  and  $0.8\%$ , respectively, for different degrees of perturbation, up to  $I_1 = 10 \cdot I_0$ ), although the tests conducted for the 2D prototype are more extensive. For DC measurements, the prototypes therefore provide the necessary geometrical selectivity and meet (2D) or come very close to (3D) the precision demands set out for the measurement task in the introduction of this thesis. For the 2D prototype, an analysis of the reproducibility of the measurement results with a second sensor array and a study of possible sources of errors were also performed and provided a possible explanation for the observed deviation between the two prototypes.

The DC measurements with the 2D arrays also confirmed the applicability of the developed current-independent calibration method for the transfer factors  $k_{a_n}$  and allowed for their determination at the required precision for small array-to-conductor distances. This method composes an integral part of the measurement method, since it provides the necessary robustness and applicability for industrial measurement tasks. For the given 2D laboratory prototypes, the calibration method still lacks sufficient geometrical selectivity for applicability under strong perturbations. Possible points of improvement include a more detailed characterisation of the 2D array, as it was already performed for possible sensor misalignments for both arrays, or the development of sensors conceived to measure larger relative magnitudes of higher orders (adaptation of array radius and relative position) or additional higher orders.

The evaluation of the AC measurements allowed for a current determination with a similar

precision as for the DC measurements, even for large perturbations  $I_1 = 6 \cdot I_0$ . The geometrical selectivity which is achievable for AC measurements, was confirmed by repeated measurements at different phase differences in two- and three-conductor systems. The feasibility of AC measurements using the developed measurement principle and the two evaluation methods was thus successfully demonstrated and provides the basis for the two fundamental measurement tasks for AC grid operability: precise measurement of  $I_{\text{RMS}}$  and fault detection.

With the ranking of the measurement methods with respect to technological readiness, the next steps towards an industrialization also become apparent. The 3D prototype must still prove its worth with AC measurements and, in contrast to the 2D solution, will also be tested with deformed cable paths. Based on the DC results, the transfer of the 3D method to these different measurement environments can be considered straightforward, although the implications of each one should be assessed carefully. Meanwhile, the development of the 2D solution can already be focused towards the creation of an integrated system and an up-scaling towards grid applications using a suitable sensor technology (advanced prototype) and configuration (e.g. single PCB). This thesis therefore presents the fundamental proof of concept for the measurement method and the advanced prototype for either model can be compared to the pilot system designated in the TRL.

When it comes to an assessment of the required time for the remaining development stages, the complexity of the innovative measurement principle must also be kept in mind. The discussion in the previous chapters have already underlined the fact that careful examination and analysis are necessary to obtain a firm grasp on the multi-parameter measurement method, which then allows for the development of a robust and reliable solution, ready to be deployed and to provide the desired precision in electrical grids. Furthermore, the possibility and means of installing the sensors in the electrical grid, and the further development of the essential calibration method are also decisive factors for the degree of geometrical selectivity and robustness that the proposed solution can provide.

To conclude the work presented above at this point in time, the focus is shifted again to the technological readiness of the current development and prototypes. In March 2016, the experimental phase for the 2D prototype has reached two-thirds of the period that will end with the SOGRID project, while the setup of the 3D prototype has just been completed, so that the measurements with this array can now proceed. This experimental phase of this project task is thus still in a very active state and multiple measurement series are scheduled for the next weeks and months, including further AC measurement series (especially with the 3D prototype measurements), the experimental verification of the calibration method, etc. The theoretical framework and discussion of state-of-the-art sensor technologies provided in this manuscript, along with the presented

experimental results and means for array characterisation can be regarded as a complete toolbox for the implementation and analysis for future sensor development and testing.

The next steps detailed above present a form of task list for the following next months of development, which serve to raise both prototypes further up on the TRL scale. With the framework provided above and the know-how accumulated over the past three years, these steps towards industrialization are rather intuitive. However, to complete the outlook at this point, it is also meaningful to touch on some points that have been identified as promising development possibilities during discussions on this task.

## VI.2 Perspectives

An option that should definitely be explored further is the combination of the measurement results obtained by the sensor arrays positioned at each conductor respectively. As detailed above, while high order coefficients are exploited to obtain precise measurements without the influence of perturbing currents, lower order coefficients contain information on the position and current magnitude of the other conductors. It is therefore of interest, to combine the results from each array in order to improve the overall precision. This solution would add a post-processing stage to the evaluation method and the feasibility would thus depend strongly on the requirements (memory, processing-power, cost, etc.) for suitable application-specific integrated circuits (ASICs, cf. TRL 5 and 7).

Another approach is the improvement of the coefficient determination accuracy or the reduction of the required sensor number and configuration complexity using Bayesian methods. These have previously been employed at G2Elab to reduce the number and spatial distribution of required sensors for the characterization of magnetic fields in cars.<sup>[40]</sup> The approach is based on the introduction of *a priori* information into a Bayesian approach to the inverse problem. This can significantly reduce the number of required measurements and increase the accuracy of existing measurements through further data processing steps. Since it can be expected that the measurement geometry will be well-defined for sensor installation in the grid, the quantity and quality of the *a priori* information should be high and this method therefore presents a promising approach.

Concerning the transition from laboratory to industrial prototypes, it is important to note two central aspects: the measurement principle will remain intact and it is (only) necessary to scale-up the solution to suit the larger field magnitudes and, at the same time, the measurement conditions (primarily the geometry) will change and are expected to be subject to larger variations over time (e.g. due to temperature effects). The modified measurement problem requires two principal

modifications: the selection of a suitable sensor technology for the higher field range, which also provides a resolution and precision that allow for the determination of the required order, and the analysis of the robustness of the measurement method under these new circumstances. Both questions should be answered in a detailed feasibility report that is completed before the transition is put into effect. The informative value and reliability of such report will profit significantly from a precise definition of sensor installation conditions and parameters. The robustness analysis will likely result in the definition of necessary procedures, both for a one-time array characterisation after fabrication (for sensor array parameters  $r_i$ ,  $\theta_i$ , misalignments  $\alpha_i$ ,  $\beta_i$ , for the 2D case), and at a given periodicity over time (to account for possible fluctuations in the transfer factor  $k$ ).

Besides the selection of an adequate magnetic field sensor technology for grid applications, the change in relative inter-conductor distance  $x$  and the range of possible array-to-conductor distances  $d_0$  will likely result in the reassessment of the optimal sensor array radius  $r$  (based also on the dimensions of the sensors and the required order of decomposition/sensor number). Based on these new form factors, alternative sensor configurations should also be taken into consideration. In a first instance, the design of the sensor array as an ensemble instead of a combination of individual, commercially available, sensors will already provide an improvement. The manufacturer of the fluxgate sensors employed for this work (Stefan Mayer Instruments) has confirmed that it would be feasible to place six mono-axial sensors on a PCB with a radius as small as 2 cm. This could be an interesting alternative for the fabrication of future, smaller and simplified 3D prototypes, using only discs for sensor placement (the smallest disk radius is currently 3.4 cm). Of course, the radius cannot be reduced at will, since such a reduction entails a decrease in higher order contributions to the decomposition. Even more substantial improvements can be expected, if it is possible to replace the fluxgate sensor, which were very well-suited for the laboratory testing, with a more adapted sensor technology for the grid applications, e.g. the air coils presented in the outlook of Ch. II. If these allow for punctiform measurements of the magnetic field, they can enhance the attainable precision of the method, thanks to the rejection of field components at undesired frequencies.

Besides the presented short-term perspectives that will inevitably play a role in the development and advancement to a higher level of technological readiness, the following long-term potentials may also present promising paths of exploration at a given time.

### VI.3 Long-term technological advances

Two more profound/radical changes to the sensor technology or the measurement conditions are presented in the following. However, they would require extensive development and/or an overhaul of the measurement method; they should nevertheless be kept in mind as optional paths for the long-term.

- **Dedicated (harmonics) sensors:** The reduction in magnitude for higher orders is an inherent characteristic of the spatial harmonic decomposition for single punctual sources. It is also the predominant behaviour for the parallel conductors studied above. However, for the case of a deformed conductor path, the relative magnitude of orders is subject to local variations, i.e. at certain points on the sphere a higher order can show an 'unusually' strong contribution. These variations are enhanced with a non-linear conductor path. This local signature provides a very interesting opportunity for the current determination as it would allow for an even better discrimination between different field sources. The requirement for this is the possibility to measure a certain order locally. This would allow the placement of a sensor at a position where the conductor under investigation produces an 'irregularly' strong higher order contribution while external sources exhibit the 'regular' minor contribution of that coefficient which is further diminished by the distance. With the measurement principle at hand, it is only possible to determine an ensemble of coefficients  $a_{n,m}$  up to a specific order  $N$  and for a volume defined and limited by the sensor array dimensions (which are subject to the limitations explained above). In this respect, it may prove useful, to consult similar applications in other fields of research. For example, spherical harmonics and microphone arrays have been employed in acoustic signal analysis and the coefficient determination was improved by using circles of different radii within a plane, so that individual circles are adapted to identify a specific contribution.<sup>[46]</sup> It appears promising to also consider the use of circles or spheres with different radii for the current sensing solution, in order to selectively detect specific coefficients, since the analysis presented demonstrated the varying influence of different orders depending on the array radius  $r$  (and its distance  $d_0$  from the conductor).

Designs for dedicated coil sensors for the identification of specific components have previously been proposed and developed at G2Elab by Vincent *et al.*<sup>[47]</sup> Such dedicated coil sensors offer the possibility for a significant reduction of the sensor complexity and price.

- **Deformed cable cross-section generating "custom" harmonics:** A further extension of the

approach described above involves the deliberate controlled shaping of the local variations (and thus contributions) of specific coefficients to further enhance the differentiation capability concerning different coefficients and thereby the field from different sources. This approach is especially appealing because it potentially allows for a firm control of the shape of the harmonic signature while being of distinctly novel character. The application of the spatial harmonic decomposition would be identical to that detailed above, since only the structure of the magnetic field is altered in this approach. Further pursuit of this approach would require detailed study of the magnetic field patterns created by conductors with deformed cross-sections of various shapes, and the analysis of possible sensor placement in recesses specifically created in the conductor path (in accordance with constraints imposed by the electric field and cable fabrication standards and technology). Based on discussion with the industrial partner Nexans, this approach has been deemed a technically possible option.

The two approaches for future modifications of the sensing principle or measurement conditions present steps that can either be considered to extend beyond the nine TRLs if the basic measurement principle remains unaltered, or to present an independent development starting at or near the bottom of a separate process that can be divided in TRLs.

---

## Bibliography

---

- [1] de Régulation de l’Energie, C. “Définition des Smart grids.” (2015). URL <http://www.smartgrids-cre.fr/>.
- [2] Covrig, C. F., Ardelean, M. *et al.* “Smart Grid Projects Outlook 2014.” Technical report, European Commission Joint Research Centre (JRC) (2014). doi:[10.2790/22075](https://doi.org/10.2790/22075). URL <http://ses.jrc.ec.europa.eu/smart-grids-observatory>.
- [3] “The Smart Grid: An Introduction.” Technical report, Litos Strategic Communication for U.S. Department of Energy (2015).
- [4] Ripka, P., Kaspar, P. and Saneistr, J. “Geometrical selectivity of current sensors.” *PRZEGLAD ELEKTROTECHNICZNY (Electrical Review)*, 5a:pp. 38–39 (2012). URL [pe.org.pl/articles/2012/5a/11.pdf](http://pe.org.pl/articles/2012/5a/11.pdf).
- [5] Ziegler, S., Woodward, R. *et al.* “Current Sensing Techniques: A Review.” *Sensors Journal, IEEE*, 9(4):pp. 354–376 (2009). ISSN 1530-437X. doi:[10.1109/JSEN.2009.2013914](https://doi.org/10.1109/JSEN.2009.2013914).
- [6] Ripka, P. “Electric current sensors: a review.” *MEASUREMENT SCIENCE & TECHNOLOGY*, 21(11):pp. 1–23 (2010). ISSN 0957-0233. doi:[10.1088/0957-0233/21/11/112001](https://doi.org/10.1088/0957-0233/21/11/112001).
- [7] (PEM), P. E. M. “PEM datasdata - RCTi-3ph - Thin, flexible, clip-around, AC current transducer.” Online, [http://www.pemuk.com/Userfiles/RCTi-3Phase/RCTi3ph\\_0511.pdf](http://www.pemuk.com/Userfiles/RCTi-3Phase/RCTi3ph_0511.pdf).
- [8] Hauser, H., Stangl, G. *et al.* “Magnetoresistive Sensors.” *Preparation, Properties, and Applications of Thin Ferromagnetic Films*, pp. 15–27 (2000). doi:[10.1007/BF03159608](https://doi.org/10.1007/BF03159608).
- [9] Asfour, A., Yonnet, J.-P. and Zidi, M. “A high dynamic range GMI current sensor” *Sensor Technology, Journal of*, Vol.2 No.4 (2012). doi:[10.4236/jst.2012.24023](https://doi.org/10.4236/jst.2012.24023)

- [10] Webster, J. G. and Eren, H. (editors). *Measurement, Instrumentation, and Sensors Handbook*. CRC Press (Taylor & Francis Group), ISBN 9781439848838, 2nd edition (2014).
- [11] Ripka, P., Pribil, M. and Butta, M. “Fluxgate Offset Study.” *Magnetics, IEEE Transactions on*, 50(11):pp. 1–4 (2014). ISSN 0018-9464. doi:[10.1109/TMAG.2014.2329777](https://doi.org/10.1109/TMAG.2014.2329777).
- [12] Fermon, C. and Pannetier-Lecoq, M. “Électronique de spin et capteurs magnétiques.” *Reflète de la Physique*, 18:pp. 8–11 (2010). doi:<http://dx.doi.org/10.1051/refdp/2010002>.
- [13] Costa, F. and Poulichet, P. “Sondes pour la mesure de courant en électronique de puissance.” *Techniques de l'Ingénieur - Énergies | Convertisseurs et machines électriques*, D 3 085:pp. 1–18 (2005). URL <http://www.techniques-ingenieur.fr/base-documentaire/energies-th4/outils-d-analyse-en-electronique-de-puissance-et-metrologie-42278210/sondes-pour-la-mesure-de-courant-en-electronique-de-puissance-d3085/>.
- [14] Bazzocchi, R. and Rienzo, L. D. “Interference rejection algorithm for current measurement using magnetic sensor arrays.” *Sensors and Actuators A: Physical*, 85(1â3):pp. 38 – 41 (2000). ISSN 0924-4247. doi:[10.1016/S0924-4247\(00\)00321-6](https://doi.org/10.1016/S0924-4247(00)00321-6). URL <http://www.sciencedirect.com/science/article/pii/S0924424700003216>.
- [15] Di Rienzo, L., Bazzocchi, R. and Manara, A. “Circular arrays of magnetic sensors for current measurement.” *Instrumentation and Measurement, IEEE Transactions on*, 50(5):pp. 1093–1096 (2001). ISSN 0018-9456. doi:[10.1109/19.963165](https://doi.org/10.1109/19.963165).
- [16] Di Rienzo, L. and Zhang, Z. “Spatial Harmonic Expansion for Use With Magnetic Sensor Arrays.” *Magnetics, IEEE Transactions on*, 46(1):pp. 53–58 (2010). ISSN 0018-9464. doi:[10.1109/TMAG.2009.2027899](https://doi.org/10.1109/TMAG.2009.2027899).
- [17] Yakymyshyn, C., Brubaker, M. and Yakymyshyn, P. “Current Sensor.” (2007).
- [18] Bourkeb, M., Joubert, C. *et al.* “Device for measuring currents in the conductors of a sheathed cable of a polyphase network.” (2013).
- [19] Storkey, M. “Current sensor.” (2008). URL <http://www.google.com.ar/patents/EP1977257A1?c1=zh>. EP Patent App. EP20,060,792,399.
- [20] Kawase, M. “Electric current sensor.” (2002). URL <http://google.com/patents/EP1199573A3?c1=ko>. EP Patent App. EP20,010,124,870.

## BIBLIOGRAPHY

---

- [21] Hohe, H., Sauerer, J. and Weber, N. "Vorrichtung und Verfahren zur Strommessung." (2002). URL <http://google.com/patents/EP1114325B1?cl=de>. EP Patent 1,114,325.
- [22] Paprotny. "Self-powered MEMS Sensor Module for Measuring Electrical Quantities in Residential, Commercial, Distribution and Transmission Power Systems." (2010). doi:[10.1109/ECCE.2010.5617742](https://doi.org/10.1109/ECCE.2010.5617742).
- [23] Todaro, M. T., Sileo, L. and De Vittorio, M. *Magnetic Sensors - Principles and Applications*, chapter Magnetic Field Sensors Based on Microelectromechanical Systems (MEMS) Technology. InTech (2012). doi:[10.5772/36468](https://doi.org/10.5772/36468).
- [24] Bahreyni, B. and Shafai, C. "A Resonant Micromachined Magnetic Field Sensor." *Sensors Journal, IEEE*, 7(9):pp. 1326 –1334 (2007). ISSN 1530-437X. doi:[10.1109/JSEN.2007.902945](https://doi.org/10.1109/JSEN.2007.902945).
- [25] Leung, C. M. *Magnetolectric smart current smart current sensors for wireless condition monitoring applications*. Ph.D. thesis, The Hong Kong Polytechnic University (2012).
- [26] Paprotny. "MODELING, DESIGN AND FABRICATION OF (10 x 10 x 4 MM<sup>3</sup>) MEMS AC ENERGY SCAVENGER FOR SMART GRID APPLICATIONS." *PowerMEMS2010* (2011).
- [27] Leland. "Design and Fabrication of a MEMS AC Electric Current Sensor." (2008). doi:[10.4028/www.scientific.net/AST.54.350](https://doi.org/10.4028/www.scientific.net/AST.54.350).
- [28] Ettelt, D. *Conception and fabrication of a strain-gauge magnetometer*. Ph.D. thesis, University of Grenoble (2012). URL <https://tel.archives-ouvertes.fr/tel-00744722/>.
- [29] Coillot, C. and Leroy, P. *Magnetic Sensors - Principles and Applications*, chapter 3 - Induction Magnetometers Principle, Modeling and Ways of Improvement, Magnetic Sensors. InTech (2012). doi:[10.5772/38945](https://doi.org/10.5772/38945).
- [30] Ripka. *Magnetic Sensors and Magnetometers*. Artech House (2001).
- [31] Tumanski, S. "Induction coil sensorsâa review." *Measurement Science and Technology*, 18(3):p. R31 (2007). URL <http://stacks.iop.org/0957-0233/18/i=3/a=R01>.
- [32] Paperno, E. and Grosz, A. "A miniature and ultralow power search coil optimized for a 20 mHz to 2 kHz frequency range." *Journal of Applied Physics*, 105(7):07E708 (2009).

- doi:<http://dx.doi.org/10.1063/1.3072718>. URL <http://scitation.aip.org/content/aip/journal/jap/105/7/10.1063/1.3072718>.
- [33] Grosz, A., Paperno, E. *et al.* “Integration of the electronics and batteries inside the hollow core of a search coil.” *Journal of Applied Physics*, 107(9):09E703 (2010). doi:<http://dx.doi.org/10.1063/1.3337750>. URL <http://scitation.aip.org/content/aip/journal/jap/107/9/10.1063/1.3337750>.
- [34] Grosz, A., Paperno, E. *et al.* “A Three-Axial Search Coil Magnetometer Optimized for Small Size, Low Power, and Low Frequencies.” *IEEE Sensors Journal*, 11(4):pp. 1088–1094 (2011). ISSN 1530-437X. doi:[10.1109/JSEN.2010.2079929](https://doi.org/10.1109/JSEN.2010.2079929).
- [35] Coillot, C., Moutoussamy, J. *et al.* “Improvements on the Design of Search Coil Magnetometer for Space Experiments.” *Sensor Letters*, 5(1):pp. 167–170 (2007). doi:[doi:10.1166/sl.2007.050](https://doi.org/10.1166/sl.2007.050). URL <http://www.ingentaconnect.com/content/asp/senlet/2007/00000005/00000001/art00044>.
- [36] Schmerber, L. *Identification et caractérisation de sources électromagnétiques. Application à a discrétion des moteurs de propulsion navale*. Ph.D. thesis (2007). URL <https://tel.archives-ouvertes.fr/tel-00128151v2>.
- [37] Nolting, W. *Elektrodynamik*, volume 3 of *Grundkurs Theoretische Physik*. Springer (2007). doi:[10.1007/978-3-642-37905-5](https://doi.org/10.1007/978-3-642-37905-5).
- [38] Rouve, L., Schmerber, L. *et al.* “Optimal magnetic sensor location for spherical harmonic identification applied to radiated electrical devices.” *Magnetics, IEEE Transactions on*, 42(4):pp. 1167–1170 (2006). ISSN 0018-9464. doi:[10.1109/TMAG.2006.872016](https://doi.org/10.1109/TMAG.2006.872016).
- [39] Schmerber, L., Rouve, L. and Foggia, A. “Original 2D cylindrical harmonics method for identification of the near magnetic stray field of electrical motor.” In “Electric Machines and Drives, 2005 IEEE International Conference on,” pp. 92–98 (2005). doi:[10.1109/IEMDC.2005.195707](https://doi.org/10.1109/IEMDC.2005.195707).
- [40] Pinaud, O. *Characterization, Modeling and Identification of magnetic field sources inside an electric vehicle*. Theses, Université de Grenoble (2014). URL <https://hal.archives-ouvertes.fr/tel-01122591>.

## BIBLIOGRAPHY

---

- [41] Keradec, J., Laveuve, E. and Roudet, J. “Multipolar development of vector potential for parallel wires. Application to the study of eddy currents effects in transformer windings.” *Magnetics, IEEE Transactions on*, 27(5):pp. 4242–4245 (1991). ISSN 0018-9464. doi:[10.1109/20.105038](https://doi.org/10.1109/20.105038).
- [42] McEwen, J. and Wiaux, Y. “A Novel Sampling Theorem on the Sphere.” *Signal Processing, IEEE Transactions on*, 59(12):pp. 5876–5887 (2011). ISSN 1053-587X. doi:[10.1109/TSP.2011.2166394](https://doi.org/10.1109/TSP.2011.2166394).
- [43] Alem, Y., Chae, D. and Kennedy, R. “Sparse signal recovery on the sphere: Optimizing the sensing matrix through sampling.” In “Signal Processing and Communication Systems (ICSPCS), 2012 6th International Conference on,” pp. 1–6 (2012). doi:[10.1109/ICSPCS.2012.6508014](https://doi.org/10.1109/ICSPCS.2012.6508014).
- [44] Rakhmanov, E. A., Saff, E. B. and Zhou, Y. M. “Minimal discrete energy on the sphere.” *Mathematical Research Letters*, 1(6):pp. 647–662 (1994). ISSN 1073-2780.
- [45] “Technology Readiness Level (TRL) Scale.” Online (January). URL <http://www.innovationseeds.eu/>.
- [46] Abhayapala, T. and Gupta, A. “Spherical Harmonic Analysis of Wavefields Using Multiple Circular Sensor Arrays.” *Audio, Speech, and Language Processing, IEEE Transactions on*, 18(6):pp. 1655–1666 (2010). ISSN 1558-7916. doi:[10.1109/TASL.2009.2038821](https://doi.org/10.1109/TASL.2009.2038821).
- [47] Vincent, B., Chadebec, O. and Schanen, J. “Multipolar expansion sensors for near field characterization.” In “Electromagnetic Compatibility - EMC Europe, 2008 International Symposium on,” pp. 1–4 (2008). doi:[10.1109/EMCEUROPE.2008.4786885](https://doi.org/10.1109/EMCEUROPE.2008.4786885).

# List of Figures

I.1	Evolution of the electrical grid topology. . . . .	2
I.2	Evolution of the number, distribution and type of power generation plants in Denmark, between the 1980s (left) and today (right) <sup>[3]</sup> . . . . .	4
I.3	Overview of the components of the SOGRID project and their installation sites in the distribution grid. . . . .	5
I.4	Schematic of an exemplary measurement setup. The sensor arrays (red spheres) for each (non-linear) conductor are connected to an ASIC to allow data combination and processing for increased precision. . . . .	9
II.1	The two categories of contactless current measurement methods. . . . .	15
II.2	<i>left</i> : Schematic of a Rogowski coil. <sup>[5]</sup> ; <i>right</i> : Schematic of a current transformer. . . . .	17
II.3	Schematics to illustrate the operating principle of magnetic sensors based on the Hall effect (left) and an AMR sensor using a Wheatstone bridge. . . . .	20
II.4	Effect of the field created by the excitation field on the magnetic flux density and permeability of the core, as well as the resulting voltage pulses picked-up by the detection coil. <sup>[10]</sup> . . . . .	23
II.5	Schematics of open-loop (left) and closed-loop (right) sensing configurations using magnetic field sensors in the gap of the magnetic core. . . . .	26
II.6	Sensing configurations for the application of spatial harmonics decomposition for current measurement. . . . .	31
II.7	<i>left</i> : Bourke et al. patent diagram; <i>right</i> : FieldMetrics patent diagram; . . . . .	32
II.8	Self-powered MEMS current sensor, including cantilever-based current sensor and AC energy harvester. <sup>[22]</sup> . . . . .	35
II.9	Frequency response (left) and equivalent magnetic noise spectrum (right) for search coils. <sup>[32]</sup> . . . . .	39

LIST OF FIGURES

---

III.1	Left: Conductor geometry of an (infinite) straight wire that creates a 2D magnetic field. Right: Exemplary conductor geometry creating an essentially 3D magnetic field. . . . .	43
III.2	Different application methods of spherical harmonic decompositions using either an internal or an external composition or a combination of both. . . . .	45
III.3	Contour plots of magnetic vector potential. . . . .	47
III.4	Illustration of the reconstruction for the magnetic vector potential using an increasing number of orders (from $N = 1$ to 4). . . . .	48
III.5	Contribution of each order (dotted lines) to total magnetic flux density (solid line) along circular sensor array path in 2D for $d_0 = 6$ cm, $r = 4$ cm and $I_0 = 10$ A. . .	49
III.6	Geometrical description of exemplary measurement conditions for an internal spatial harmonic decomposition and field reconstruction within a circle delineated by individual sensors. . . . .	50
III.7	Influence of increasingly large perturbing current on the decomposition coefficients of the first five orders. . . . .	53
III.8	Precision of current determination using different orders of the spatial harmonics decomposition and for different relative perturber-to-primary conductor distances $d_1/d_0$ . . . . .	57
III.9	Relative magnitude of an order $B_{n+1}$ with respect to the next lower order $B_n$ , in dependence of the sensor array radius $r$ and the array center-to-conductor distance $d_0$ . . . . .	58
III.10	Magnitude of fourth order contribution $B_4$ to the reconstruction of the magnetic field for various combinations of the array-to-conductor distance $d_0$ and the array radius $r$ . . . . .	59
III.11	Coefficient error for random errors of the given magnitude for the radial (left) and angular (right) position of the individual (10) sensors. . . . .	62
III.12	Definition of misalignment/Euler angles $(\alpha, \beta)$ with respect to the measurement axes	63
III.13	Coefficient errors for rotation offsets around $\vec{e}_r$ : $\alpha = 0$ to $\pm 2^\circ$ (left) and around $\vec{e}_x$ : $\beta = 0$ to $\pm 2^\circ$ (right). . . . .	64
III.14	Error induced by out-of-measurement plane rotations of the array around $\vec{e}_y$ (top left), $\vec{e}_z$ (top right) or a combination of both rotations (bottom). . . . .	66
III.15	Geometrical considerations for the calculation of a reference matrix. . . . .	69
III.16	Effect of decreasing step size/interpolation mesh for the determination of $d_0$ and $\varphi_0$ .	72

III.17	Contour plot of coefficient values for a range of values of $I_0$ and $I_1 (= I_{\text{ext}})$ (logarithmic scale); left: $a_{1,-1}$ right: $a_{6,6}$ ; sphere radius $r = 4$ cm, decomposition order $N = 6$ , for 360 triaxial measurement points on the sphere. . . . .	75
III.18	Exemplary conductor path for 3D model simulation study. . . . .	76
III.19	Various test configurations for practical implementations involving the placement of a given number of sensors (measurement points) on a sphere. . . . .	78
III.20	Error in coefficient values for the strongest contributions of each order $a_{n,-1}$ , for the decomposition of a two-conductor system with $I_0 = I_1$ . . . . .	83
III.21	Magnitude of decomposition orders by radius $r$ . . . . .	84
III.22	Relative magnitude of decomposition orders with respect to the next lower order . . . . .	85
III.23	Error in a fourth order coefficients for 'fabrication errors'. . . . .	87
III.24	Coefficient spectrum for different conductor paths. . . . .	89
IV.1	2D prototype. . . . .	99
IV.2	Design of the 3D prototype. . . . .	100
IV.3	3D prototype with 30 miniature fluxgate sensors. . . . .	101
IV.4	Laboratory setup . . . . .	102
IV.5	Influence of data acquisition parameters and the geomagnetic field on magnetic field measurements. . . . .	104
V.1	Transfer factor $k_n$ for array A at two different positions $d_0 = 6$ and 11 cm above the conductor $\varphi_0 = 180^\circ$ . . . . .	109
V.2	Coefficient error $\Delta a_n$ for increasing perturbation current. . . . .	111
V.3	Setup for misalignment determination. . . . .	117
V.4	AC measurement setup at Nexans in Donchery. . . . .	125
V.5	Comparison of DC and AC sweep calibration. . . . .	127
V.6	Current reconstruction precision for two-conductor AC system. . . . .	129
V.7	Precision of primary current determination for a three-conductor system. . . . .	131
V.8	Placement of the 3D prototype for DC measurements. . . . .	132
V.9	3D prototype results for DC measurements. . . . .	133
VI.1	Technological readiness scale based on the definition of the European Commission. <sup>[45]</sup> . . . . .	138

# List of Tables

I.1	Comparison of measurement requirements for the two application modes. . . . .	8
II.1	Comparison of magnetic field sensor technology. . . . .	24
II.2	Performance comparison for current sensor solutions. . . . .	27
II.3	Performance comparison of exemplary commercial products for the low-voltage grid and the different contactless measurement technologies. . . . .	28
III.1	Summary of sensor array positioning and alignment parameters with respective sources of error . . . . .	61
III.2	Error of calibration procedure for test series of 12 array position set values and for various degrees of perturbation. . . . .	70
III.3	Relative magnitude of higher order contributions to the reconstruction of the magnetic field, with respect to the magnitude of the first order. . . . .	77
III.4	Reconstruction quality using different sensor distributions. . . . .	81
IV.1	Commercial magnetic sensor technology for laboratory prototype. . . . .	97
V.1	Summary of the linear regression results for $a_n(I_0)$ . . . . .	110
V.2	Summary of the linear regression results for $a_n(I_1)$ . . . . .	113
V.3	Reproducibility test for two 'identical' 2D measurement arrays. . . . .	115
V.4	Comparison of magnetic field measurements from the sensors on array A with the reference values for a spatially homogeneous field. . . . .	119
V.5	Comparison of magnetic field measurements from the sensors on array B to the reference values for a spatially homogeneous field. . . . .	120
V.6	Result of calibration for measurements at different set values. . . . .	123
V.7	Transfer factors $k_{a_4}$ obtained during the first test series at the Nexans research facility	126



---

# Nomenclature

---

## General notations

$\mu_0, \mu_r$  Vacuum permeability, magnetic permeability

$\mathbf{A}(r, \vartheta)$  Magnetic vector potential

$\vec{B}$  Magnetic flux density

$\vec{H}$  Magnetic field

$\vec{M}$  Magnetization

$I_0$  Primary current magnitude

$I_{1,2,\dots}$  Perturbing current magnitude

## 2D spatial harmonics

$\mathbb{A}(r_i, \vartheta_i)$  Matrix containing the position-dependent terms of the decomposition problem

$a_n, b_n$  Decomposition coefficients of order  $n$

$d_0, \varphi_0$  Coordinates of source  $I_0$  with respect to the center of decomposition

$r, \vartheta$  Polar coordinates

$r_i, \vartheta_i$  Radial and angular position of a measurement point/sensor with respect to the center of decomposition

$\vec{x}$  Vector of coefficient values

$N$  Maximum decomposition order

## 3D spatial harmonics

$\mathbb{A}(r_i, \varphi_i, \vartheta_i)$  Matrix of sensor positions

$a_{n,m}$  Decomposition coefficients of order  $n$  and degree  $m$

$r, \varphi, \vartheta$  Spherical coordinates (radial, azimuthal, polar)